International Journal of Solids and Structures 160 (2019) 201–231

Contents lists available at ScienceDirect

International Journal of Solids and Structures

journal homepage: www.elsevier.com/locate/ijsolstr

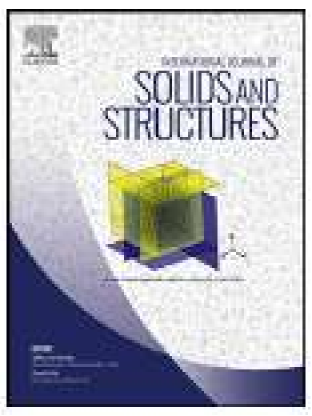

A bond-based micropolar peridynamic model with shear deformability: Elasticity, failure properties and initial yield domains

Vito Diana, Siro Casolo*

Department ABC, Politecnico di Milano, Italy

ARTICLE INFO

Article history:
Received 14 May 2018
Revised 26 October 2018
Available online 1 November 2018

Keywords:
Non-local lattice
Peridynamics
Lattice anisotropy
Micropolar model
Failure criteria

ABSTRACT

A generalized micropolar bond-based Peridynamic model with shear deformability for linear and non-linear problems is proposed. The analytical implicit formulation is derived from the definition of a specific microelastic energy function for micropolar nonlocal lattices, giving particular attention to numerical implementation aspects of the model. We investigate the effectiveness of this formulation, empathizing the importance of considering particle's rotations in enriched bond-based peridynamic models with arbitrary Poisson's ratios. Numerical analyses show that a microelastic energy function dependent on a shear deformation measure in which rotational degrees of freedom of the particles are not included, leads to a model not capable to describe properly the elastic behavior of isotropic solids subjected to non-homogeneous deformation fields. Moreover two novel deformation-based failure criteria for micropolar peridynamics accounting for bond shear deformation, associated or not with the corresponding stretch of the ligament, are proposed. A deep investigation is carryied out on the direction dependency of the failure response of the lattice, considering different horizon/grid spacing ratios. In this way the maximum errors are estimated and the effective initial yield domains corresponding to the failure criteria presented are identified in two dimensional principal $s_1 - s_2$ and generalized $s - \gamma$ deformations space.

1. Introduction

In the last two decades, the interest towards the computational models based on a full discrete approach is growing, especially when analyzing crack path and geometry in boundary value problems where strong discontinuities arise. Among these, lattice models in which the solid is imagined as an assembly of discrete units connected by springs or in general rehological elements, reflecting in a certain sense the atomistic structure of matter, have proved as promising approaches (Nikolić et al., 2017; Bolander and Saito, 1998; Griffiths and Mustoe, 2001; Gerstle et al., 2007; Cusatis et al., 2011; Brighenti et al., 2013; Kale and Ostoja-Starzewski, 2015; Yao et al., 2016; Ostoja-Starzewski, 2002; Mohammadipour and Willam, 2017; Casolo, 2009). The fundamental concept of using the lattice formulations in solid mechanics was first introduced by Hrennikoff (1941). He replaced a continuum elastic domain by a lattice of truss, the elastic properties of which were determined based on those of the continuum domain with no cracking, following the original idea proposed by Navier (1827) in the early days of elasticity. A well-known issue of the lattice spring model with only pairwise axial interaction among particles, is the restriction on effective value of Poisson's ratio, which in the general three dimensional case is fixed to the value of $\nu = 1/4$ (Stakgold, 1950; Ostoja-Starzewski, 2002). The Poisson's ratio restriction was overcome by introducing particles rotational DOFs (Hrennikoff, 1941; Schlangen and Garboczi, 1997; Ostoja-Starzewski, 2002), following an intuition by Voigt (1887), and by considering non-central force interactions (shear springs) between particles (Pan et al., 2018; Cusatis et al., 2017; Born and Huang, 1954). Hassold and Srolovitz (1989) proposed an approach based on the definition of an harmonic potential for the rotation of bonds from their initial orientation, whereas Keating (1966) introduced a strain energy terms which depends on the change in the angle between two neighboring normal springs to modify Poisson's ratio values without violating the rotational invariance requirement (Nikolić et al., 2017). Alternative strategies to handle this issue involved the use of non-local axial interaction terms into the lattice system potential (Chen et al., 2014), or the multi-body shear spring approach in which the relative shear deformation is calculated from a particle cluster by using a local strain method rather than the shear displacement of two particles (Jiang et al., 2017; Zhao et al., 2011).

Another important feature of lattice models is that, differently from classical continuum based formulations in which the strain measures comes from the definition of a strain tensor, the deformation is usually measured in a finite number of direc-

---

* Corresponding author.
E-mail address: siro.casolo@polimi.it (S. Casolo).

https://doi.org/10.1016/j.ijsolstr.2018.10.026
0020-7683/

tions due to the fixed orientation of the ligaments (Monette and Anderson, 1994). Thus the lattice topology leads to an intrinsic anisotropy of the failure response, which can influence the biased crack propagations and strongly depends on the specific discretization adopted, as pointed out by Tancogne-Dejean and Mohr (2018). They analyzed elasticity and initial yield surfaces of several truss lattices materials theoretically, numerically and experimentally, founding that elastic isotropic truss lattices are still plastically anisotropic. Irregular lattices or random geometry lattices can greatly reduce this effect (Schlangen and van Mier, 1992; Cusatis et al., 2003), but they are not generally elastically uniform under uniform straining (Nikolić et al., 2017). An alternative strategy to solve this issue is represented by non-local lattices (Pan et al., 2018; Chen and Liu, 2016) or by models arising from Peridynamic (PD) theory of solid mechanics (Silling and Lehoucq, 2010). In fact, extending the range of non-local actions, one can drastically reduce or in some cases eliminate the anisotropic effect in regular lattice grids (Bobaru, 2011; Dipasquale et al., 2016).

Inspired by the original molecular theory of elasticity by Navier (1827), Cauchy (1850) and Poisson at the begining of XIX century (Poisson, 1813; Capecchi et al., 2010), the Peridynamic theory proposed by Silling (2000), replaces the differential equations of classical continuum mechanics with integro-differential equations and thus is valid anywhere in a deformable body regardless of any discontinuity (Yaghoobi and Chorzepa, 2017). Solid materials are considered as a collection of particles held together by internal forces that are functions of material and kinematic variables defined among interacting particles within a material horizon of radius δ. The size of the horizon depends on the nature of the problem, in the case of problems that are expected to have nonlocal physical behavior (Madenci and Oterkus, 2014), an appropriate nonzero value of the horizon δ is required, however in numerical simulation of macroscale problems it can be chosen according to convenience, since, the bond's elastic parameters can be fitted to experimental data for any value of δ. The PD model as originally proposed (bond-based PD, i.e. BBPD) is a central force model, and therefore (as for the Navier and Poisson's elasticity theory), the Poisson's ratio is a fixed value $\nu = 1/4$ for 3D and plane strain problems and $\nu = 1/3$ for plane stress problems. To overcome this shortcoming, various efforts have been made. Silling et al. (2007) introduced a more general formulation, coined state-based PD (SBPD) in which the pairwise forces between two particles are, in general, functions of the deformations of all nodes within the neighborhoods of the particles and the non-ordinary state-based model (NOSB), a tool for adapting classical material models for use with peridynamics and for simulating the material with advanced constitutive models (Warren et al., 2009; Foster and Xu, 2018). The state-based PD formulation eliminates the Poisson's ratio restriction, and Sarego et al. (2016) showed that ν can vary in the range from 0.1 to 0.45 for 2D problems, but it comes with a computational penalty, normally increasing the cost by at least a factor of two compared with the bond-based formulations (Cheng et al., 2015). The drawback of NOSB peridynamics are instead the relatively complicated implementation, the open question regarding the zero-energy modes and the high computational cost. The capability of NOSB peridynamics is attributed to the arbitrary direction of bond force, which is in contrast to the BB peridynamics or SB peridynamics only allowing extensional bond force. In fact, the component of bond force out of the bond direction in NOSB peridynamics represents the shear force due to shear deformation. It can be seen that one problem in BB peridynamics or SBPD peridynamics is that the axial bond force cannot account for the shear deformation but only for the extensional deformation (Rabczuk and Ren, 2017; Ren et al., 2016).

In the context of bond-based models, Liu and Hong (2012) proposed a force compensation scheme adding additional forces on each pairwise force between particles to simulate materials with a non fixed Poisson's ratio. Wang et al. (2018) starting from the Stillinger-Weber potential functions (Stillinger and Weber, 1985; Zhang and Chen, 2014), derived a conjugated bond-pair-based peridynamic formulations in which the interacting forces between two material points within one horizon are not only related to the stretch of the bond, but also related to the rotation of the conjugated bond angles. Prakash and Seidel (2015) developed an enriched two-parameter linear elastic bond-based peridynamic model for plane stress conditions, where two springs were introduced to describe the displacements in the normal and tangential directions and to handle with variable Poisson's ratios. However they showed that in the case of $\nu = 1/3$, the bond axial stiffness obtained by the authors cannot reduce to the well known result reported by Silling and Askari (2005). A BBPD formulation which account for single bond shear deformation has been proposed recently (Zhu and Ni, 2017). The classical peridynamic formulation is extended by incorporating the bond rotation effect so that the pairwise force between two particles can be decomposed in a normal and tangential component to improve the prediction of the effective Poisson's ratio (These bonds with normal force and shear force are isomorphic to a spring network with central force plus rotational springs). The authors applied the model (namely PDS model) only to simulate the mechanical behavior of elastic isotropic solids with variable Poisson's ratio and subjected to homogeneous deformation field, but no considerations have been made about the performance of the model under more complex deformation fields and on the fundamental requirement of rotational invariance, which seems not preserved. Actually, Gerstle et al. (2007) enhanced BBPD by allowing the bond of two material points to also develop pairwise peridynamic moments. The resulting model, called micropolar peridynamic model, can simulate linear elastic materials with arbitrary Poisson's ratios. It is noted that in the Gerstle's micropolar peridynamic model, each bond was viewed as a micro cantilever Euler-Bernoulli beam with two stiffness moduli, one related to stretch deformation and the other to bending effect (i.e. the ligament curvature), whereas the failure is controlled by the definition of a maximum tensile and compressive bond stretch limit. Later, Chowdhury et al. (2015) proposed a state-based version of micropolar peridynamics in linear elasticity, without any considerations about the failure response and the post-elastc behavior. PD theory has been used so far to model a wide variety of problems involving fracture (Bobaru et al., 2012; Madenci and Oterkus, 2014; Gerstle et al., 2007; Silling, 2014; Casolo and Diana, 2018; Lee and Hong, 2016), plasticity (Luo et al., 2018; Sun and Sundararaghavan, 2014) and viscoelasticy (Madenci and Oterkus, 2016; Mitchell, 2011; Weckner and Mohamed, 2013), however further research is required in the context of failure criteria (Dipasquale et al., 2017). Moreover the systematic study of the effects of multiple neighbor non-local interaction on the failure response of PD lattice is rarely found.

In this paper, a generalized bond-based micropolar peridynamic formulation (MPPD) accounting for shear deformability is presented. Differently from the traditional BBPD approach, and Gerstle's micropolar model in which shear deformation measure and failure condition based on shearing deformations are not defined, the conceived model is based on the definition of a microelastic energy function which depends on three deformation parameters: the bond stretch, the bond shear deformation accounting for the rotational degrees of freedom, and the particles relative rotation. Hence three different stiffness parameters for each peridynamic ligament can be defined and calibrated separately, leading to a more general micropolar model applicable to a wide variety of mechanical problems. Both the micropolar Gerstle's formulation and the PDS model can be considered as special cases of the conceived MPPD model. In particular, the latter is obtained keeping

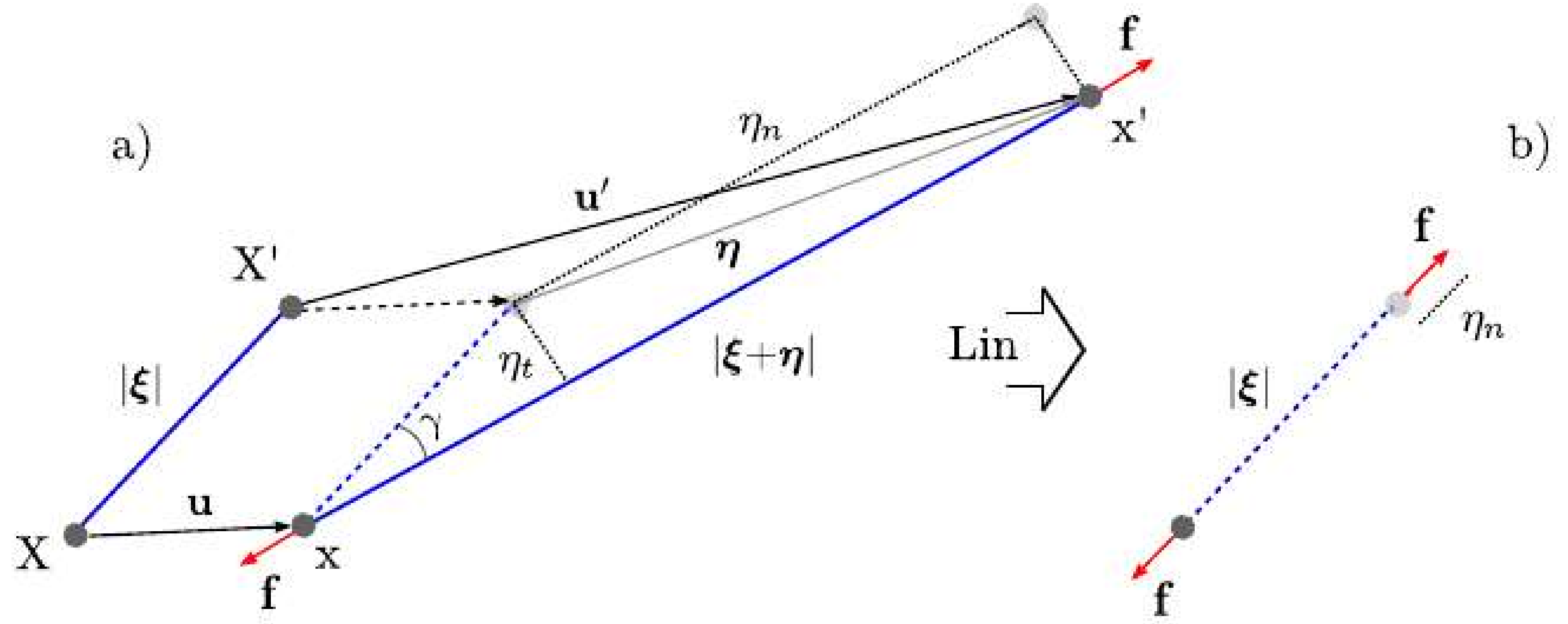

Fig. 1. (a) Undeformed and deformed configuration of a BBPD bond; (b) Linearized BBPD (the pairwise force is directed along the line connecting the two particles in the undeformed configuration).

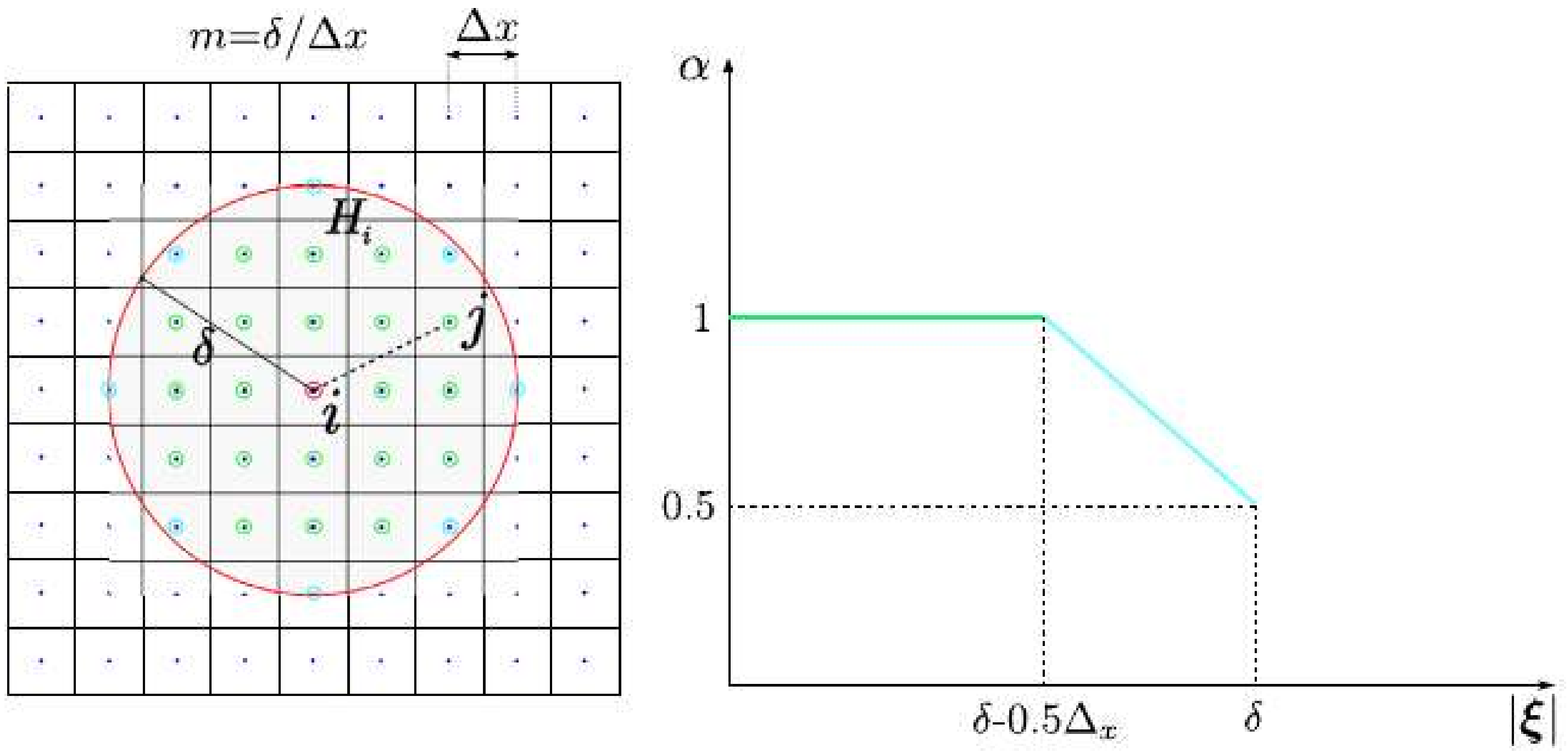

Fig. 2. (sx) Proximity search procedure for neighboring list identification (in green the full neighboring particles with $\alpha = 1$ and in cyan the partial neighboring particles);(dx) Volume correction coefficient α within the horizon. The ratio decreases to 1/2 at the border of a horizon. (For interpretation of the references to colour in this figure legend, the reader is referred to the web version of this article.)

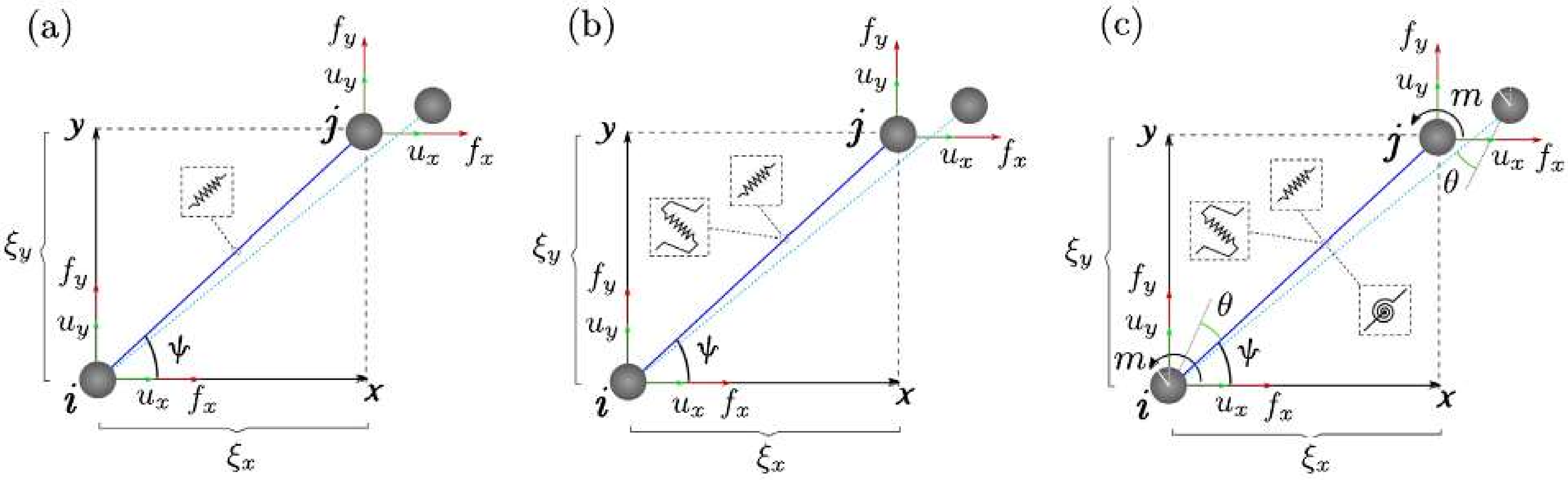

Fig. 3. Schematics of bond configuration connecting two particles i and j for (a):bond-based PD (one term in the microelastic function dependent on bond stretch); (b): enriched bond-based model PDS (two terms in the microelastic function dependent on bond stretch and bond sliding, respectively); (c): bond-based micropolar MPPD model (three terms in the microelastic function dependent on bond stretch, shear deformation and relative rotation, respectively).

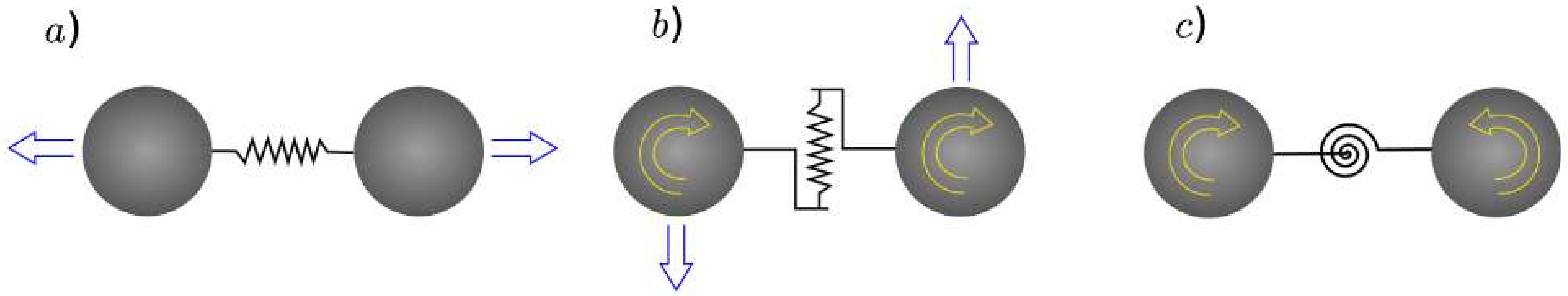

Fig. 4. Sketch of the interactions between two particles: (a) due to normal spring, (b) due to shearing spring, (c) due to rotational spring.

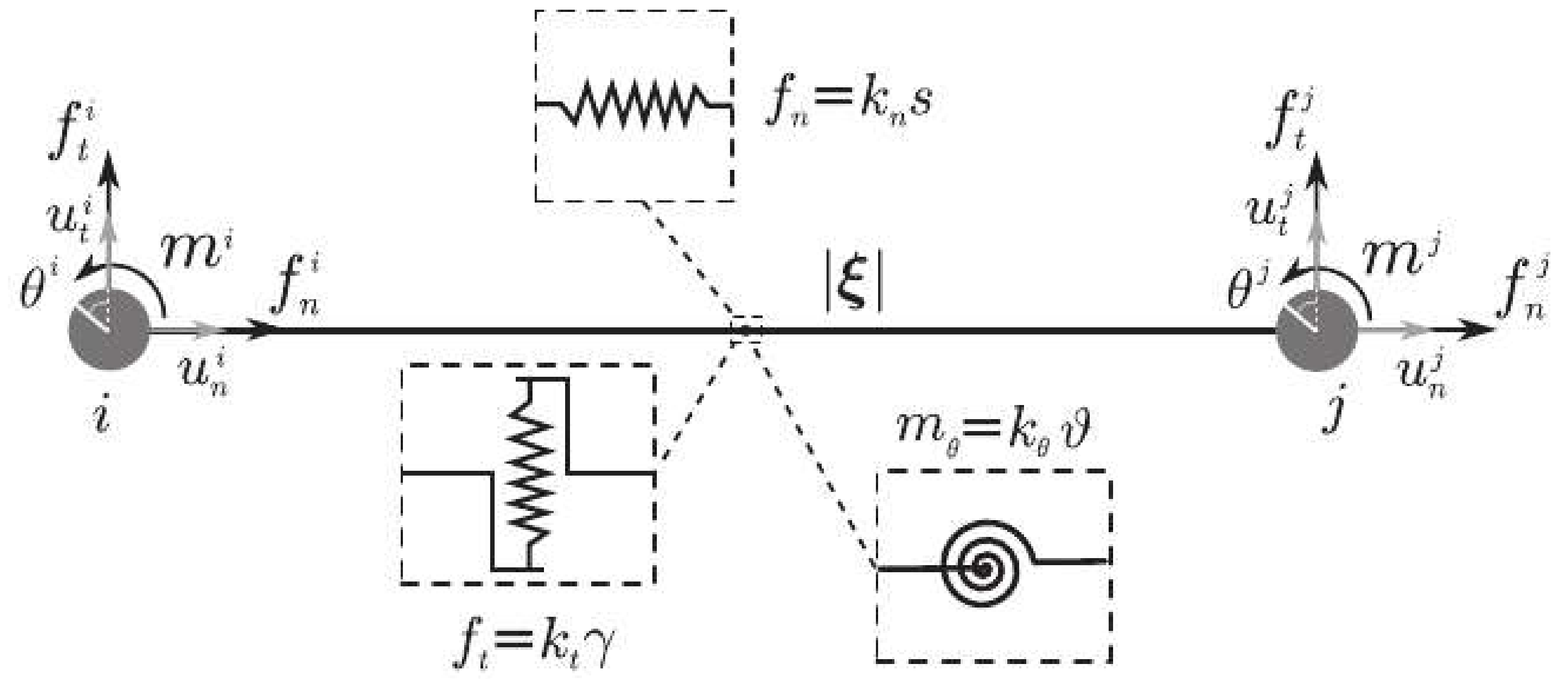

Fig. 5. Schematics of bond configuration connecting two particles i and j in the local coordinate system for bond-based micropolar peridynamics. The bond can be idealized as a set of three (axial, shear and rotational) equivalent springs placed in midpoint of the ligament.

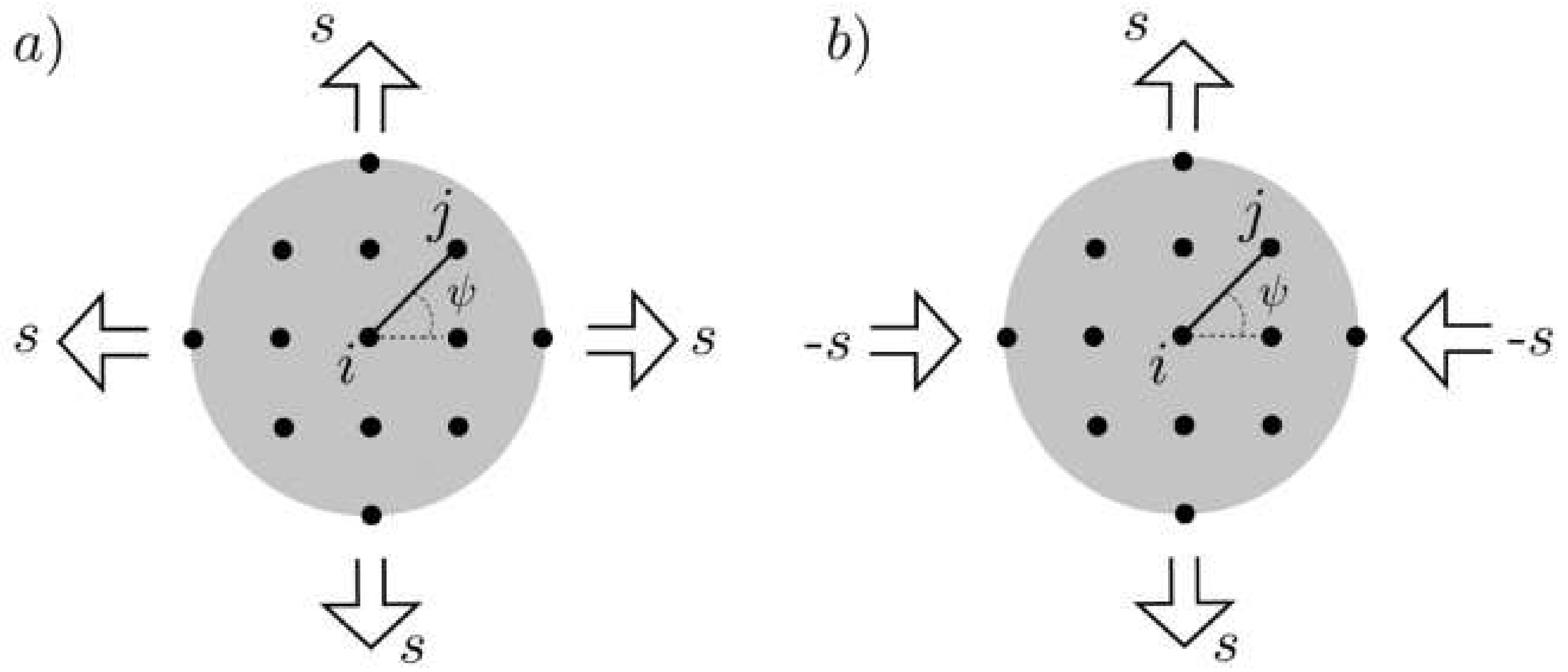

Fig. 6. Schematics of family H_x subjected to: (a) isotropic expansion field of orthogonal PD stretch components $s_1 = s_2 = s$; (b) pure shear field of orthogonal PD stretch components $s_1 = -s_2 = s$.

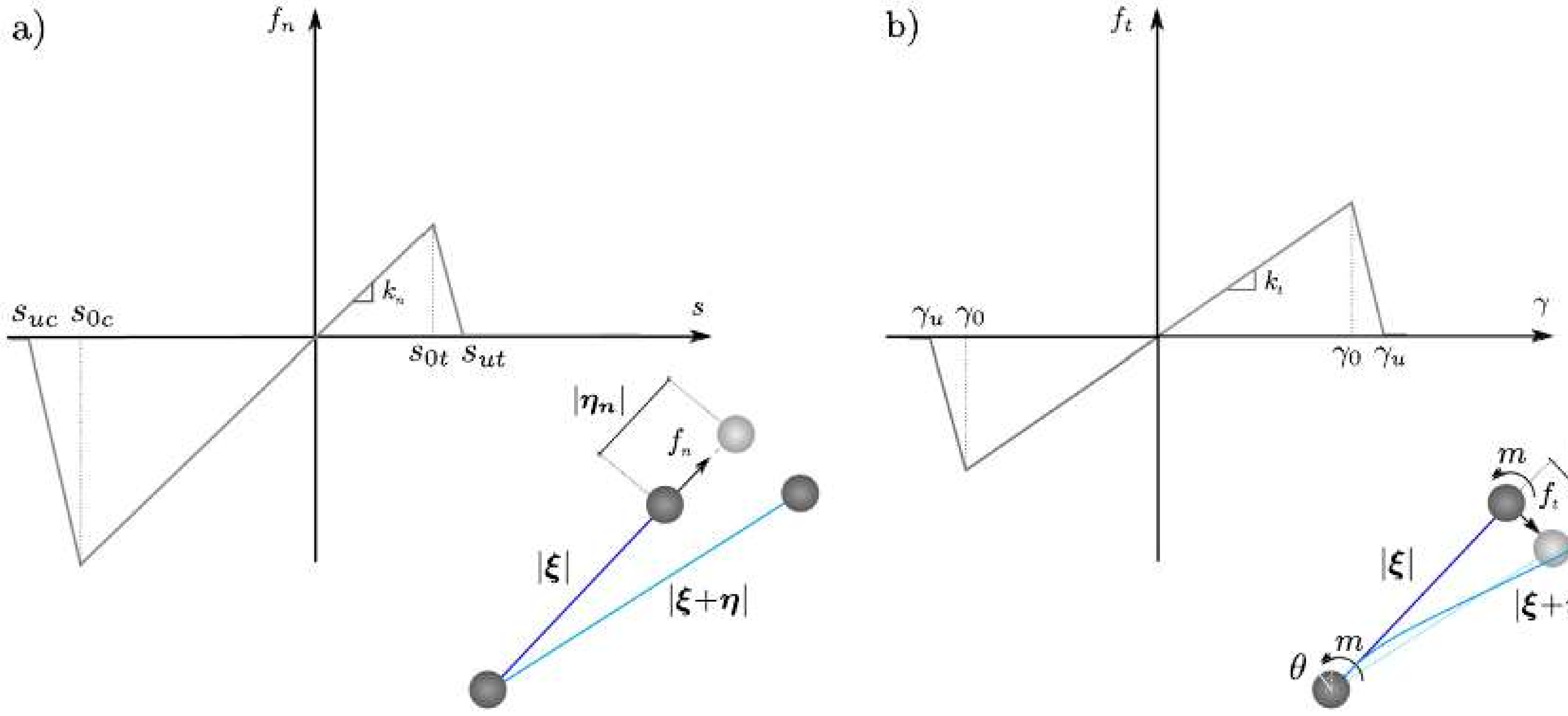

Fig. 7. Bond force-bond deformation relationship in peridynamics; (a) axial bond force-bond stretch relationship; (b) Shear bond force-bond sliding relationship (In figure is represented the schematics of bond shearing deformation in MPPD with EB beam-like ligaments.).

the rotational degree of freedom restrained in the MPPD model. Moreover we propose two novel failure criteria based on the definition of a bond shearing deformation limit that can be function or not of the corresponding axial deformation of the ligament.

This paper is structured as follows. In Section 2, an analytical implicit formulations of BBPD and PDS for linearized problems is given, handing particular attention to numerical implementation aspects of the models. The novel generalized three parameter micropolar model is then derived starting from the definition of specific shear and particles relative rotation deformation measures. In this way the microelastic energy function is written and the generalized bond stiffness operator for MPPD is obtained. The two parameter Gerstle's micropolar model is then obtained as special case, simply considering the relative rotation stiffness coefficient, function of the bond shear stiffness, as in a beam-like element. In the last part of the section, two novel deformation-based failure criteria are presented and the theoretical first yield domains in two dimensional principal and generalized deformations space are identified through analytical procedures. In Section 3, we investigate the effectiveness of the MPPD formulation in elasticity and its capabilities in simulating the mechanical behavior of Isotropic solids with arbitrary Poisson's ratio, under homogeneous and non-homogeneous deformation fields, comparing the results with those obtained utilizing FEM analyses and PDS model. To this end a nat-

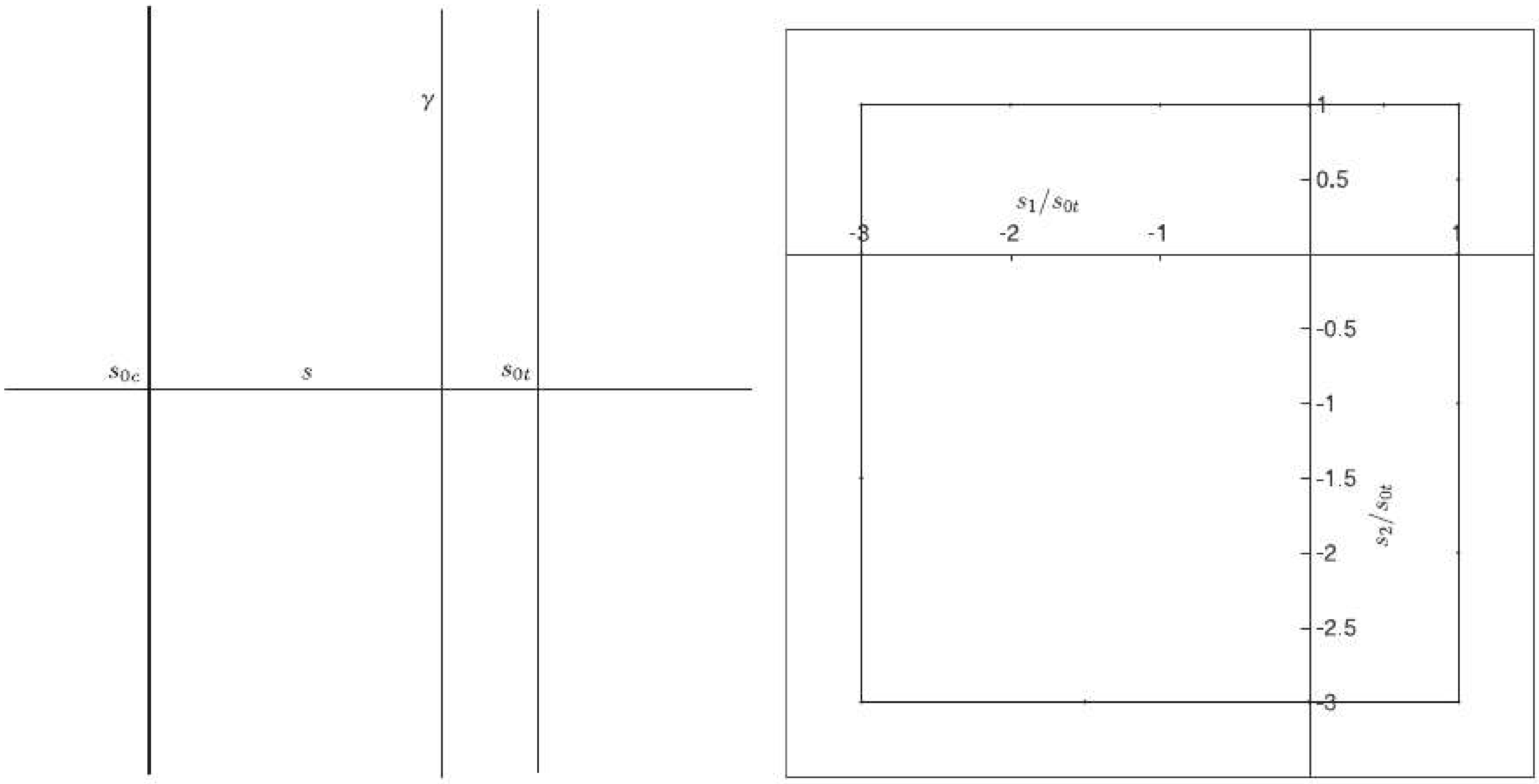

Fig. 8. Yield loci in generalized deformations $s-\gamma$ plane (sx) and in two dimensional principal PD stretch space s_1-s_2 (dx) according to a max bond stretch criterion with $s_{0c}=-3s_{0t}$.

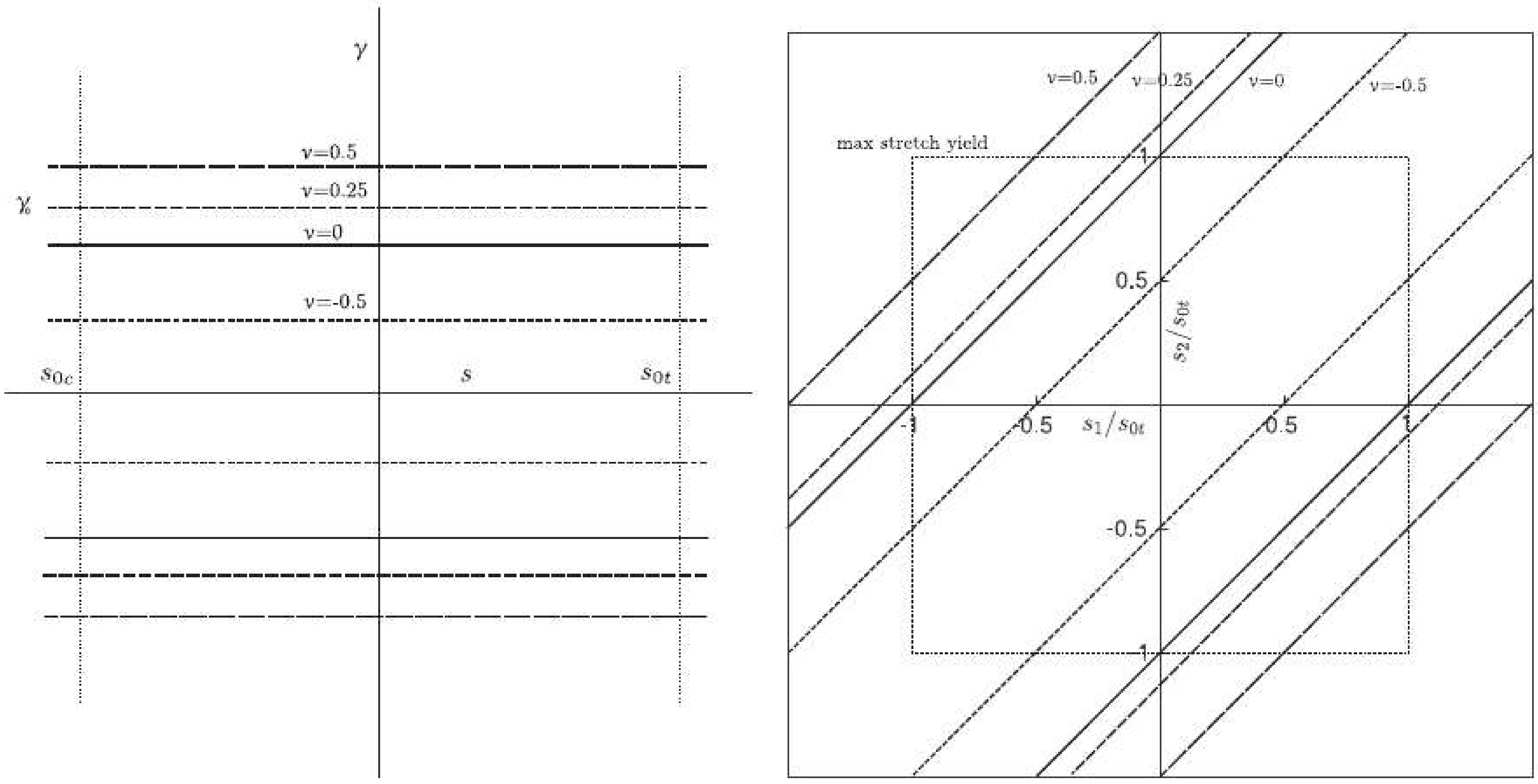

Fig. 9. Yield loci in generalized deformations $s-\gamma$ plane and in two dimensional PD stretch space s_1-s_2 according to a max sliding criterion ($s_{0c}=-s_{0t}$).

ural frequency study and static analyses considering simple loading cases are carried out. In Section 4, a deep investigation on first yield conditions corresponding to the maximum stretch criterion and to the failure criteria presented in Section 2 is showed. The intrinsic anisotropic failure response of the lattice model is quantified, considering different horizon/grid spacing ratios. In this way the relative maximum errors are estimated and the effect of the aforementioned grid-induced anisotropy on the modification of the theoretical first yield domains is showed, considering different range of non-local actions. Finally, we conclude the findings in this study and discuss the issues to be addressed for future development. A MATLAB (Matlab, 2017) computing on an UNIX OS is used to generate the results presented in this study.

2. Linearized bond-based peridynamics

Peridynamics is a nonlocal theory of mechanics in which material points in a continuum or in a group of discrete particles interact with each other through forces that are functions of material and kinematic variables (Silling, 2017). The acceleration of any particle at $\mathbf{X}$ in the reference configuration at time t is found from

$$\rho\ddot{\mathbf{u}}(\mathbf{X},t)-\int_{H_x}\boldsymbol{f}(\mathbf{u}'-\mathbf{u},\mathbf{X}'-\mathbf{X})dV_{\mathbf{X}'}-\mathbf{b}(\mathbf{X},t)=\mathbf{0}\quad for\quad \mathbf{X}\in\Omega, \tag{1}$$

where Ω is the domain occupied by the body, whereas $\mathbf{X}'-\mathbf{X}=\boldsymbol{\xi}$ and $\mathbf{u}'-\mathbf{u}=\boldsymbol{\eta}$ are the relative position (i.e. reference bond) and the relative displacement between the material points $\mathbf{X}$ and $\mathbf{X}'$ (see Fig. 1). The body force vector is $\mathbf{b}$, and $\mathbf{f}$ is the pairwise force in the peridynamic bond[1] The integral is defined over a region H_x called the horizon region of radius δ. The discretized form of the

---

[1] In general, the pairwise force $\mathbf{f}(\boldsymbol{\xi},\boldsymbol{\eta})$ is collinear with the deformed locations of the two particles, however in linear BBPD theory the pairwise force is directed along the direction of the undeformed ligament.

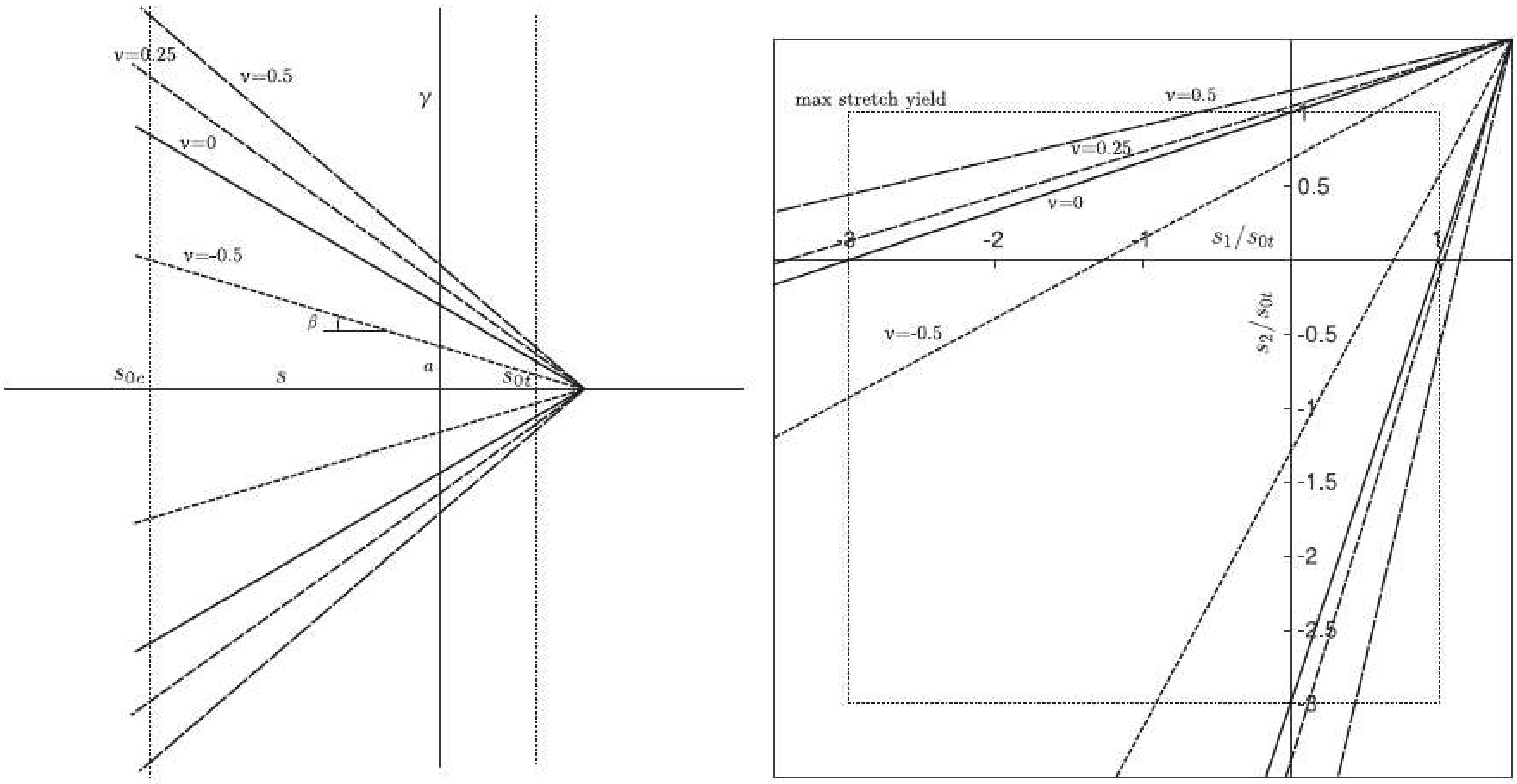

Fig. 10. Yield loci in generalized deformations $s - \gamma$ plane (sx) and in two dimensional PD stretch space $s_1 - s_2$ (dx) according to a frictional sliding criterion with $s_{0c} = -3s_{0t}$.

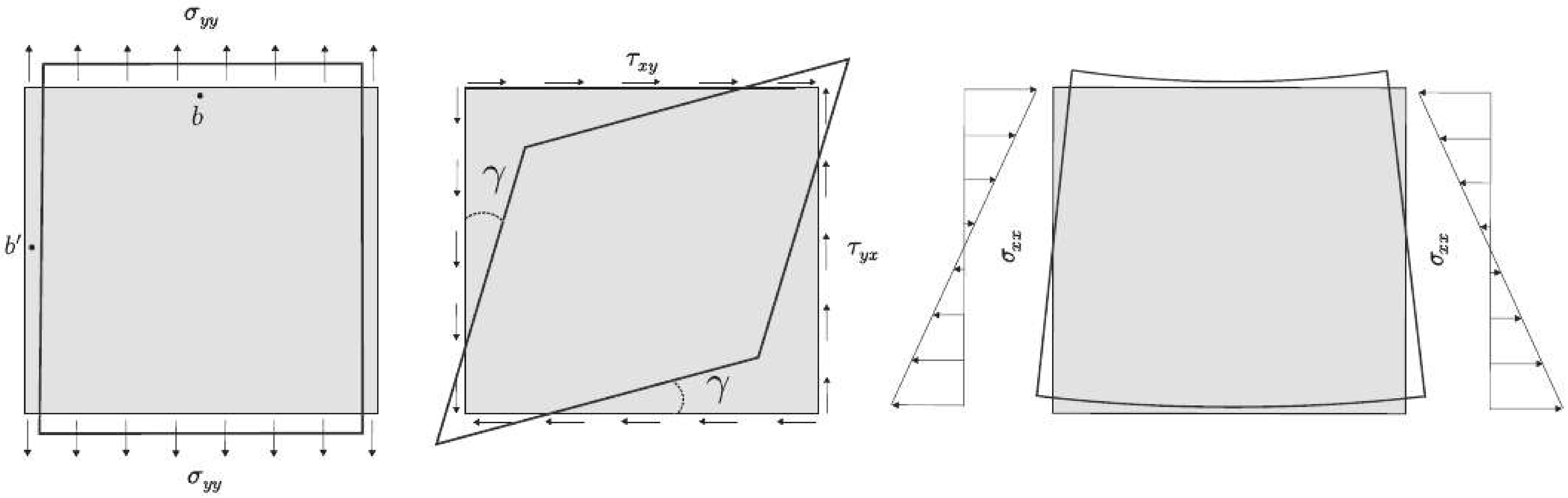

Fig. 11. Schematics of boundary conditions of the square lamina subjected to simple traction, pure shear and simple bending. Regarding the case of simple traction, in order to minimize the error in the numerical estimation of the Poisson's ratio, we evaluate the displacements in two points b and b' positioned at a distance δ from the boundaries.

linear momentuum equilibrium equation at time t is:

$$\sum_{j=1} \mathbf{f}(\mathbf{u}_j - \mathbf{u}_i, \mathbf{X}_j - \mathbf{X}_i)\Delta V_j + \mathbf{b}_i = \rho\ddot{\mathbf{u}}_\mathbf{i} \tag{2}$$

where subscript j denotes a particle within the horizon of particle i. Thus the sum in Eq. (2) is taken over all nodes j such that $|\mathbf{X}_j - \mathbf{X}_i| \leq \delta$ (i.e. neighboring particles of particle i). In the case of a microelastic peridynamic material, a linearized form of the previous equation, in the hypothesis of static conditions (Zaccariotto et al., 2015) is

$$\sum\nolimits_{j=1}\Big[\mathbf{C}(\boldsymbol{\xi})\boldsymbol{\eta}\Big]_{ij}\Delta V_j + \mathbf{b}_i = \sum\nolimits_{j=1}\Big[c(\boldsymbol{\xi})\frac{\boldsymbol{\xi}\otimes\boldsymbol{\xi}}{|\boldsymbol{\xi}|^3}\boldsymbol{\eta}\Big]_{ij}\Delta V_j + \mathbf{b}_i = \mathbf{0} \tag{3}$$

where $\mathbf{C}(\boldsymbol{\xi})$ is the second-order micromodulus tensor and $c(\boldsymbol{\xi})$ is the micromodulus function or normal stiffness $k_n(\boldsymbol{\xi})$ of the ligament. The expression of the micromodulus function[2] is obtained by equating, for a homogeneous deformation, the microelastic energy density of peridynamic solid with the strain energy density of classical linear elastic homogeneous body (Gerstle et al., 2009)

$$\Phi(\mathbf{X}) = \frac{1}{2}\int_{H_x}\frac{c(|\boldsymbol{\xi}|)s^2|\boldsymbol{\xi}|}{2}dV_{\mathbf{X}'} \tag{4}$$

where s is the bond stretch

$$s = \frac{|\boldsymbol{\xi}+\boldsymbol{\eta}| - |\boldsymbol{\xi}|}{|\boldsymbol{\xi}|} \tag{5}$$

which in a linearized theory is written as

$$s = \frac{1}{|\boldsymbol{\xi}|}\left(\boldsymbol{\eta}\cdot\frac{\boldsymbol{\xi}}{|\boldsymbol{\xi}|}\right) = \frac{\eta_n}{|\boldsymbol{\xi}|} \tag{6}$$

where η_n is the component of $\boldsymbol{\eta}$ directed along the undeformed bond of unit vector $\boldsymbol{\xi}/|\boldsymbol{\xi}|$. For plane-stress and plane strain conditions, in the case of constant (cylindrical) micromodulus function we obtain

$$c(|\boldsymbol{\xi}|) = c = \begin{cases} \dfrac{6E}{\pi t\delta^3(1-\nu)} & \text{plane stress} \\ \dfrac{6E}{\pi t\delta^3(1-2\nu)(1+\nu)} & \text{plane strain} \end{cases} \tag{7}$$

where t is the thickness, δ is the horizon. E and ν are the Young's modulus and the Poisson's ratio, respectively. The computer code

---

[2] We are considering isotropic materials, thus $c(\boldsymbol{\xi}) = c(|\boldsymbol{\xi}|)$.

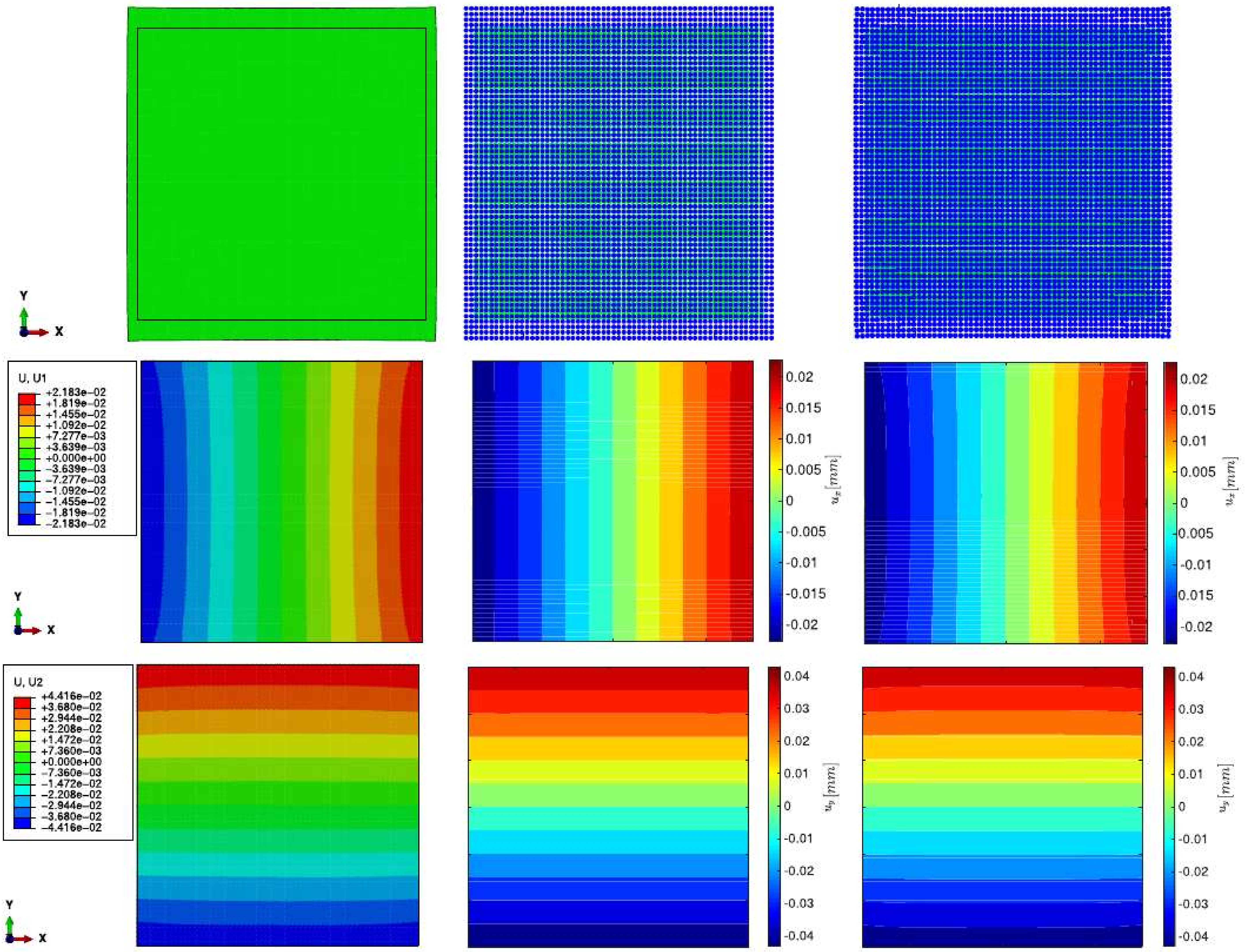

Fig. 12. Simple traction, $\nu = -0.5$: Deformed shape and displacements map obtained with FEM, PDS, MPPD.

performs the discretization of the PD body using mesh generation tools developed for finite-element analyses. Thus the structure is discretized into a set of subvolumes, each of which has a single PD material point located at its centroid. Subsequently an algorithm determines the neighboring particles (i.e. the connections) of each particle of the discretization. In this work, a linear elastic relationship between the magnitude of the pairwise force and the bond relative elongation is adopted

$$f = f_n = cs \tag{8}$$

We implemented a quadrature scheme in which partial neighbor intersections are also considered. This aspect adds complexity to the creation of neighbor lists (Fig. 2) but it increases the precision of the quadrature. The results of the partial neighbor intersection computation (i.e. the value of the volume correction coefficient α) is calculated with (Liu and Hong, 2012)

$$\alpha(|\boldsymbol{\xi}|) = \begin{cases} \frac{\xi-\delta+0.5\Delta x}{\Delta x} & \text{if} \quad (\delta - 0.5\Delta x) < |\boldsymbol{\xi}| \leq \delta \\ 1 & \text{if} \quad |\boldsymbol{\xi}| \leq (\delta - 0.5\Delta x) \\ 0 & \quad otherwise \end{cases} \tag{9}$$

where Δx is the grid spacing. The elastic problem is solved using an implicit scheme where the stiffness matrix is defined at bond level as

$$[K]_{bond} = \frac{c}{|\boldsymbol{\xi}|^3}\alpha\,\Delta V_i \Delta V_j \begin{bmatrix} \xi_x^2 & \xi_x\xi_y & -\xi_x{}^2 & -\xi_x\xi_y \\ \xi_x\xi_2 & \xi_y{}^2 & -\xi_x\xi_y & -\xi_y{}^2 \\ -\xi_x{}^2 & -\xi_x\xi_y & \xi_x{}^2 & \xi_x\xi_y \\ -\xi_x\xi_y & -\xi_y{}^2 & \xi_x\xi_y & \xi_y{}^2 \end{bmatrix} \tag{10}$$

where ξ_x and ξ_y are the components of the bond vector between the particles i and j. This expression of $[K]_{bond}$ can be obtained considering the definition of the macroelastic potential energy for a peridynamic body

$$\hat{\Phi}(\mathbf{X}) = \frac{1}{2}\int_{\Omega}\int_{H_x} \frac{c(|\boldsymbol{\xi}|)s^2|\boldsymbol{\xi}|}{2} dV_{\mathbf{X}'} dV_{\mathbf{X}} \tag{11}$$

In the case of a single bond of length $|\boldsymbol{\xi}|$ between two particles i and j (see Fig. 3), we can write in a discrete form the balance of the variation of the total macroelastic energy and the work W done by the external nodal forces $\{p\}$ (in the hypothesis of small deformations, i.e. linearized PD) as

$$\hat{\Phi} = \frac{1}{2}\{u\}^T \frac{1}{2}\{b\}c(|\boldsymbol{\xi}|)\Delta V_i|\boldsymbol{\xi}|\alpha\,\Delta V_j\{b\}^T\{u\} = \frac{1}{2}\{u\}^T\{p\} = W \tag{12}$$

where c is the micromodulus of the bond, $\{u\}$ is the vector of the particles displacements,

$$\{u\} = \{u_x^i \quad u_y^i \quad u_x^j \quad u_y^j\}^T \tag{13}$$

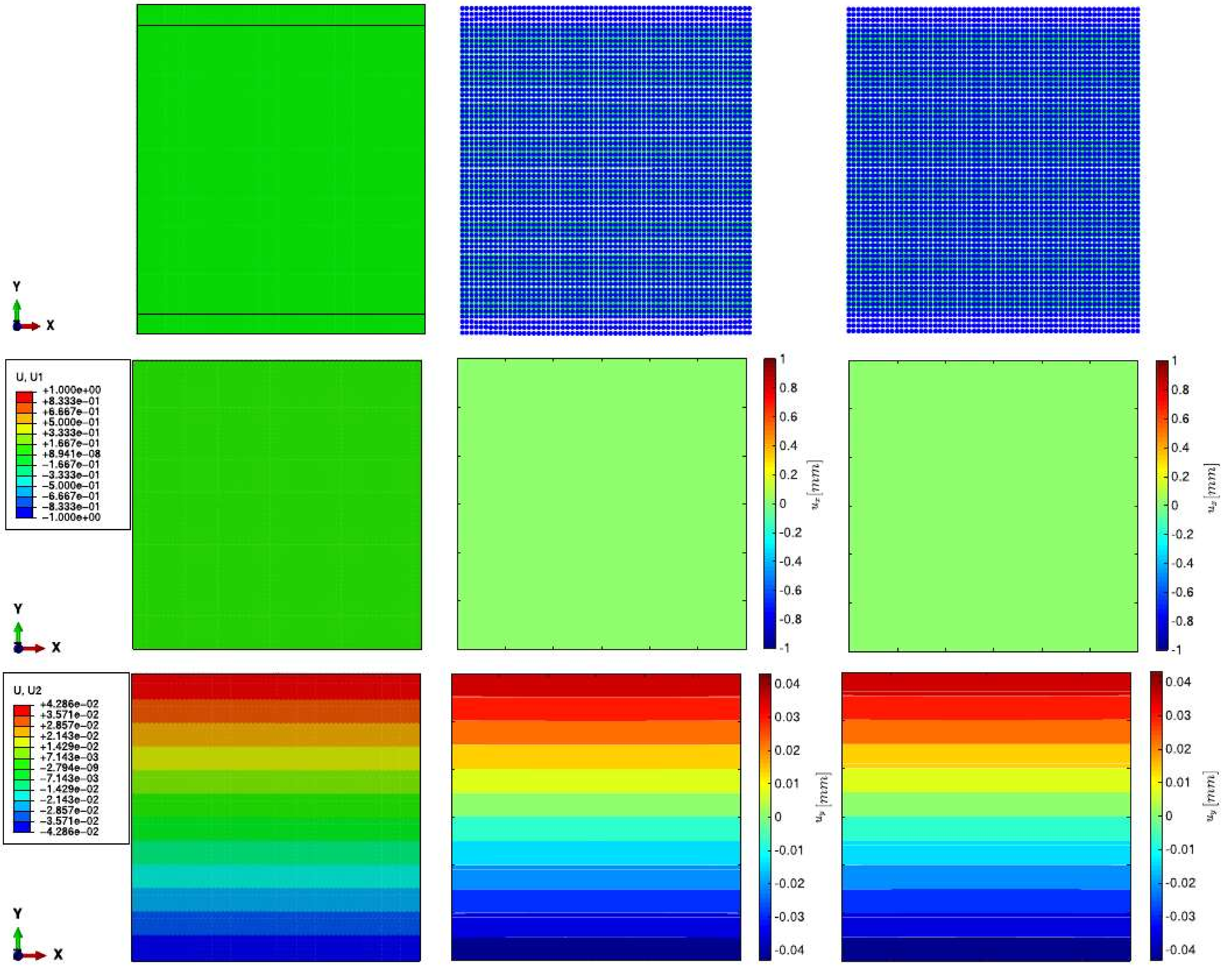

Fig. 13. Simple traction, $\nu = 0$: Deformed shape and displacements maps obtained with FEM, PDS, MPPD.

ΔV_i and $\alpha \Delta V_j$ are the volumes of the bond particles (ΔV_j is reduced according to Eq. (9)), while b^T defined as

$$\{b\}^T = \frac{1}{|\boldsymbol{\xi}|}\{-\cos\psi \quad -\sin\psi \quad \cos\psi \quad \sin\psi\} \tag{14}$$

relates the bond particles displacements with the bond stretch in such a way that $s = \{b\}^T\{u\}$. The factor 1/2 in Eq. (11) is included because the energy stored in each bond is associated equally with the two particles i and j, thus in the case of a uniform grid it is removed from Eq. (12) in order to avoid double-counting of the bonds $i-j$ and $j-i$. In this way, following Eq. (12), $[K]_{bond}$ is given by

$$[K]_{bond} = \{b\}c(|\boldsymbol{\xi}|)\Delta V_i|\boldsymbol{\xi}|\alpha\Delta V_j\{b\}^T \tag{15}$$

Following the assembly of the global structure stiffness matrix, the displacements and forces can be determined in the usual manner. It is worth noting that in Bond-based PD the Poisson's ratio of the material assumes the value 1/3 for (2D) plane stress and 1/4 for (2D) plane strain and 3D analyses, as a result of the pairwise central force nature of the interaction between particles. In this work the volume method for correcting the peridynamic surface effect is adopted (Bobaru et al., 2015; Le and Bobaru, 2017), thus the dimensionless correction factor for the micromodulus c of the bond connecting two particles i and j is computed with

$$\lambda = \frac{2V_0}{V(H_i) + V(H_j)} \tag{16}$$

where $V_0 = t\pi\delta^2$, whereas $V(H_i)$ and $V(H_j)$ are the real volumes associated with H_i and H_j, respectively.

2.1. BBPD with shear bonds for arbitrary Poisson's ratio (PDS model)

A bond-based formulation which account for single bond shear deformation have been proposed recently (Zhu and Ni, 2017). The classical peridynamic constitutive equation is extended by incorporating the bond rotation effect so that the pairwise force between two particles can be decomposed in a normal and tangential component[3] to improve the prediction of the effective Poisson's ratio (This model is now called in this paper BBPDS or simply PDS model). Adopting a linearized form, the micro elastic energy density $\Phi(\mathbf{X})$ is rewritten by introducing the contribution of tangential strain

$$\Phi(\mathbf{X}) = \frac{1}{2}\int_{H_x} \frac{c(|\boldsymbol{\xi}|)s^2|\boldsymbol{\xi}|}{2} + \frac{g(|\boldsymbol{\xi}|)\gamma^2|\boldsymbol{\xi}|}{2} dV_{\mathbf{X}'} \tag{17}$$

---

[3] These bonds with normal force and shear force are isomorphic to a spring network with central force plus single bond rotational springs.

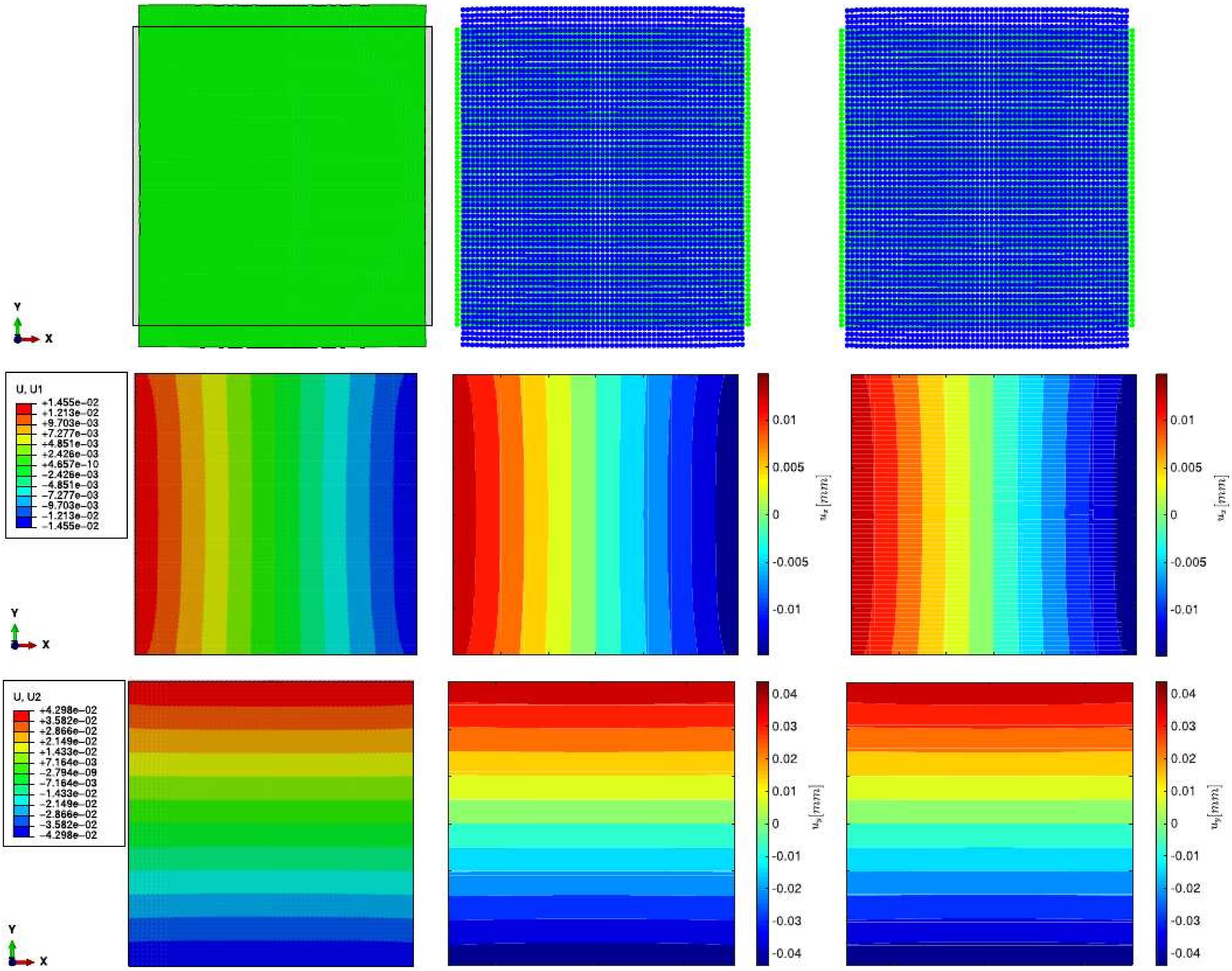

Fig. 14. Simple traction, $\nu = 1/3$: deformed shape and displacements maps obtained with FEM, PDS, MPPD.

where γ is the bond shearing deformation or bond sliding

$$\gamma = \frac{\eta_t}{|\boldsymbol{\xi}|} \tag{18}$$

where η_t is the component of $\boldsymbol{\eta}$ orthogonal to the undeformed bond $\boldsymbol{\xi}$. In this way, the second-order micromodulus tensor $\mathbf{C}(\boldsymbol{\xi})$ in Eq. (3) can be rewritten as

$$\mathbf{C}(\boldsymbol{\xi}) = c(|\boldsymbol{\xi}|)\left[\frac{\boldsymbol{\xi}\otimes\boldsymbol{\xi}}{|\boldsymbol{\xi}|^3}\right] + g(|\boldsymbol{\xi}|)\left[\frac{\mathbf{I}\,|\boldsymbol{\xi}|^2 - \boldsymbol{\xi}\otimes\boldsymbol{\xi}}{|\boldsymbol{\xi}|^3}\right] \tag{19}$$

where $\boldsymbol{I}$ is a second-order unit tensor and $g(|\boldsymbol{\xi}|)$ is the shear micromodulus function. The expression of normal and tangent stiffnesses $k_n = c(|\boldsymbol{\xi}|) = c$ and $k_t = g(|\boldsymbol{\xi}|) = g$ are obtained by equating, for two different homogeneous deformation states, the microelastic energy density of peridynamic continuum with the strain energy density of classical linear elastic homogeneous body (Gerstle et al., 2009). The pairwise bond force can be expressed now as

$$\boldsymbol{f}(\boldsymbol{\eta}, \boldsymbol{\xi}) = \mathbf{C}(\boldsymbol{\xi})\boldsymbol{\eta} = \boldsymbol{f}_n + \boldsymbol{f}_t = c(|\boldsymbol{\xi}|)s\frac{\boldsymbol{\eta_n}}{|\boldsymbol{\eta_n}|} + g(|\boldsymbol{\xi}|)\gamma\frac{\boldsymbol{\eta_t}}{|\boldsymbol{\eta_t}|} \tag{20}$$

For plane-stress and plane-strain conditions, in the case of constant (cylindrical) micromodulus function we obtain (Zhu and Ni, 2017)

$$g(|\boldsymbol{\xi}|) = g = \begin{cases} \dfrac{6E(1-3\nu)}{\pi t \delta^3(1-\nu^2)} & \text{plane stress} \\ \dfrac{6E(1-4\nu)}{\pi t \delta^3(1-2\nu)(1+\nu)} & \text{plane strain} \end{cases} \tag{21}$$

Being in this case $\{b_\gamma\}^T$ defined as

$$\{b_\gamma\}^T = \frac{1}{|\boldsymbol{\xi}|}\{\sin\psi \quad -\cos\psi \quad -\sin\psi \quad \cos\psi\} \tag{22}$$

and relates the bond particles displacements with the bond shear deformation in such a way that

$$\gamma = \{b_\gamma\}^T\{u\} \tag{23}$$

The stiffness matrix is defined at bond level as

$$[K]_{bond} = \frac{c}{|\boldsymbol{\xi}|^3}\alpha\,\Delta V_i \Delta V_j \begin{bmatrix} \xi_x^2 & \xi_x\xi_y & -\xi_x{}^2 & -\xi_x\xi_y \\ \xi_x\xi_2 & \xi_y{}^2 & -\xi_x\xi_y & -\xi_y{}^2 \\ -\xi_x{}^2 & -\xi_x\xi_y & \xi_x{}^2 & \xi_x\xi_y \\ -\xi_x\xi_y & -\xi_y{}^2 & \xi_x\xi_y & \xi_y{}^2 \end{bmatrix}$$

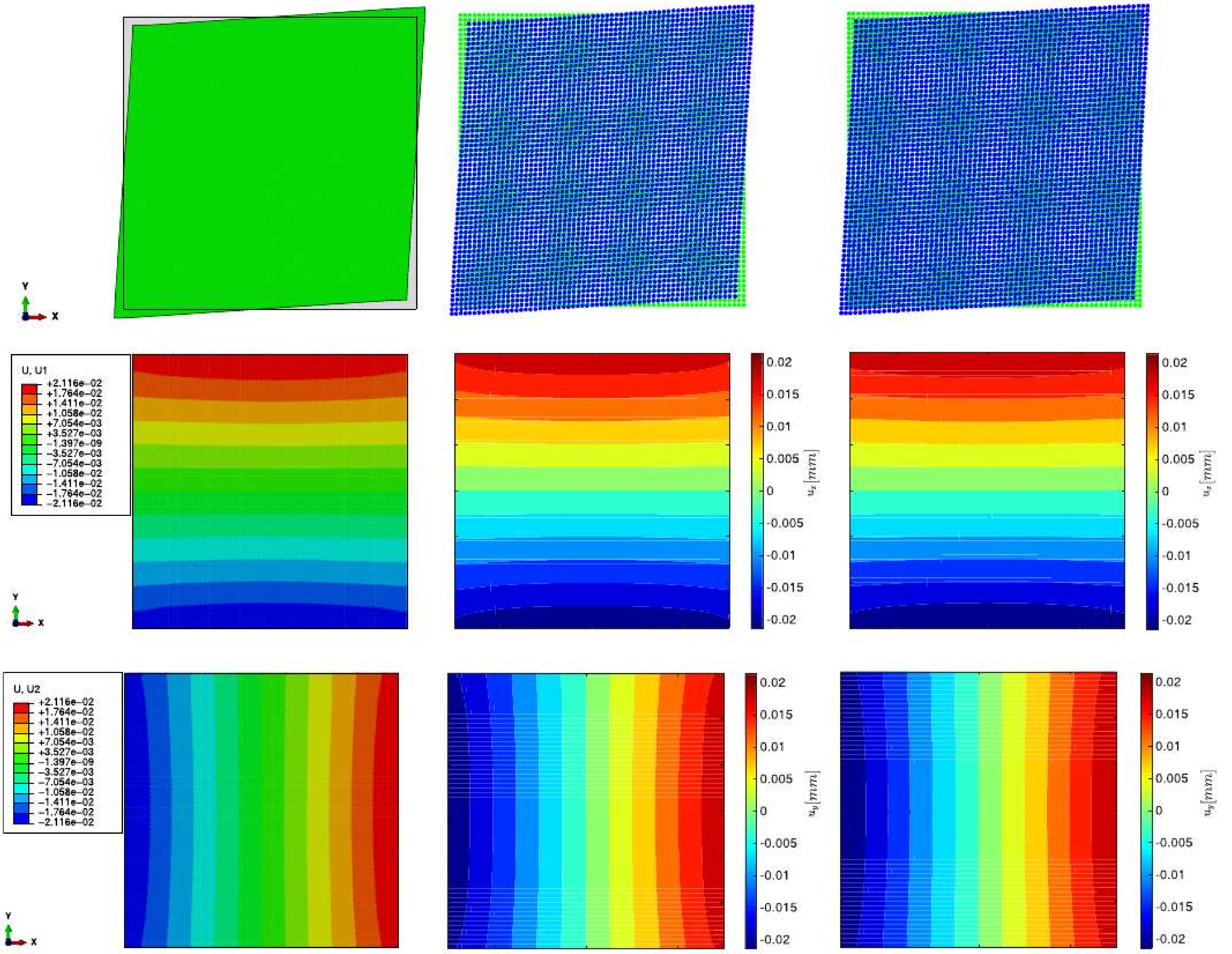

Fig. 15. Pure shear, $\nu = -0.5$: Deformed shape and displacements map obtained with FEM, PDS, MPPD.

$$+\frac{g}{|\boldsymbol{\xi}|^3}\alpha\,\Delta V_i\Delta V_j\begin{bmatrix} \xi_y^2 & -\xi_x\xi_y & -\xi_y{}^2 & \xi_x\xi_y \\ -\xi_x\xi_2 & \xi_x{}^2 & \xi_x\xi_y & -\xi_x{}^2 \\ -\xi_y{}^2 & \xi_x\xi_y & \xi_y{}^2 & -\xi_x\xi_y \\ \xi_x\xi_y & -\xi_x{}^2 & -\xi_x\xi_y & \xi_x{}^2 \end{bmatrix} \tag{24}$$

2.2. A generalized micropolar formulation with shear deformability

In micropolar Peridynamics (MPPD) the particles translational degrees of freedom are augmented to include a rotational degree of freedom θ in two dimension (Gerstle et al., 2009). In this way the original discretized BBPD equation of motion (see Eq. (2)) for any particle i is augmented with a moment equation at time t

$$\sum_{j=1} \mathbf{m}(\mathbf{u}_j - \mathbf{u}_i, \mathbf{X}_j - \mathbf{X}_i)\Delta V_j + \mathbf{c}_i = \mathbf{J}\ddot{\boldsymbol{\theta}}_i \tag{25}$$

where $\mathbf{c}$ denotes the applied body couple or body torque vector and $\ddot{\boldsymbol{\theta}}$ is the angular acceleration vector, while $\mathbf{J}$ denotes the mass moment of inertia tensor per unit volume (the static equilibrium equation is obtained setting the right term of the equation equal to zero). In MPPD each bond connecting two particles i and j can be idealized as an assemblage of two translational spring and a rotational spring. The bond particle's force vector and displacements in local coordinate system (e.g. quantities evaluated at the reference configuration aligned with the X axis, as in Fig. 4) are $\{f\}^T = \{f_n^i \;\; f_t^i \;\; m^i \;\; f_n^j \;\; f_t^j \;\; m^j\}$ and $\{u\}^T = \{u_n^i \;\; u_t^i \;\; \theta^i \;\; u_n^j \;\; u_t^j \;\; \theta^j\}$, respectively. Being this a linearized Micropolar PD formulation, normal and tangential displacements are with respect to coordinate axes that are aligned with the undeformed configuration. In this way we can define three bond deformation parameters, which are functions of the relative displacements in the normal, tangential, and rotational sense, respectively (see Fig. 4). The deformation in the normal direction is the bond stretch s, defined in the same way as in BBPD, thus $s = (u_n^j - u_n^i)/|\boldsymbol{\xi}|$. The shearing deformation or bond sliding is

$$\gamma = \frac{(u_t^j - u_t^i)}{|\boldsymbol{\xi}|} - \frac{(\theta^j + \theta^i)}{2} \tag{26}$$

defined as the difference between the rotation angle of the beam chord and particles average rotation. This latter reduces or increases the bond sliding depending on the mutual rotation sense of the particles itself. In particular, if the two particles rotate with an equal and opposite angle θ, the rotation's contribute to the bond sliding is null. We can also introduce a deformation parameter for the rotational bond spring which is defined by the relative particles rotation measure, or in other words the difference

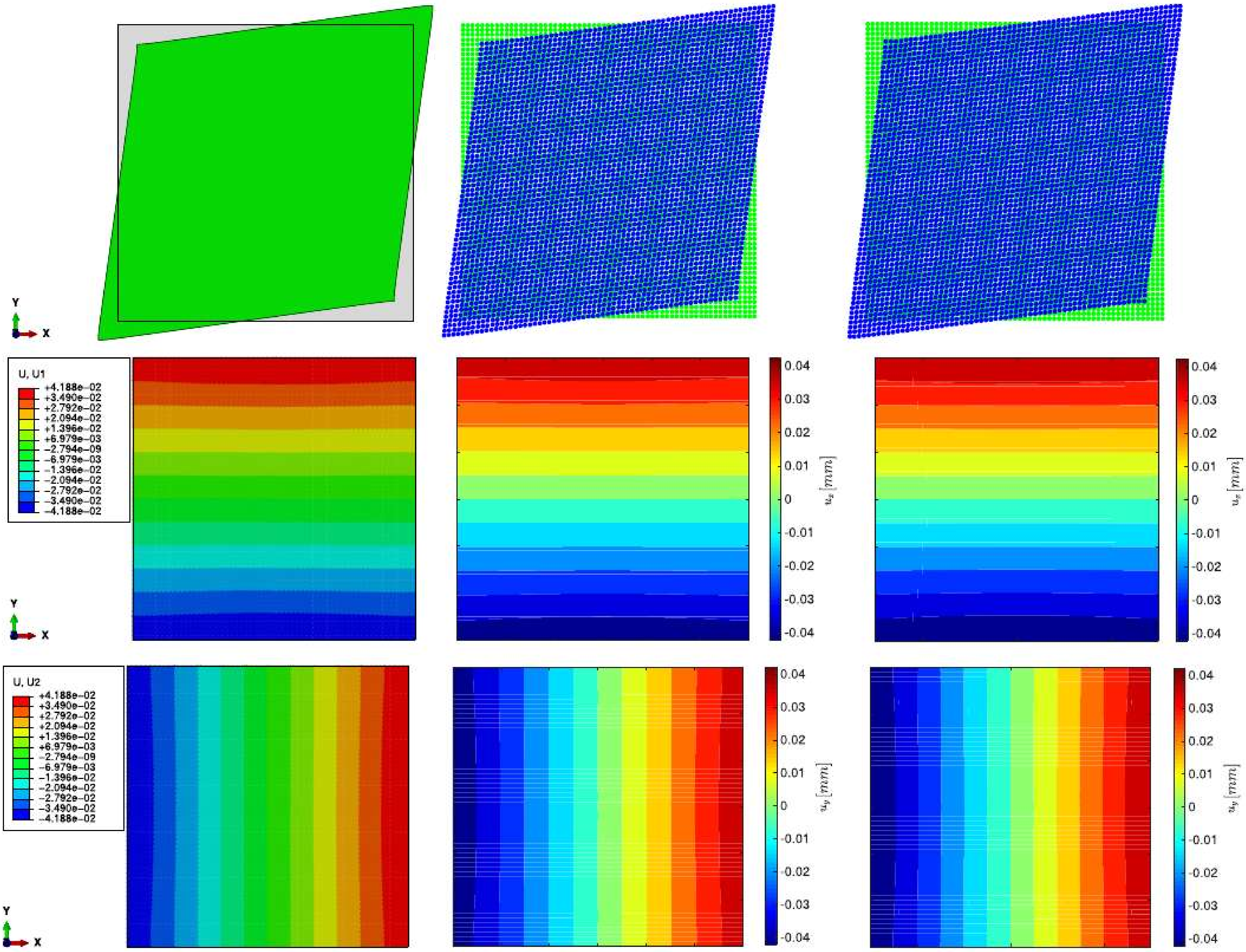

Fig. 16. Pure shear, $\nu = 0$: Deformed shape and displacements map obtained with FEM, PDS, MPPD.

between the rotation angles of the two connected particles

$$\vartheta = (\theta^j - \theta^i) \tag{27}$$

This parameter can be used to improve the bond stretch measure in such a way that

$$s = \frac{(u_n^j - u_n^i) + \vartheta\kappa}{|\boldsymbol{\xi}|} \tag{28}$$

where κ is a scaling parameter which regulates how much bending is considered in the bond stretch measure (for simplicity in this study is set to zero) (Karihaloo et al., 2003; Pan et al., 2018; Lilliu and van Mier, 2003). In this way we can write the kinematic equation relating the particles displacements to the bond deformation parameters

$$\{h\} = [B]^T\{u\} \tag{29}$$

where $\{h\} = \{s \quad \gamma \quad \vartheta\}^T$ is the vector of the springs deformation measures and $[B]^T$ is defined as

$$[B]^T = \frac{1}{|\boldsymbol{\xi}|}\begin{bmatrix} -1 & 0 & 0 & 1 & 0 & 0 \\ 0 & -1 & |\boldsymbol{\xi}|/2 & 0 & 1 & |\boldsymbol{\xi}|/2 \\ 0 & 0 & -|\boldsymbol{\xi}| & 0 & 0 & |\boldsymbol{\xi}| \end{bmatrix} \tag{30}$$

The constitutive behavior of the model is defined by the following relation

$$\{q\} = [D]\{h\} \longrightarrow \begin{Bmatrix} f_n \\ f_t \\ m_\theta \end{Bmatrix} = \begin{bmatrix} k_n & 0 & 0 \\ 0 & k_t & 0 \\ 0 & 0 & k_\theta \end{bmatrix} \begin{Bmatrix} s \\ \gamma \\ \vartheta \end{Bmatrix} \tag{31}$$

where $[D]$ is a diagonal matrix containing the bond normal, tangential, and rotational spring equivalent stiffnesses and relates the pairwise forces and micromoment, (i.e. the peridynamic actions between two particles) to the bond deformation parameters defined above. The pairwise bond moment and forces can be viewed as the springs reactions to the bond deformations s and γ and r, respectively. In particular, the bond forces are equal in modulus to the particles forces ($f_n = f_n^j = -f_n^i$ and $f_t = f_t^j = -f_t^i$) but this is not true for bond and particles moments. In fact, for example m_i and m_j could assume the same nonzero value leading to a bond micromoment m_θ equal to zero. This because in a specific ligament, m_θ represents the self-equilibrated part of the particles micromoments (Fig. 5).

It is worth noting that this is a general micropolar Peridynamic formulation which leads to different centrosymmetric models

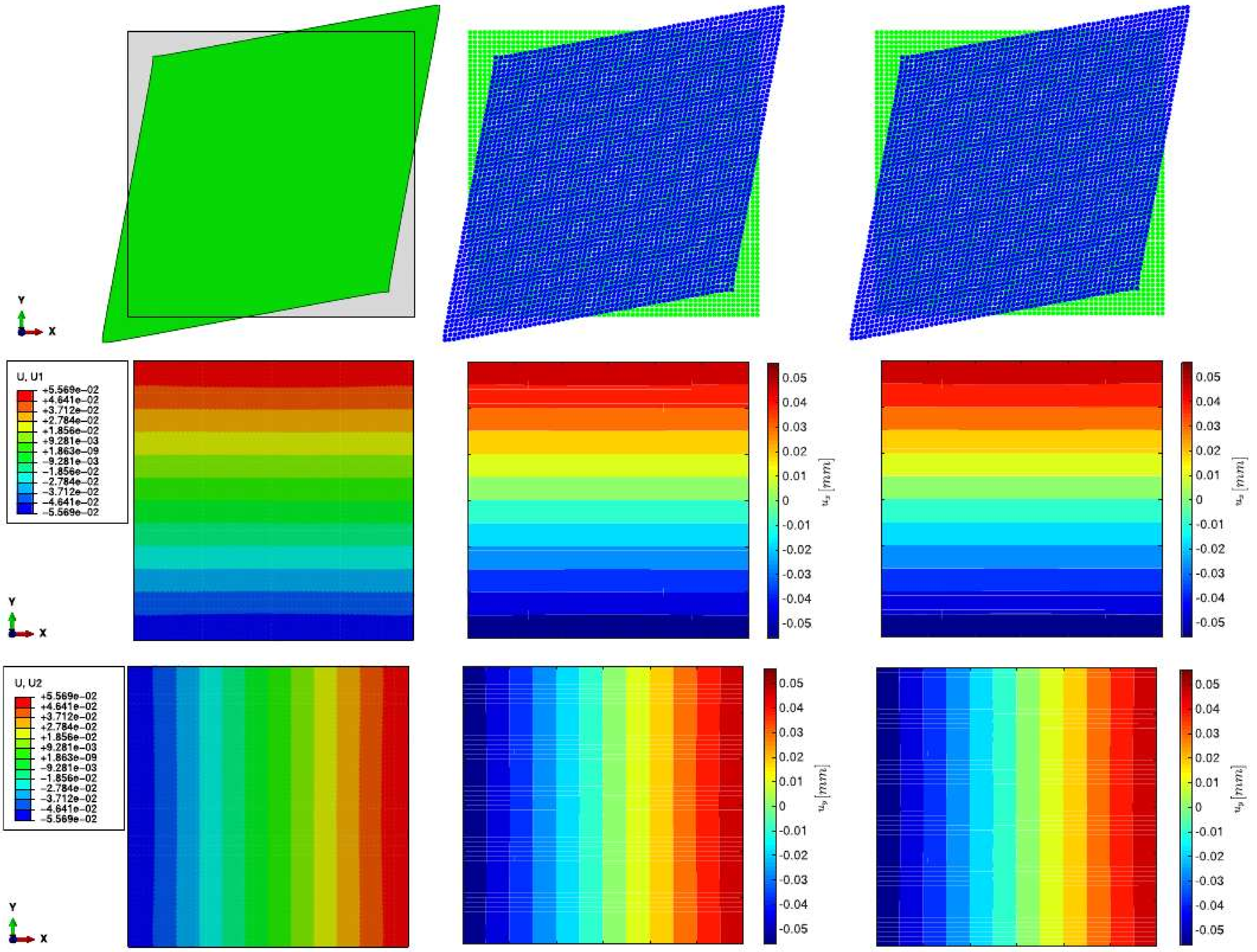

Fig. 17. Pure shear, $\nu = 1/3$: Deformed shape and displacements map obtained with FEM, PDS, MPPD.

depending on the specific constitutive parameters laws k_n, k_t and k_θ adopted.[4]

The general form of the micro elastic energy density $\Phi(\mathbf{X})$ for micropolar peridynamics is obtained by considering the contribution of the three springs and their corresponding deformation measures

$$\Phi(\mathbf{X}) = \frac{1}{2}\int_{H_x} \frac{k_n s^2|\boldsymbol{\xi}|}{2} + \frac{k_t\gamma^2|\boldsymbol{\xi}|}{2} + \frac{k_\theta\vartheta^2}{2} dV_{\mathbf{X}'} \tag{32}$$

In this way, considering Eqs. (30)–(32), the bond stiffness matrix in global coordinate system can be expressed in the following form

$$[K]_{bond} = \alpha|\boldsymbol{\xi}|\Delta V_i\Delta V_j[R]^T[B][D][B]^T[R]$$
$$= \frac{\alpha}{|\boldsymbol{\xi}|}\Delta V_i\Delta V_j[R]^T\begin{bmatrix} k_n & 0 & 0 & -k_n & 0 & 0 \\ 0 & k_t & -k_t|\boldsymbol{\xi}|/2 & 0 & -k_t & -k_t|\boldsymbol{\xi}|/2 \\ 0 & -k_t|\boldsymbol{\xi}|/2 & k_\theta|\boldsymbol{\xi}| + k_t|\boldsymbol{\xi}|^2/4 & 0 & k_t|\boldsymbol{\xi}|/2 & -k_\theta|\boldsymbol{\xi}| + k_t|\boldsymbol{\xi}|^2/4 \\ -k_n & 0 & 0 & k_n & 0 & 0 \\ 0 & -k_t & k_t|\boldsymbol{\xi}|/2 & 0 & k_t & k_t|\boldsymbol{\xi}|/2 \\ 0 & -k_t|\boldsymbol{\xi}|/2 & -k_\theta|\boldsymbol{\xi}| + k_t|\boldsymbol{\xi}|^2/4 & 0 & k_t|\boldsymbol{\xi}|/2 & k_\theta|\boldsymbol{\xi}| + k_t|\boldsymbol{\xi}|^2/4 \end{bmatrix}[R] \tag{33}$$

The relationship between the microelastic constants of an isotropic MPPD model (k_n, k_t) and the conventional macro elastic parameters (E, ν) can be obtained by comparing the micoelastic energy function of micropolar PD model to the conventional strain energy density in elasticity, for two different homogeneous deformation fields. We consider an isotropic expansion ($s_1 = s_2 = s$) and a pure shear deformation of orthogonal PD stretch components $s_1 = -s_2 = s$ (see Fig. 6). The deformation variables s and γ of each bond in Eq. (32), are in general function of the angle of inclination ψ of the ligament. However in the case of isotropic expansion we can write

$$s = s; \qquad \gamma = 0 \tag{34}$$

---

[4] We are considering isotropic material, thus the [D] matrix which describes the constitutive behavior of the bond is not dependent on the orientation angle of the ligament.

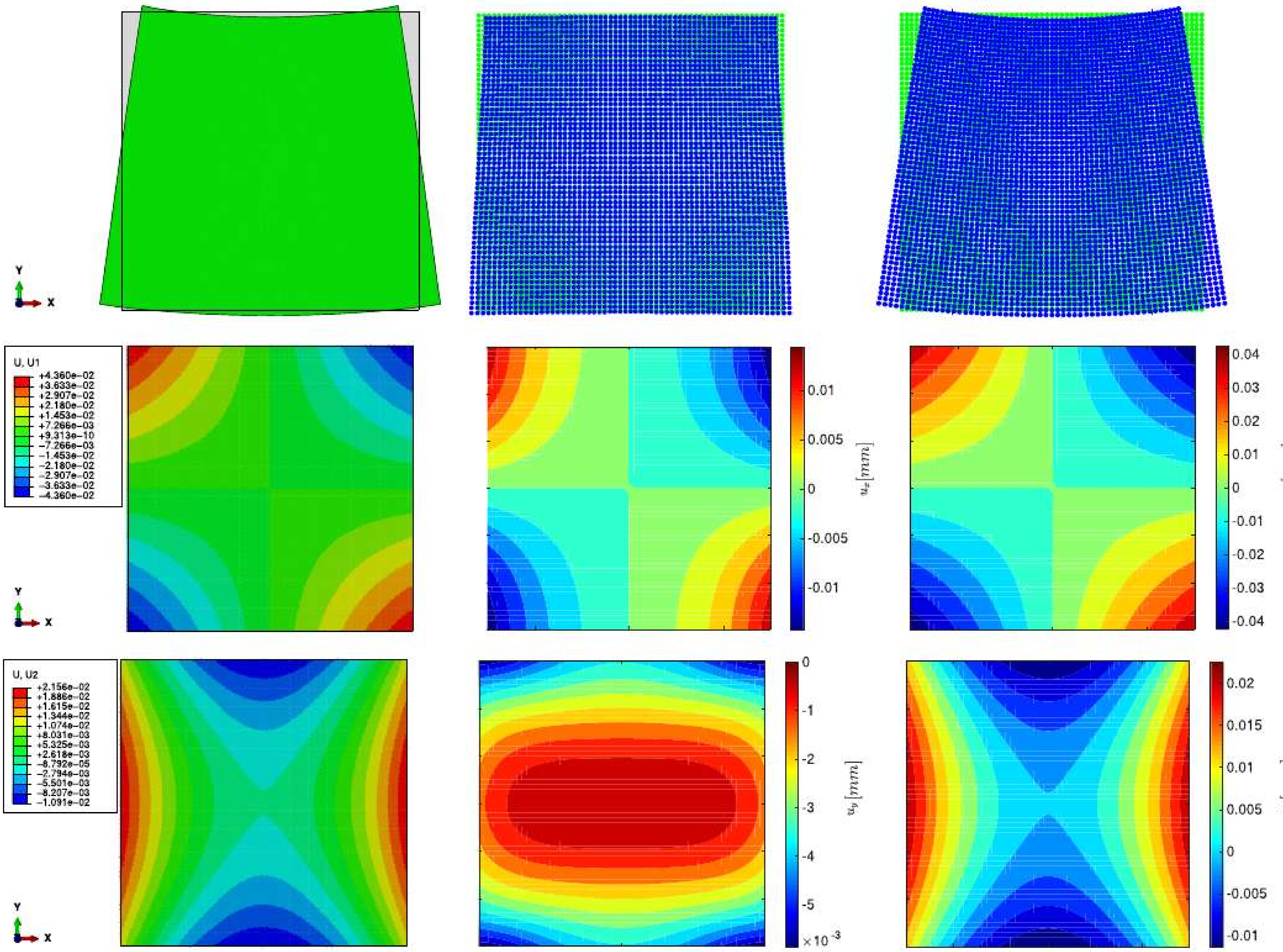

Fig. 18. Simple bending, $\nu = -0.5$: deformed shape, horizontal and vertical displacements map obtained with FEM, PDS, MPPD.

considering also that $c = k_n$ and that for homogeneous deformation fields $\vartheta = 0$. In this way, from Eq. (32) we obtain

$$\Phi(\mathbf{X}) = \frac{1}{2}\int_{H_x} \frac{k_n s^2 |\boldsymbol{\xi}|}{2} dV_{\mathbf{X}'} = \frac{1}{2}\int_{H_x} \frac{k_n t s^2 |\boldsymbol{\xi}|}{2} dA_{\mathbf{X}'}$$
$$= \frac{1}{2}\int_0^{\delta} \frac{2k_n t\pi s^2 |\boldsymbol{\xi}|^2}{2} d\xi = \frac{k_n t\pi s^2 \delta^3}{6} \tag{35}$$

In the conventional continuum mechanics, for the elastic solids under isotropic expansion, the linear elastic strain energy density function for plane stress can be written as

$$\frac{1}{2}C_{ij}\epsilon_i\epsilon_j = \frac{E}{2(1-\nu^2)}\begin{bmatrix} 1 & \nu & 0 \\ \nu & 1 & 0 \\ 0 & 0 & \frac{1-\nu}{2} \end{bmatrix}\begin{Bmatrix} s \\ s \\ 0 \end{Bmatrix} \cdot \begin{Bmatrix} s \\ s \\ 0 \end{Bmatrix} = \frac{Es^2}{1-\nu} \tag{36}$$

whereas for plane strain is

$$\frac{1}{2}C_{ij}\epsilon_i\epsilon_j = \frac{E}{2(1-2\nu)(1+\nu)}\begin{bmatrix} 1-\nu & \nu & 0 \\ \nu & 1-\nu & 0 \\ 0 & 0 & \frac{1-2\nu}{2} \end{bmatrix}\begin{Bmatrix} s \\ s \\ 0 \end{Bmatrix} \cdot \begin{Bmatrix} s \\ s \\ 0 \end{Bmatrix}$$
$$= \frac{Es^2}{(1-2\nu)(1+\nu)} \tag{37}$$

In the case of pure shear deformation, instead, s and γ in Eq. (32) are function of the angle ψ according to

$$s = s\cos(2\psi); \qquad \gamma = \gamma\sin(2\psi) \tag{38}$$

so that

$$\Phi(\mathbf{X}) = \frac{1}{2}\int_{H_x} \frac{k_n s^2\cos^2(2\psi)|\boldsymbol{\xi}|}{2} + \frac{k_t\gamma^2\sin^2(2\psi)|\boldsymbol{\xi}|}{2} dV_{\mathbf{X}'}$$
$$= \frac{1}{2}\int_0^{\delta} 4\int_0^{\pi/2} \frac{k_n t s^2\cos^2(2\psi)|\boldsymbol{\xi}|}{2}$$
$$+ \frac{k_t t\gamma^2\sin^2(2\psi)|\boldsymbol{\xi}|}{2} d\psi\, d\xi$$
$$= \int_0^{\delta} \frac{k_n t s^2\left[4\psi + \sin(4\psi)\right]|\boldsymbol{\xi}|^2}{8}$$
$$+ \frac{k_t t\gamma^2\left[4\psi - \sin(4\psi)\right]}{8}\Bigg|_0^{\pi/2} d\xi$$
$$= \frac{k_n t\pi s^2\delta^3}{12} + \frac{k_t t\pi\gamma^2\delta^3}{12} \tag{39}$$

The conventional linear elastic strain energy density function for plane stress conditions is obtained by

$$\frac{1}{2}C_{ij}\epsilon_i\epsilon_j = \frac{E}{2(1-\nu^2)}\begin{bmatrix} 1 & \nu & 0 \\ \nu & 1 & 0 \\ 0 & 0 & \frac{1-\nu}{2} \end{bmatrix}\begin{Bmatrix} s \\ -s \\ 0 \end{Bmatrix} \cdot \begin{Bmatrix} s \\ -s \\ 0 \end{Bmatrix} = \frac{Es^2}{1+\nu} \tag{40}$$

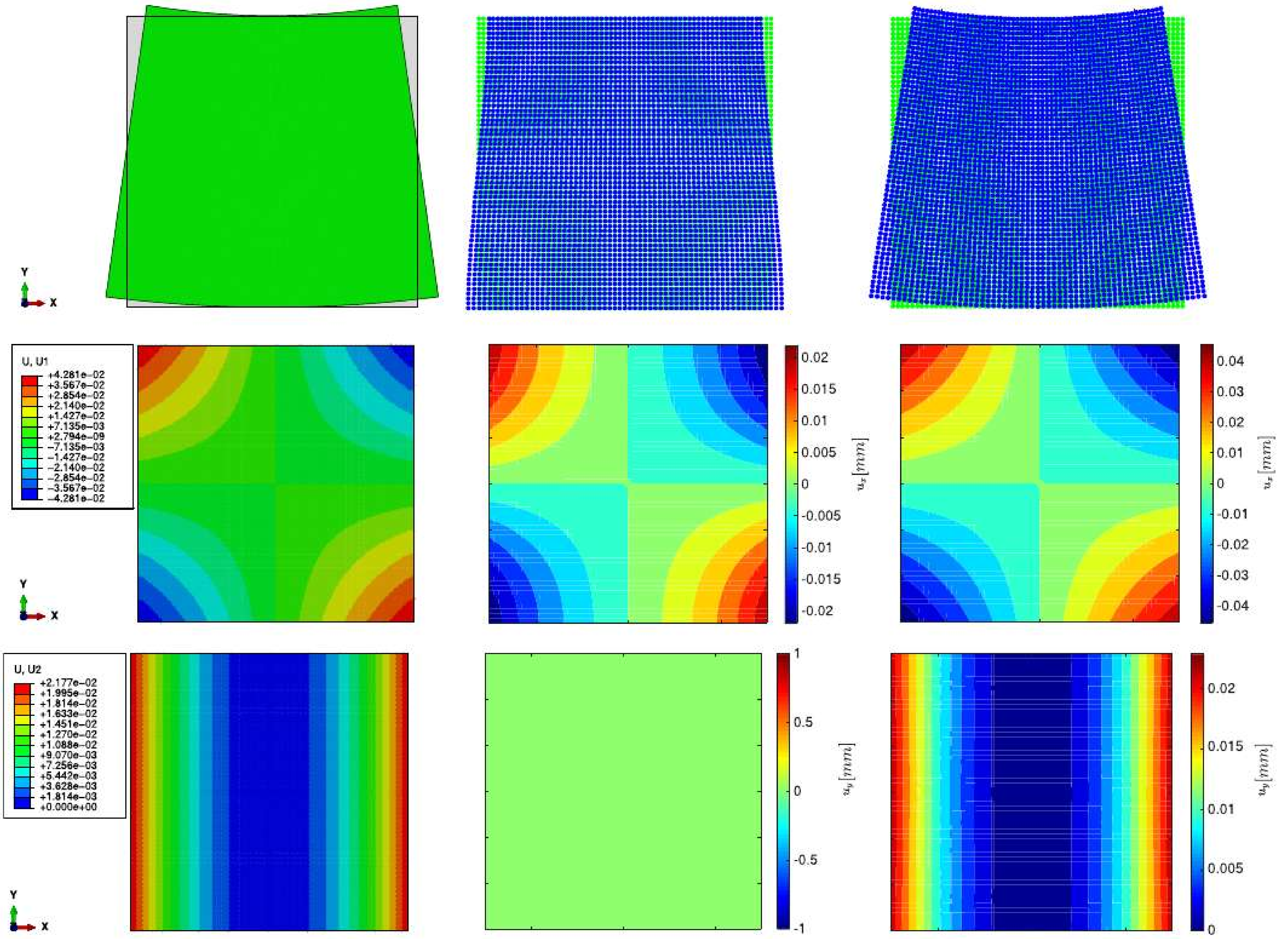

Fig. 19. Simple bending, $\nu = 0$: deformed shape and displacements map obtained with FEM, PDS, MPPD.

whereas for plane strain is

$$\frac{1}{2}C_{ij}\epsilon_i\epsilon_j = \frac{E}{2(1-2\nu)(1+\nu)}\begin{bmatrix}1-\nu & \nu & 0\\ \nu & 1-\nu & 0\\ 0 & 0 & \frac{1-2\nu}{2}\end{bmatrix} \begin{Bmatrix}s\\-s\\0\end{Bmatrix}\cdot\begin{Bmatrix}s\\-s\\0\end{Bmatrix} = \frac{Es^2}{1+\nu}; \qquad (41)$$

Solving the systems of Eqs. (35)–(37) and Eqs. (39)–(41) for k_n and k_t, we obtain Eq. (7) for $k_n = c$ and Eq. (21) for $k_t = g$. Thus, we can consider the PDS model as a special case of the conceived generalized MPPD formulation when the rotational degree of freedom is not taken into account or is kept restrained. It is worth noting that, contrarily to the PDS formulation, the MPPD model here presented is a proper micropolar peridynamic model. The definition of a shearing deformation measure which does not account for particle rotations, leads to an incorrect description of the mechanical behavior of materials undergoing non-homogeneous deformation fields, as will be shown in the next section. However, when referring to an equivalent Cauchy continuum, a specific value of the rotational spring constant k_θ is not strictly required, so that an almost arbitrary value of k_θ can be chosen in the equivalent micropolar lattice model and could be calibrated in such a way to reduce the size effect, an intrinsic feature of micropolar models.

In any case, since the introduction of rotational degrees of freedom into the lattice spring models provides the stiffness matrix resembling the beam stiffness matrix, beams come as a natural choice to represent (non-local) lattice elements (Nikolić et al., 2017). The micro-elastic energy of a micropolar peridynamic solid with frame-like ligaments connecting particles, thus a 2D non-local lattice with Euler-Bernoulli beam-like microstructure (i.e. Gerstle's model Gerstle et al. (2007)), is a particular case of the model described in Eqs. (32), (33) and may be obtained by setting in Eq. (31)

$$\begin{aligned} k_n &= c\\ k_t &= 12d/|\boldsymbol{\xi}|^2\\ k_\theta &= d/|\boldsymbol{\xi}| \end{aligned} \qquad (42)$$

where the independent elastic constants are only two, since $k_t = f(k_\theta)$. In this specific case, by equating the micro-elastic energy of MPPD to the strain energy of continuum corresponding to two different homogeneous deformation states, we obtain[5]

$$d(|\boldsymbol{\xi}|) = d = \begin{cases} \frac{E(1-3\nu)}{6\pi t\delta(1-\nu^2)} & \text{plane stress}\\ \frac{E(1-4\nu)}{6\pi t\delta(1-2\nu)(1+\nu)} & \text{plane strain} \end{cases} \qquad (43)$$

The stiffness d corresponding to shear deformation is a generalized stiffness which can satisfy the condition $r > 0$, $r < 0$, or $r = 0$.

---

[5] The axial stiffnesses are the same as in Eq. (7). It is important to notice that in general we need three different deformation states to calibrate the elastic bond stiffnesses, one of which is a non-homogeneous deformation state (i.e. a microrotational self-equilibrated state corresponding to $m_\theta = k_\theta\,\vartheta$).

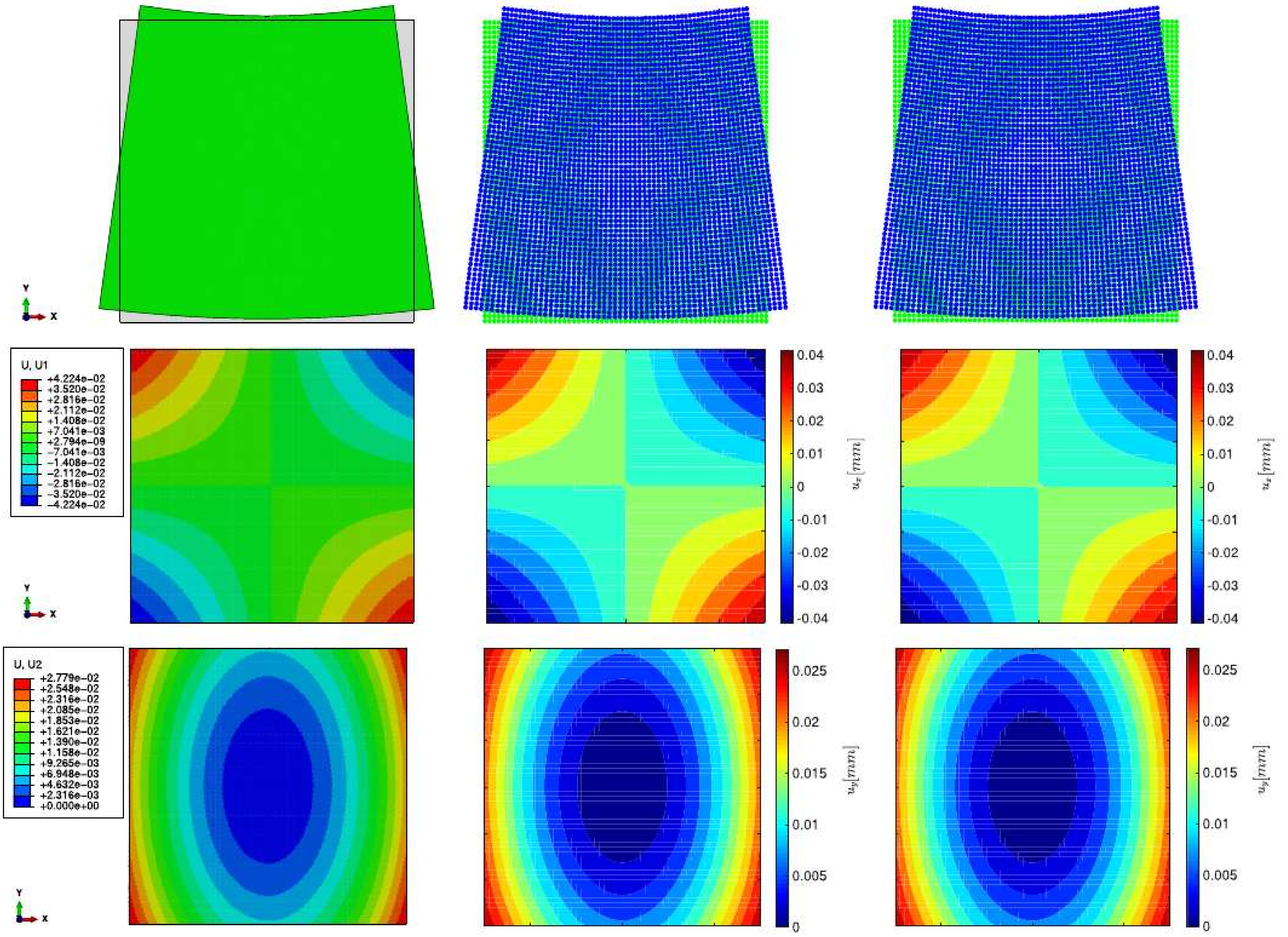

Fig. 20. Simple bending, $\nu = 1/3$: deformed shape, and displacements map obtained with FEM, PDS, MPPD.

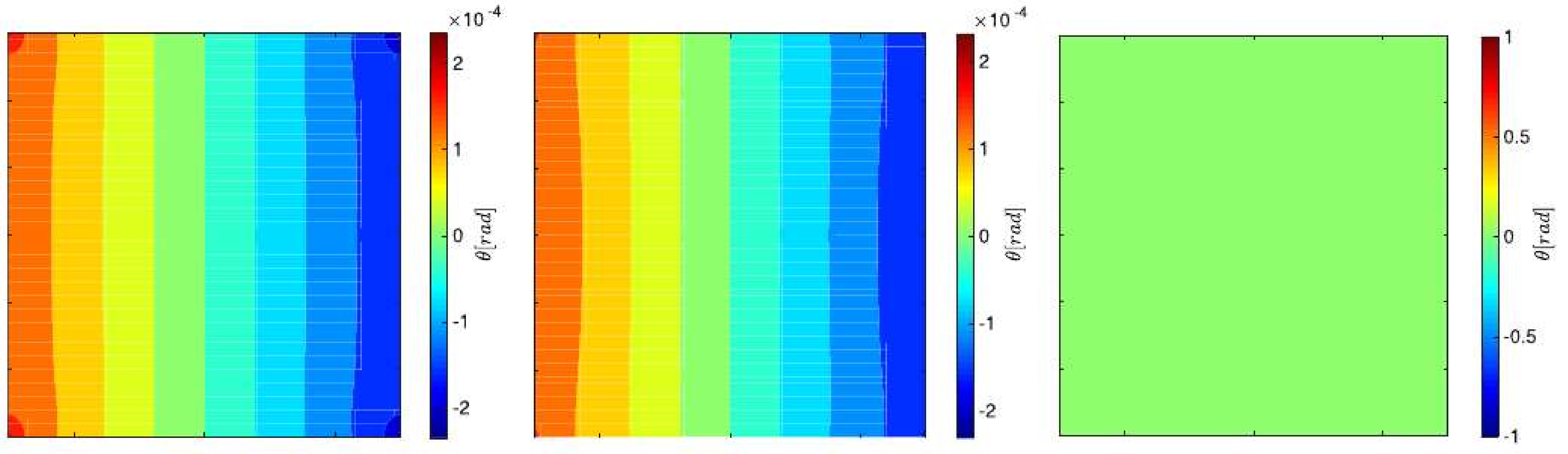

Fig. 21. Simple bending: microrotations θ maps obtained with MPPD model setting $\nu = -0.5$ (sx), $\nu = -0.5$ and $\nu = 1/3$ (dx).

The case of $r = 0$, corresponding to $\nu = 1/3$ in plane stress and $\nu = 1/4$ in plane strain, is equivalent to considering a microelastic energy potential which is function only of the peridynamic bond stretch (being a bond shear deformation measure still definable in this condition). In the case of shear spring stiffness $r < 0$, the corresponding Poisson's ratio is larger than BBPD fixed values. A physical interpretation of negative shear spring stiffness, starting from molecular-dynamics consideration was given by Zhao and Zhao (2012). Moreover Eq. (43) show that auxeticity in isotropic materials requires the flexural part to be predominant (François et al., 2017). Altough Eq. (43) comes from the analogy of a Euler-Bernoulli (EB) beam element from solid mechanics, we should not think of physical bonds. In fact, there is no account taken in this model of the actual presence of moments and curvature change of spring bonds connecting the neighboring nodes. Instead, pairwise bond forces simply relates to bond deformations in a way that is similar to that in a EB beam element in solid mechanics (Gerstle et al., 2009).

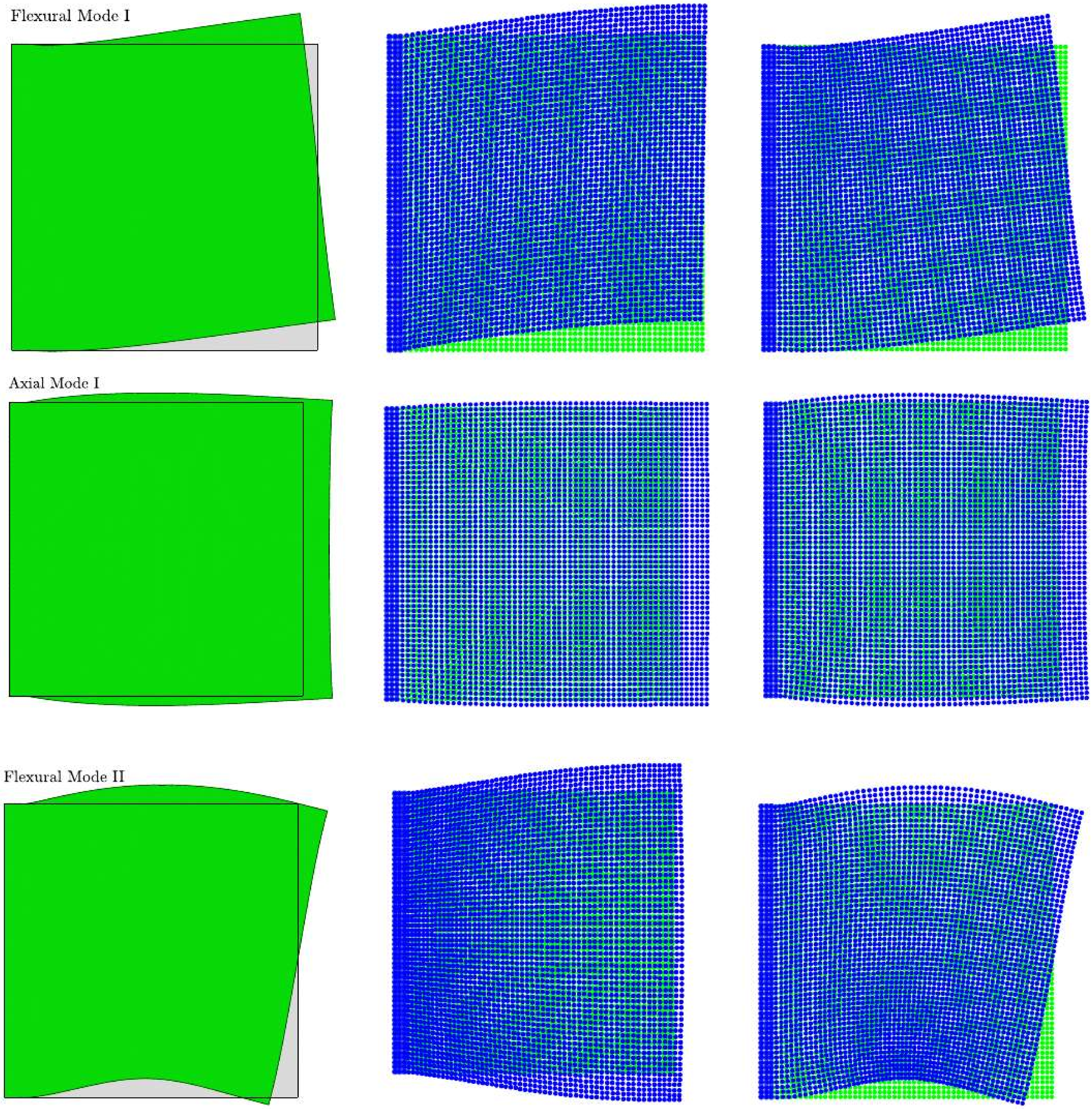

Fig. 22. Natural Frequencies of the cantilever square lamina, $\nu = -0.5$: deformed shapes obtained with FEM, PDS, MPPD.

2.2.1. Failure conditions and local damage variables

In this section different deformation-based[6] failure criteria related to the different equivalent springs defined above are introduced. The first criterion analyzed here is that of maximum bond stretch (Silling and Askari, 2005). We consider a modified prototype-microelastic constitutive law with different tensile and compressive pairwise force-bond stretch relationships. The values of the stretch s_{0t}, and s_{0c}, corresponding to the reaching of the elastic limit in tension and compression, respectively, are calculated on the basis of a homogenization process of the materials of which the solid considered is made of, and can be estimated as

$$s_{0t} = \sigma_{0t}/\mathrm{E}; \qquad s_{0c} = \sigma_{0c}/\mathrm{E} \tag{44}$$

where σ_{0t}, σ_{0c} are the tensile and compressive uniaxial elastic limit stress and E is the elastic modulus of the homogenized material. The ultimate tensile stretch limit, s_{ut}, and the ultimate compressive stretch limits, s_{uc}, are related instead to the fracture energy G_{fl}, and uniaxial compressive energy absorption capacity of the material (Yaghoobi and Chorzepa, 2017; Gerstle et al., 2009). In this way we refer only to the mechanical behavior of the equivalent axial spring, because of the strain control is carried out exclu-

---

[6] We refer to deformation-based yield criteria for peridynamic solids and we do not consider failure corresponding to $m_\theta - \vartheta$ bond constitutive law. These initial yield conditions are focused on the ultimate deformations, instead of the tensile stresses.

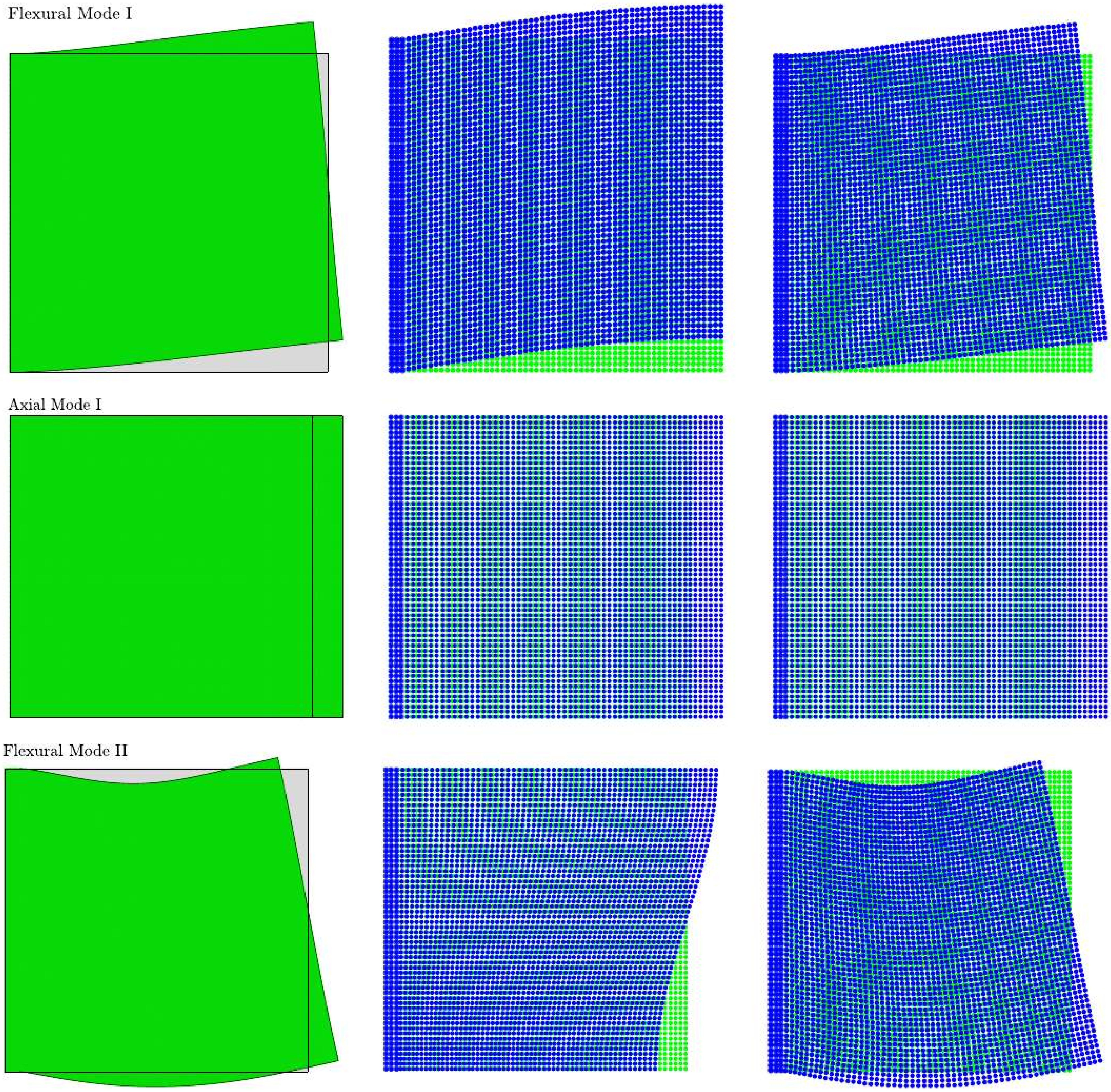

Fig. 23. Natural Frequencies, $\nu = 0$: deformed shapes obtained with FEM, PDS, MPPD.

sively on the bond stretch measure (see Fig. 7). In order to specify the status of a specific bond $\boldsymbol{\xi}_{ij}$ connecting two particles $\mathbf{X}_i$ and $\mathbf{X}_j$, a history-dependent scalar valued function μ in tension and in compression is introduced (Silling and Askari, 2005)

$$\mu_t(\boldsymbol{\xi}_{ij}, t) = \begin{cases} 0 & s \geq s_{ut} \\ \dfrac{s_{ut} - s}{s_{ut} - s_{0t}} & s_{0c} \leq s < s_{ut} \\ 1 & s < s_{0t} \end{cases} \tag{45}$$

$$\mu_c(\boldsymbol{\xi}_{ij}, t) = \begin{cases} 0 & s \leq s_{uc} \\ \dfrac{s_{uc} - s}{s_{uc} - s_{0c}} & s_{uc} < s \leq s_{0c} \\ 1 & s > s_{0c} \end{cases} \tag{46}$$

Then, based on functions $\mu_t(\boldsymbol{\xi}_{ij}, t)$ and $\mu_c(\boldsymbol{\xi}_{ij}, t)$, a local tensile and compressive damage variable is defined and computed for each step t and for each particle $\mathbf{X}_i$ as

$$d_t(\mathbf{X}_i, t) = 1 - \frac{\sum_{j=1} \mu_t(\boldsymbol{\xi}_{ij}, t) \Delta V_j}{\sum_{j=1} \Delta V_j} \tag{47}$$

$$d_c(\mathbf{X}_i, t) = 1 - \frac{\sum_{j=1} \mu_c(\boldsymbol{\xi}_{ij}, t)\, \alpha\, \Delta V_j}{\sum_{j=1} \alpha\, \Delta V_j} \tag{48}$$

where d_t is the local tensile damage and d_c is the local compressive damage. The numerator in the fractions represents the actual damaged volume of the unit cell considered, in tension and in compression, respectively, whereas the denominator is the volume of the family of particle $\mathbf{X}_i$ in the undeformed configuration.

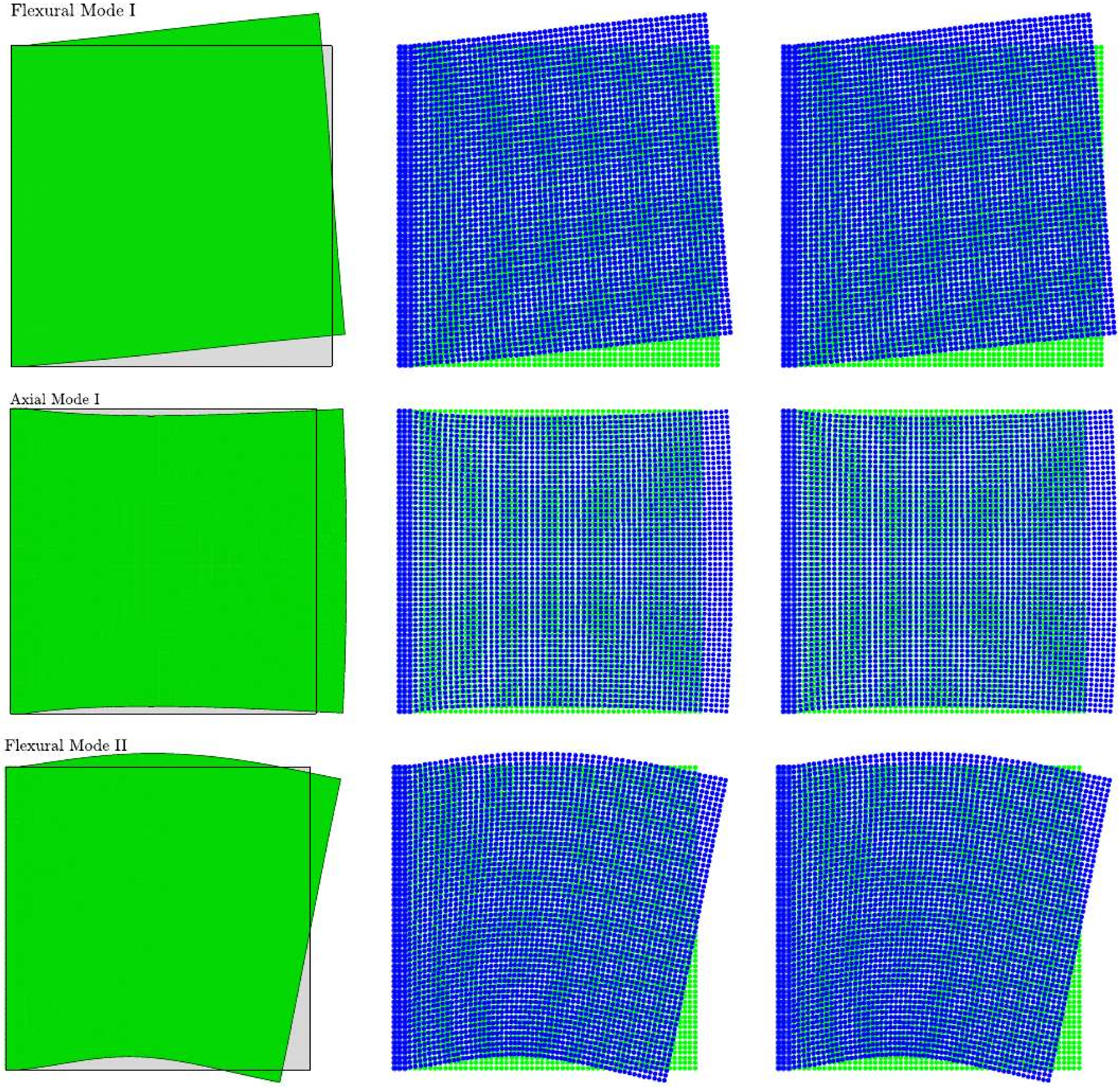

Fig. 24. Natural Frequencies, $\nu = 1/3$: deformed shapes obtained with FEM, PDS, MPPD.

The failure condition in $s - \gamma$ plane (i.e. the generalized deformations 2D space) and in principal peridynamic stretch $s_1 - s_2$ space, corresponding to a sample case in which $s_{0c} = -3s_{0t}$, is showed in Fig. 8.

By considering the bond shear force-bond shear deformation (namely bond sliding) constitutive law we can define another yield condition based this time on the definition of a maximum value of bond shearing deformation. This value has to be the same whatever the deformation is positive or negative because of geometric considerations (see Fig. 7).

In analogy with the maximum shear stress model of the continuum in which $\tau_0 = \sigma_{0t}/2$, being $\tau_0 = \hat{\gamma}_0 \mathrm{G}$ and $\hat{\gamma}_0 = 2\gamma_0$ in uniaxial tests, we can write

$$\gamma_0 = \gamma_l = \frac{\tau_0}{2\mathrm{G}} = \frac{\sigma_{0t}}{4\mathrm{G}} = \frac{s_{0t}}{4}\frac{\mathrm{E}}{\mathrm{G}} = \frac{s_{0t}}{2}(1+\nu) \tag{49}$$

where G and ν are the shear modulus and Poisson's ratio of the material considered (see Fig. 9).The post-elastic behavior can be modeled for example as perfectly plastic, however, in some applications, an ultimate bond shear deformation γ_u value can be considered and estimated by using energetic approaches (Rabczuk and Ren, 2017; Foster et al., 2011; Wang et al., 2018). The failure conditions in $s - \gamma$ plane are showed in Fig. 9. As in the case of maximum stretch criterion, a specific history-dependent scalar valued function is introduced in order to state the conditions of the bond $\boldsymbol{\xi}_{ij}$

$$\mu_\gamma(\boldsymbol{\xi}_{ij}, t) = \begin{cases} 0 & \gamma \geq \gamma_u \\ \frac{\gamma_u - \gamma}{\gamma_u - \gamma_0} & \gamma_0 \leq \gamma < \gamma_u \\ 1 & \gamma < \gamma_0 \end{cases} \tag{50}$$

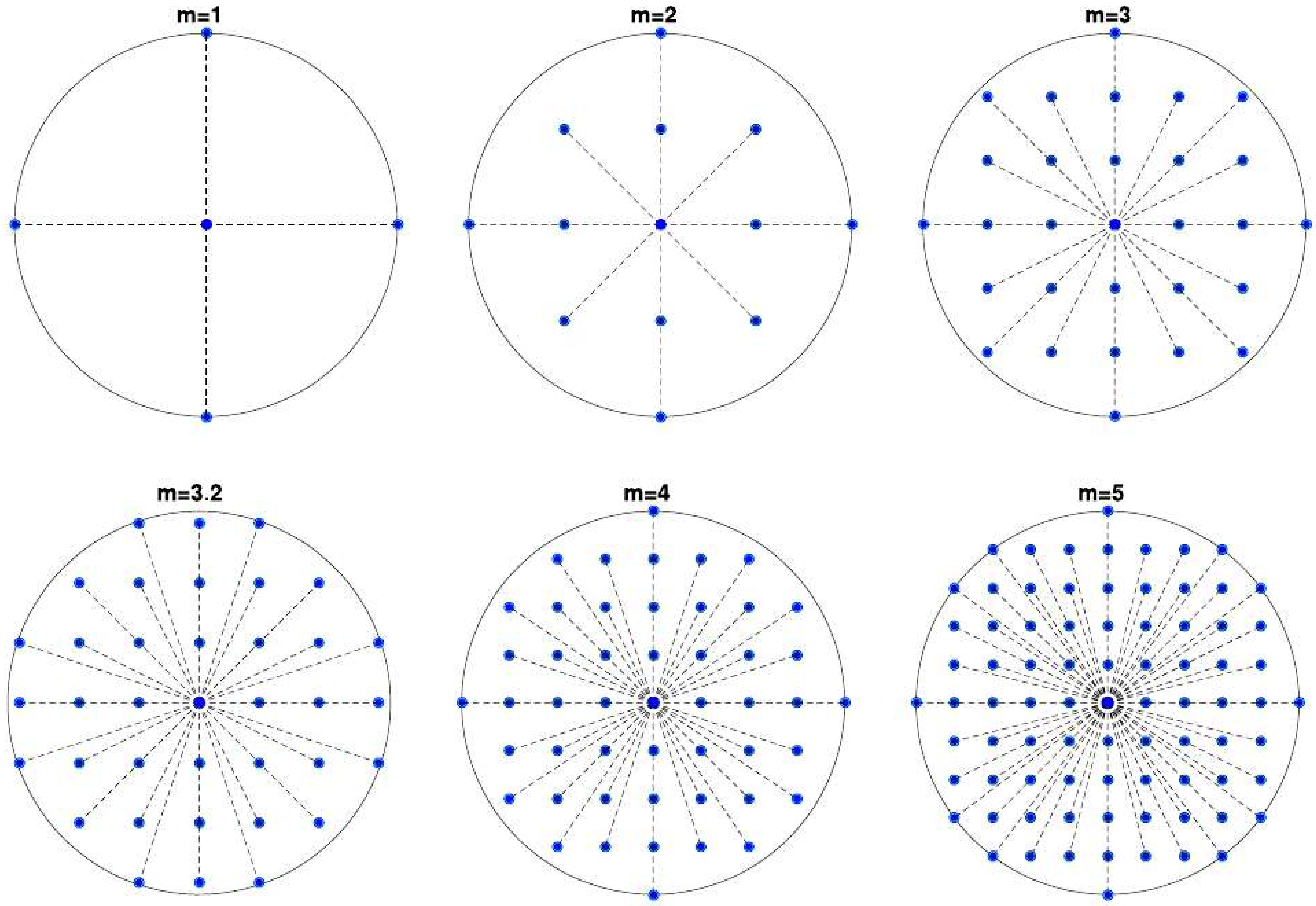

Fig. 25. Definition of the family H_x of the particles i in the case of: m = 1 (4 ligaments with 2 orthogonal directions), m = 2 (12 ligaments with 3 different directions), m = 3 (28 ligaments with 5 different directions), m = 3.2 (36 ligaments with 7 different directions), m=4 (48 ligaments with 9 different directions), m=5 (80 ligaments with 13 different directions).

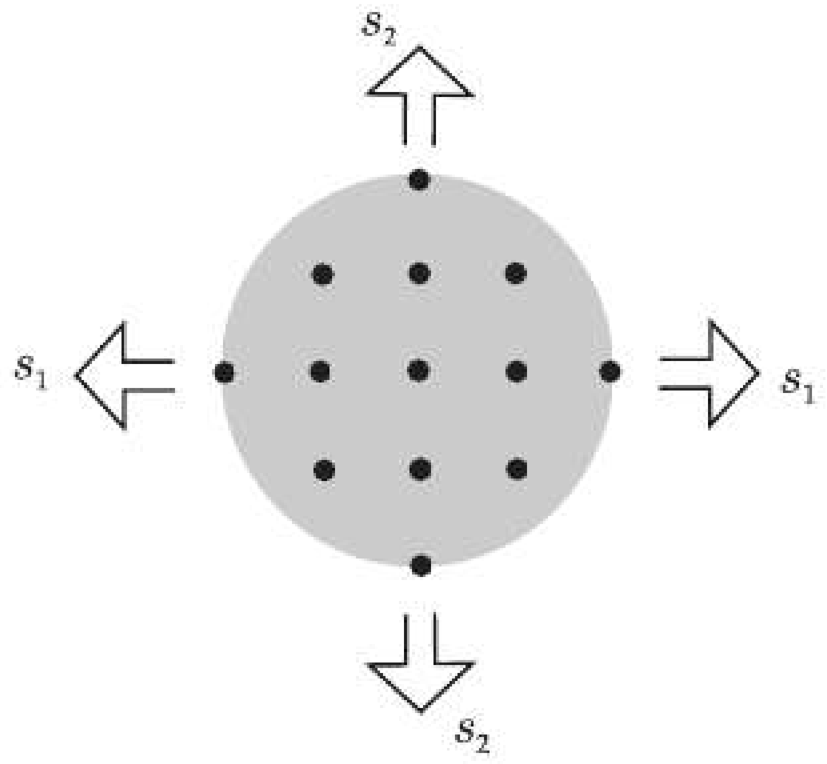

Fig. 26. Schematics of family H_x subjected to orthogonal stretch components s_1 and s_2. Each deformation state is rotated of an angle $-\pi/2 \geq \theta \geq 0$ so that one hundred different orientation are considered.

The shear damage scalar parameter is thus defined as

$$d_\gamma(\mathbf{X}, t) = 1 - \frac{\sum_{j=1} \mu_\gamma(\boldsymbol{\xi}_{ij}, t)\, \alpha\, \Delta V_j}{\sum_{j=1} \alpha\, \Delta V_j} \tag{51}$$

where $\sum_{j=1} \mu_\gamma(\boldsymbol{\xi}_{ij}, t)\, \alpha\, \Delta V_j$ is the actual damaged volume of the unit cell considered, due to the attainment of the shear deformation limit γ_0 in one or more ligaments. The theoretical first yield domain corresponding to the maximum sliding criterion calibrated on the results of a uniaxial tensile test is thus dependent on the Poisson's ratio of the material (see Fig. 9).

Finally we can adopt a frictional sliding yield criterion by considering a bond shear deformation limit which is a function of the corresponding stretch s of the ligament. By analogy with the Mohr-Coulomb model where the shear stress strength is enhanced by the normal compressive stress, according to the condition

$$\tau_l = -\sigma\, \tan\phi' + c' \tag{52}$$

where c' and ϕ' are the cohesion and the internal friction angle of the material, respectively, we can derive the corresponding tensile and compressive bond stretch limit values as

$$s_{0t} = \frac{\sigma_{0t}}{E} = \frac{1}{E}\frac{2c'\cos\phi'}{1+\sin\phi'} \tag{53}$$

$$s_{0c} = \frac{\sigma_{0c}}{E} = \frac{1}{E}\frac{2c'\cos\phi'}{1-\sin\phi'} \tag{54}$$

thus

$$a = s_{0t}\frac{1+\sin\phi'}{2\cos\phi'}\frac{\mathrm{E}}{2\mathrm{G}} = \frac{s_{0t}}{2}(1+\nu)\frac{1+\sin\phi'}{\cos\phi'} \tag{55}$$

$$\beta = tan^{-1}\left(\frac{\mathrm{E}}{2\mathrm{G}}\tan\phi'\right) = \tan^{-1}[(1+\nu)\tan\phi'] \tag{56}$$

since

$$\frac{\sigma_{0t}}{\sigma_{0c}} = \frac{s_{0t}}{s_{0c}} = \frac{1-\sin\phi'}{1+\sin\phi'}; \qquad c' = 2a\,\mathrm{G} \tag{57}$$

The yield condition is then written as

$$\gamma_l = -s\, \tan\beta + a \tag{58}$$

where β is the slope of the initial failure locus in $s - \gamma$ space and a is the shear deformation limit corresponding to $s = 0$. The estimated values of tensile and compressive stretch limits that can be used as cut-off values in tension and in compression, respectively,

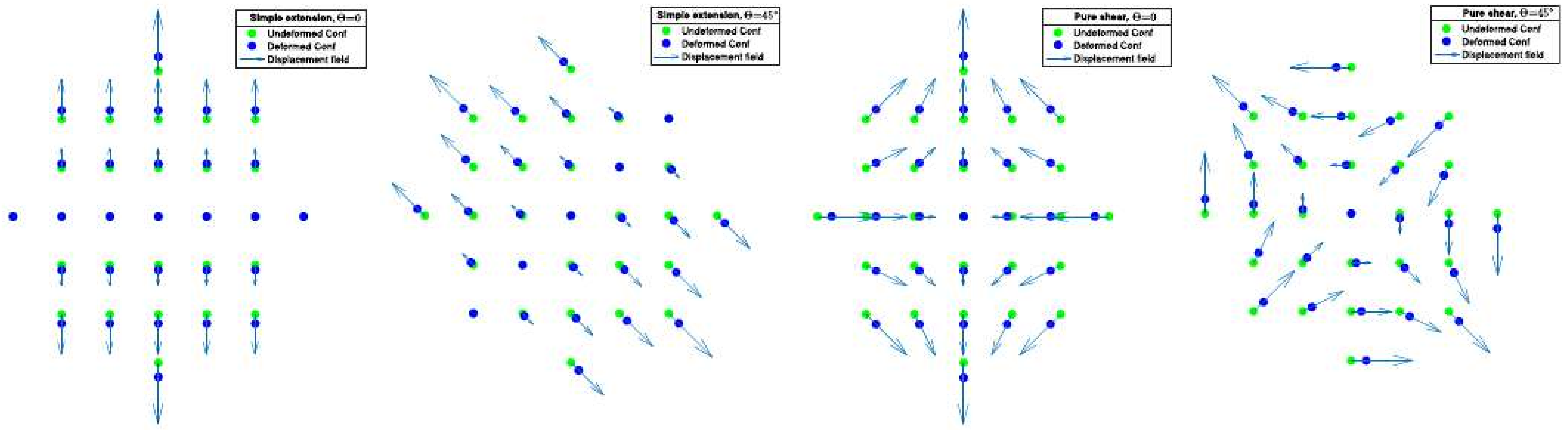

Fig. 27. Deformed configuration of the unit cell corresponding to simple extension and pure shear states in the case of $\Theta = 0$ and $\Theta = \pi/4$: example with $m = 3$.

Table 1
Simple traction: numerical errors and absolute maximum displacements (mm) obtained with FE, PDS and MPPD models.

ν	u_x (FEM)	u_x (PDS)	u_x (MPPD)	u_y (FEM)	u_y (PDS)	u_y (MPPD)	ν (PDS)	ν (MPPD)
−0.5	0.02183	0.02142	0.02161	0.04416	0.04294	0.04469	−0.499	−0.501
0	0.00000	0.00000	0.00000	0.04286	0.04303	0.04439	0	0
0.1	0.00433	0.00431	0.00446	0.04290	0.04309	0.04413	0.100	0.101
0.25	0.01092	0.01085	0.01114	0.04295	0.04326	0.04283	0.252	0.259
1/3	0.01455	0.04156	0.04156	0.04298	0.04156	0.04156	0.339	0.339

Table 2
Pure shear: numerical errors and absolute maximum displacements (mm) obtained with FE, PDS and MPPD models.

G	u_x (FEM)	u_x (PDS)	u_x (MPPD)	u_y (FEM)	u_y (PDS)	u_y (MPPD)	G (PDS)	G (MPPD)
70000	0.02116	0.02138	0.02095	0.02116	0.02138	0.02055	73698	74276
35000	0.04188	0.04223	0.04145	0.04188	0.04223	0.04145	35687	35673
31818	0.04602	0.04636	0.04661	0.04602	0.04636	0.04661	32314	31689
28000	0.05223	0.05255	0.05428	0.05223	0.05255	0.05428	28277	27242
26250	0.05569	0.05586	0.05586	0.05569	0.05586	0.05586	26461	26461

as Fig. 10 shows. In the case of $\beta = 0$, the frictional sliding failure criterion reduces to the maximum sliding condition described by Eq. (49). If the parameters of the model are calibrated on the results of a uniaxial tensile and compressive test with Eqs. (55) and (56), the theoretical yield loci in two dimensional PD stretch space are that of Fig. 10. However the yield criterion could be calibrated also only with the maximum uniaxial tensile strength of the material, avoiding a compressive cutoff and then adopting different values of a and β.

3. Effectiveness of micropolar MPPD and non-micropolar PDS peridynamic models in Elasticity

In this section we analyze the capabilities of the micropolar formulation against enriched bond-based peridynamic model with shear bonds (namely PDS model) in simulating the mechanical behavior of isotropic solids with arbitrary Poisson's ratio subjected to homogeneous and non-homogeneous elastic deformation fields. To this end a square lamina ($\mathrm{l} = 610$ mm, unitary thickness) subjected to three types of deformation fields and composed by 3721 particles is considered, using both PDS and MPPD models in plane stress conditions. The Young modulus is fixed to $\mathrm{E} = 70000\mathrm{MPa}$, while different values of the Poisson's ratio are used. Since we compare the peridynamic solution with elasticity solution we consider an horizon/grid spacing ratio $m = 3$ (Silling and Askari, 2005). The deformed shapes and displacement maps obtained with the two described models are compared to those obtained with Abaqus FEM analyses.[7] Firstly, two loading conditions, which sufficiently far from boundaries lead to homogeneous deformation field (simple traction and pure shear) are analyzed, then the non-homogeneous case of simple bending is investigated. The forces are applied to a boundary layer of thickness $\varrho = \delta$, resulting in the equivalent stress distributions of Fig. 11.

For the sake of brevity, Figs. 12–20 show the results obtained adopting three different values of Poisson's ratio ($\nu = -0.5, 0, 1/3$). The effective shear modulus G (in pure shear case) and Poisson's ratios (in simple traction case) are estimated numerically using the equations

$$\tau_{xy} = G\hat{\gamma} \longrightarrow G = \tau_{xy}/(2\gamma); \qquad \epsilon_{xx} = -\nu\epsilon_{yy} \longrightarrow \nu = -s_x^b/s_y^a \tag{59}$$

where the normal strains (the peridynamic stretches) are measured at points b and b' and γ is the shearing angle measured sufficiently far from boundaries, in order to obtain a more accurate measure (see Fig. 11).

These values are then related with the assigned G modulus $G = E/(2(1+\nu))$ and Poisson's ratio, thus the relative numerical errors are estimated (see Tables 1 and 2). The shearing stress τ_{xy} is calculated following the Peridynamic definition of traction vector (Lehoucq and Silling, 2008) (See Appendix A for details). In the

---

[7] In FEM analyses we considered the same discretization used for perydynamic codes, thus 61X61 four nodes squared plane-stress elements are used. The FEM mesh is imported in PD codes, and then particles positions, volumes and connections are created (see previous section).

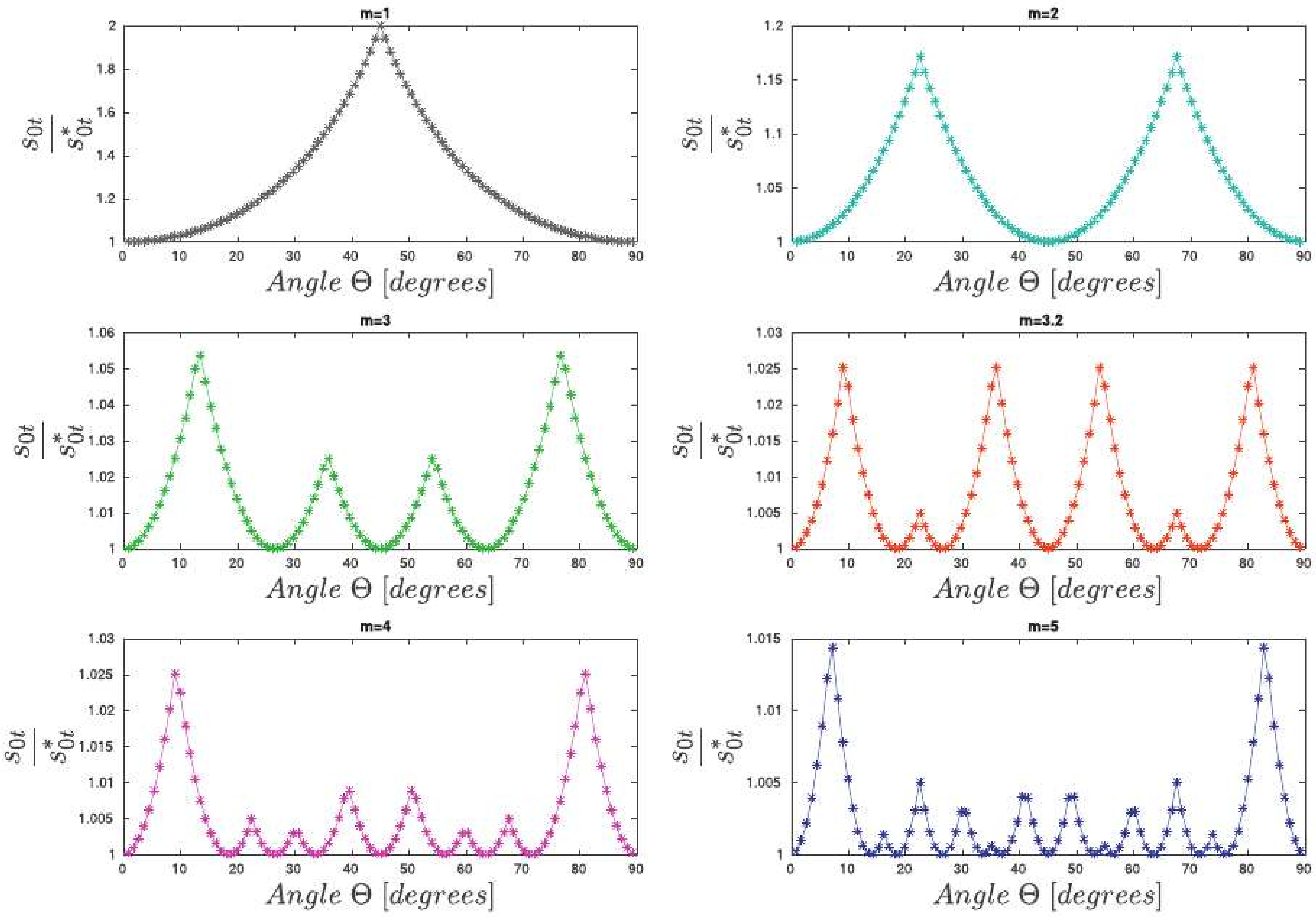

Fig. 28. Simple extension ($\nu = 0,\ s_2 = s_{0t};\ s_1 = 0$), maximum stretch yield criterion ($s_{0t} = s_2$): Influence of m on the failure anisotropy.

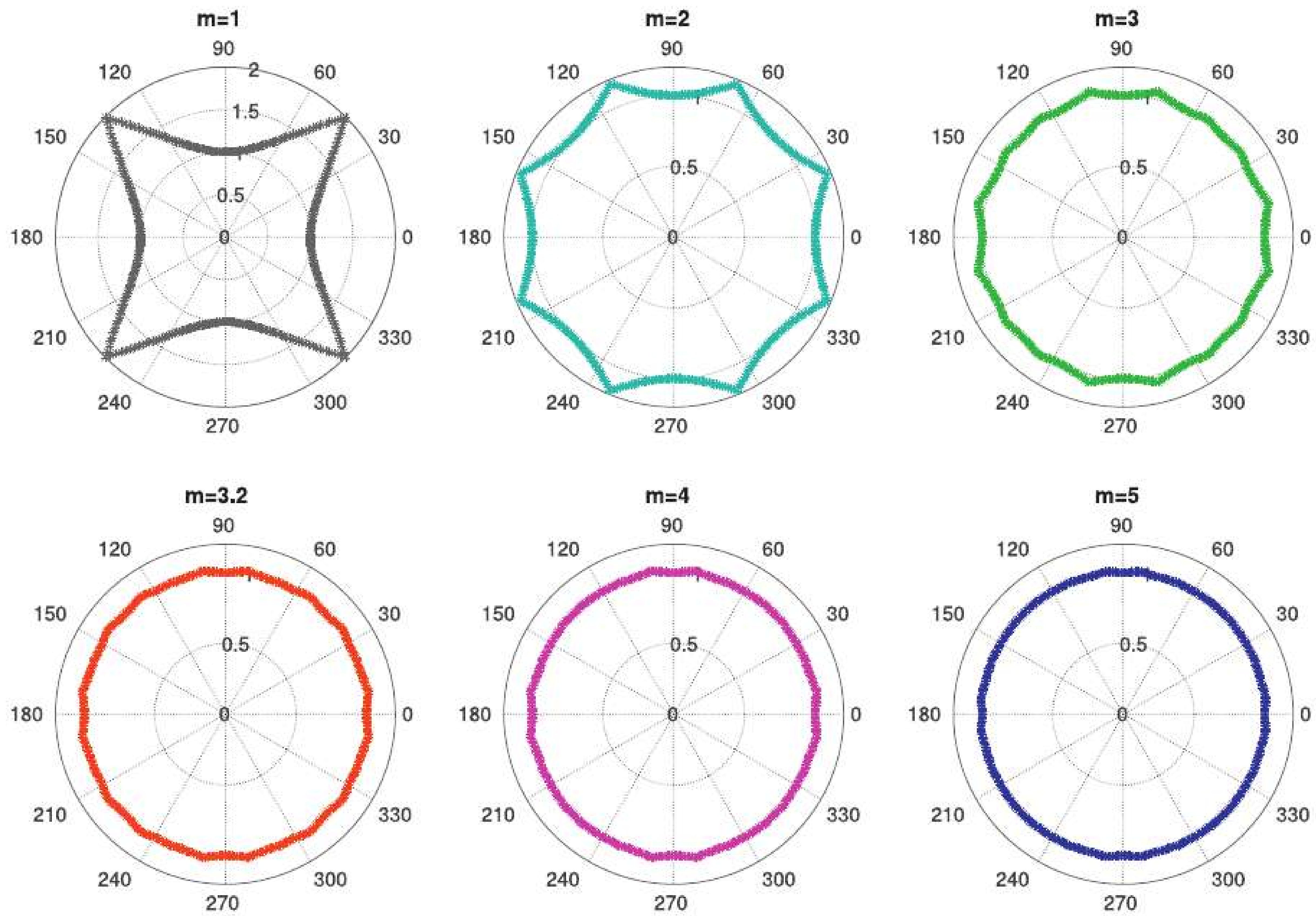

Fig. 29. Simple extension ($\nu = 0,\ s_2 = s_{0t};\ s_1 = 0$), maximum stretch yield criterion ($s_{0t} = s_2$): Influence of m on the failure anisotropy (polar coordinates; $\rho = s_{0t}/s^*_{0t},\ \Theta$).

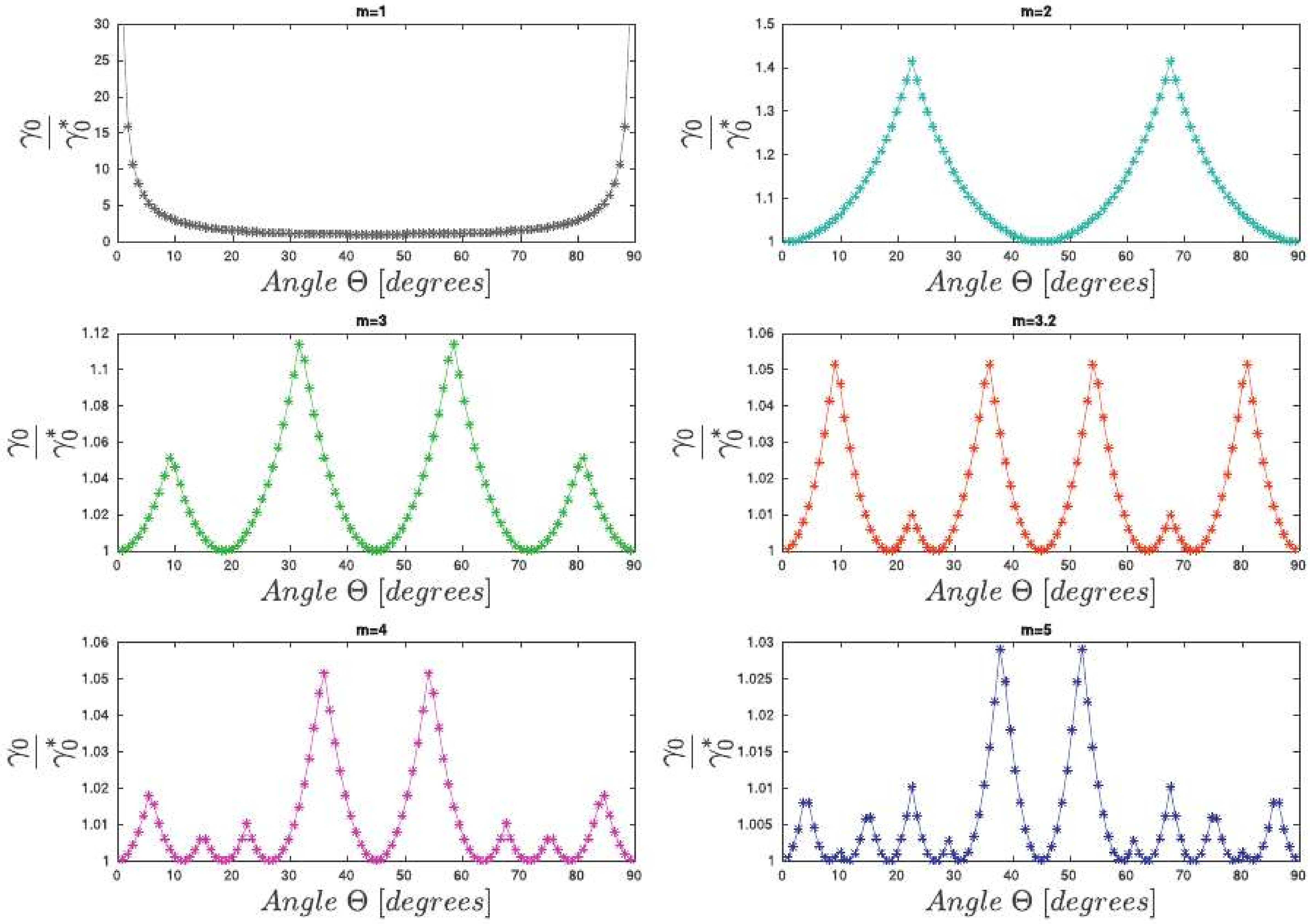

Fig. 30. Simple extension ($\nu = 0$, $s_2 = s_{0t}$; $s_1 = 0$), maximum sliding yield criterion ($\gamma_0 = s_{0t}/2$): Influence of m on the failure anisotropy.

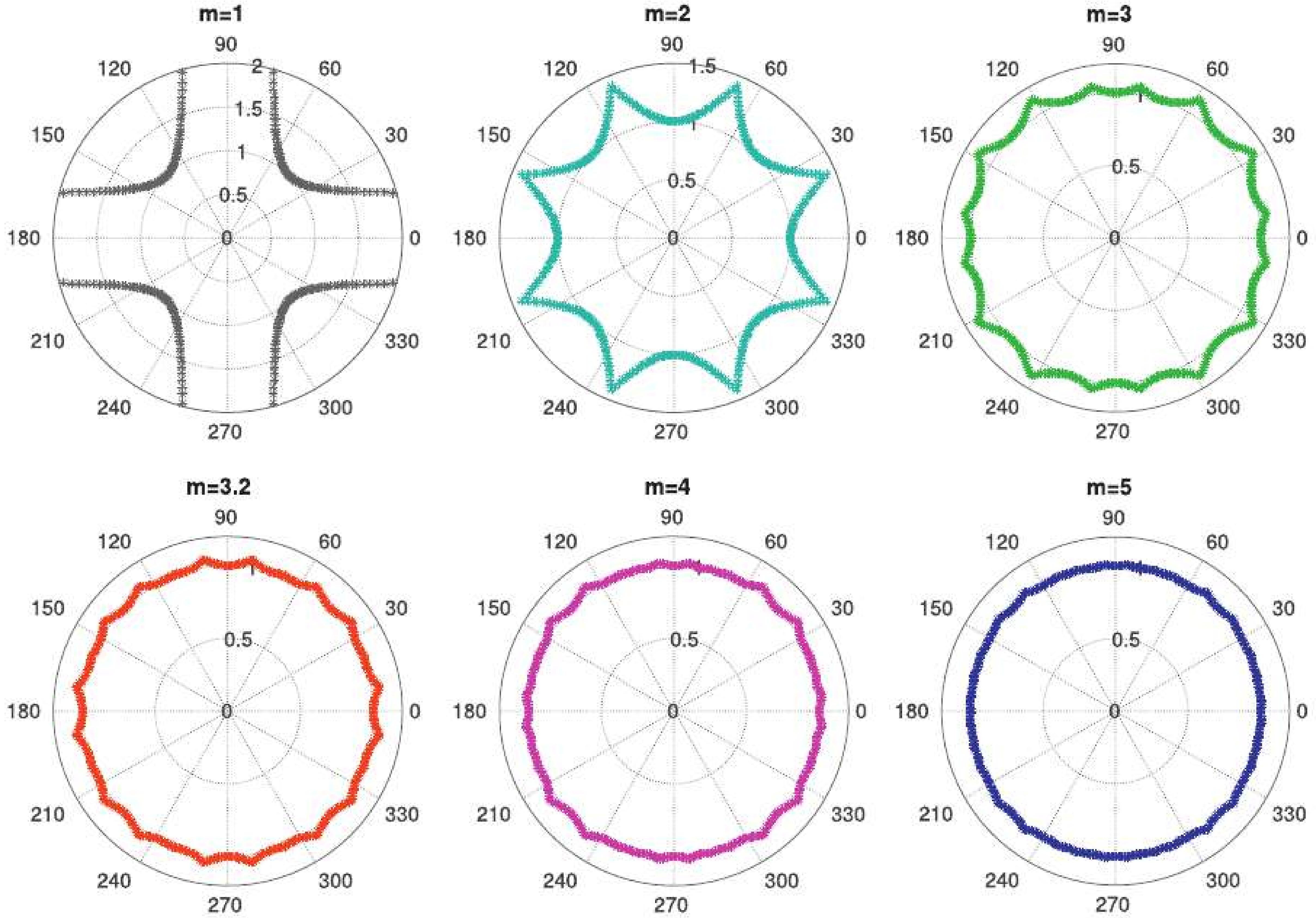

Fig. 31. Simple extension ($\nu = 0$, $s_2 = s_{0t}$; $s_1 = 0$), maximum sliding yield criterion ($\gamma_0 = s_{0t}/2$): Influence of m on the failure anisotropy (polar coordinates; $\rho = s_{0t}/s^*_{0t}$, Θ).

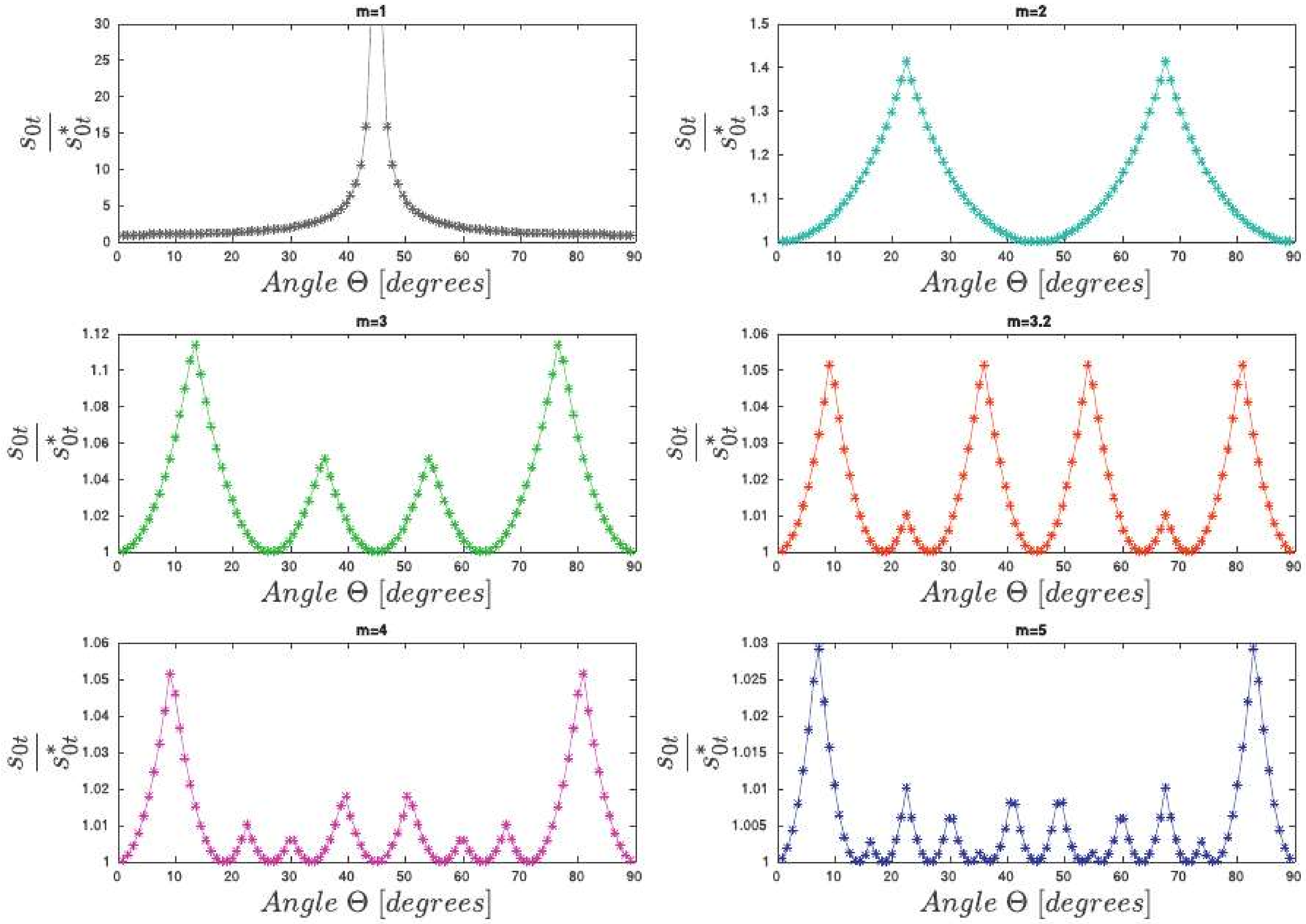

Fig. 32. Pure shear ($s_2 = -s_1 = s_{0t}$), maximum stretch yield criterion ($s_{0t} = s_2$): Influence of m on the failure anisotropy.

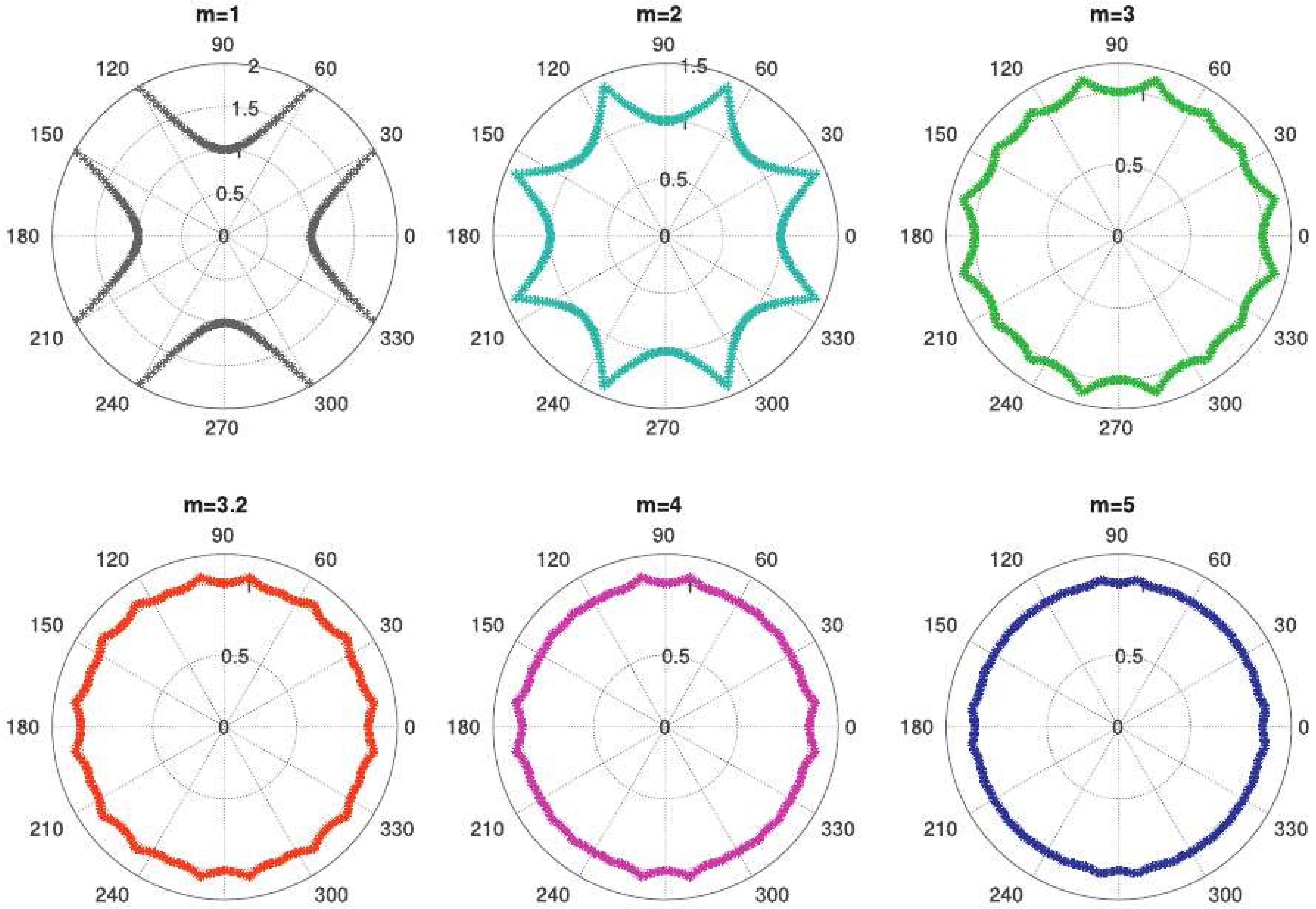

Fig. 33. Pure shear ($s_2 = -s_1 = s_{0t}$), maximum stretch yield criterion ($s_{0t} = s_2$): Influence of m on the failure anisotropy (polar coordinates; $\rho = s_{0t}/s^*_{0t}$, Θ).

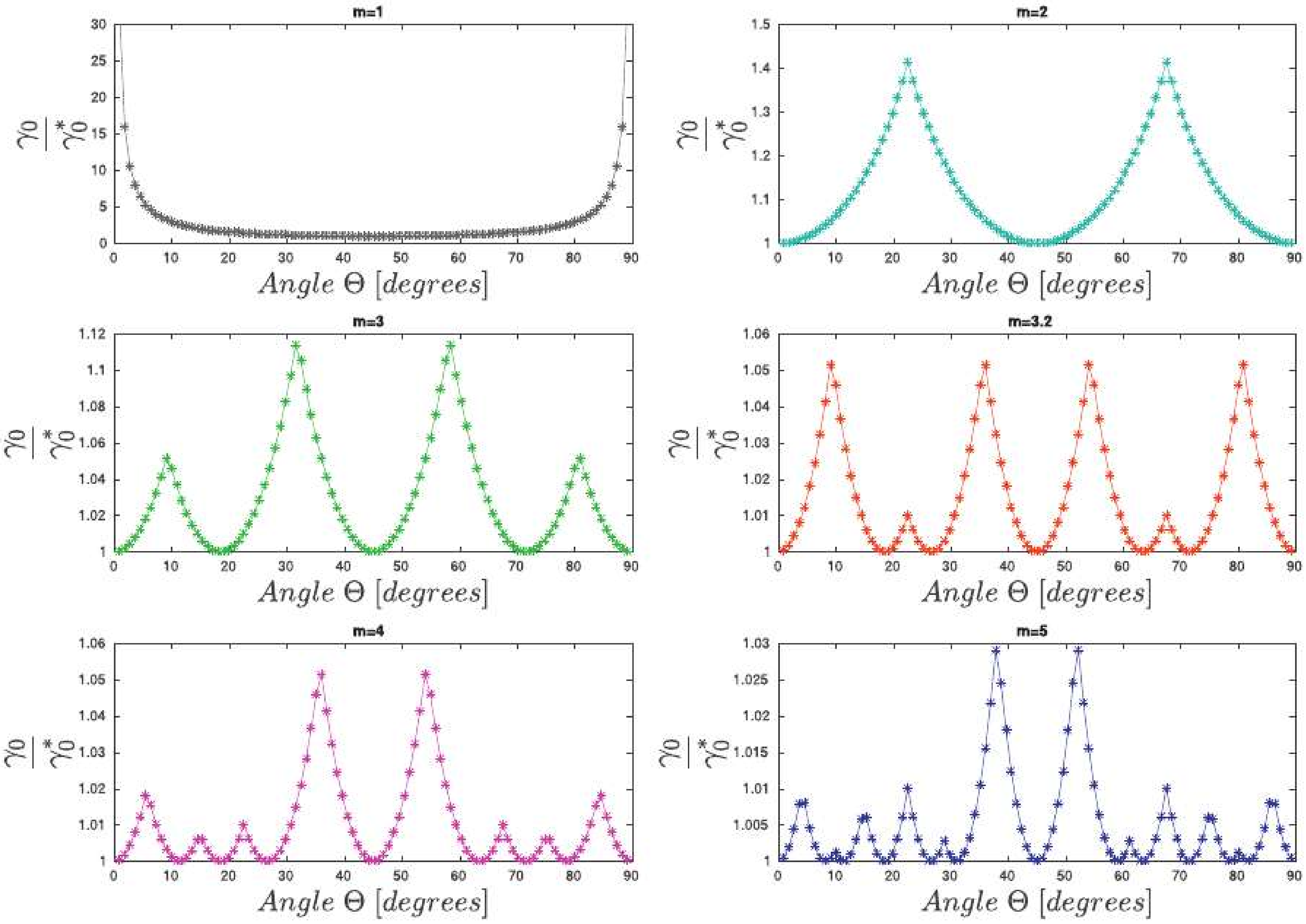

Fig. 34. Pure shear ($s_2 = -s_1 = s_{0t}/2$), maximum sliding yield criterion ($\gamma_0 = s_{0t}/2$): Influence of m on the failure anisotropy.

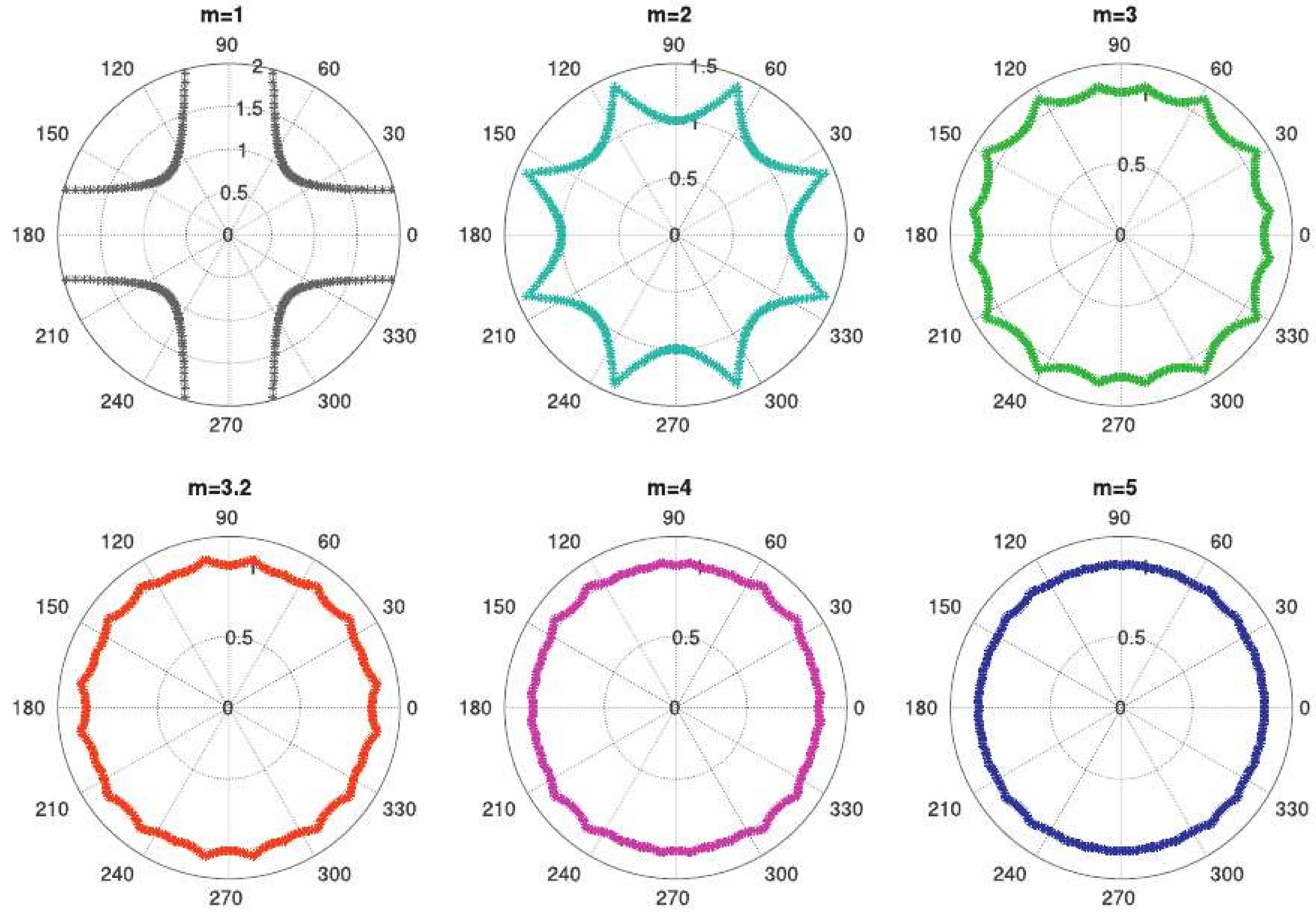

Fig. 35. Pure shear ($s_2 = -s_1 = s_{0t}/2$), maximum sliding yield criterion ($\gamma_0 = s_{0t}/2$): Influence of m on the failure anisotropy (polar coordinates; $\rho = s_{0t}/s_{0t}^*$, Θ).

Table 3
Simple bending: numerical errors and absolute maximum displacements (mm) obtained with FE, PDS and MPPD models.

ν	u_x (FEM)	u_x (PDS)	u_y (MPPD)	u_y (FEM)	u_y (PDS)	u_y (MPPD)	Er.$_{PDS}$	Er.$_{MPPD}$
−0.5	0.04360	0.01432	0.04565	0.02156	0.00587	0.02223	200.4	4.2
0	0.04281	0.02193	0.04474	0.02177	0.00000	0.02250	98	4.3
0.1	0.04264	0.02302	0.04372	0.02356	0.00244	0.02383	85	2.5
0.25	0.04238	0.02807	0.04203	0.02628	0.00966	0.02589	51	1.6
1/3	0.04224	0.04283	0.04283	0.02779	0.02802	0.02802	2.1	2.1

Table 4
Natural frequency analysis: synopsis of the of frequency values (Hz) and relative errors (%) corresponding to the I flexural natural mode calculated by FE, PDS and MPPD models.

ν	f_I (FEM)	f_I (PDS)	f_I (MPPD)	Er.$_{PDS}$	Er.$_{MPPD}$
−0.5	1195.0	3661.5	1174.5	206.4	1.7
0	1047.2	2294.9	1026.1	119.4	2.0
0.1	1027.9	2025.5	1008.9	97.1	1.8
0.25	1002.5	1565.9	990.7	56.2	1.2
1/3	989.89	982.2	982.2	2.1	2.1

Table 5
Natural frequency analysis: synopsis of the of frequency values (Hz) and relative errors (%) corresponding to the I axial natural mode calculated by FE, PDS and MPPD models.

ν	f_{II} (FEM)	f_{II} (PDS)	f_{II} (MPPD)	Er.$_{PDS}$	Er.$_{MPPD}$
−0.5	2400.2	2475.9	2308.9	3.2	3.8
0	2320.0	2294.9	2262.2	1.1	2.4
0.1	2322.6	2300.6	2275.3	1.0	1.9
0.25	2330.4	2315.8	2317.7	0.6	0.5
1/3	2336.3	2311.8	2311.8	2.1	2.1

Table 6
Natural frequency analysis: synopsis of the of frequency values (Hz) and relative errors (%) corresponding to the II flexural natural mode calculated by FE, PDS and MPPD models.

ν	f_{III} (FEM)	f_{III} (PDS)	f_{III} (MPPD)	Er.$_{PDS}$	Er.$_{MPPD}$
−0.5	3245.3	5770.3	3312.1	77.8	2.1
0	2771.2	4978.3	2770.7	79.8	0.1
0.1	2712.0	4562.4	2702.3	68.2	2.5
0.25	2635.9	3649.5	2627.8	38.4	1.6
1/3	2590.0	2594.7	2594.7	2.1	2.1

case of simple traction and pure shear, the non-polar model and the micropolar model give nearly identical results because under homogeneous deformation fields, the rotational degrees of freedom are not activated. Moreover displacement maps obtained with both PDS and MPPD models are in perfect agreement with FEM solution. We can notice only some small differences between FEM-MPPD and PDS near the boundaries of the square plate, where the forces are applied and thus the deformation field results to be non-homogeneous, however the Poisson's ratios and shearing modulus G, estimated numerically are affected by errors which are less than 4%. Thus the non-micropolar model seems to predict well the mechanical behavior of elastic materials in such conditions, leading to a correct description of the Poisson's ratio influence on the elastic solution. This notwithstanding, in the case of simple bending (see Figs. 18–20 and Table 3), contrarily to any MPPD model, the enriched PD formulation with shear bonds (i.e. PDS model) does not seem to approximate well the FEM solution if the Poisson's ratio is different from 1/3 (central force model). This because the model does not take into account particle's rotational degree of freedom, which in a lattice model are activated for non-homogeneous deformation field involving local rotations. Horizontal displacements maps calculated with PDS are slightly and only qualitatively similar to that of FEM-MPPD, whereas the vertical displacements are completely different both in trend and in values. This can be explained considering that in the case of simple bending

$$\epsilon_{xx} = s_x = -\nu \frac{M}{EJ} y; \quad \epsilon_{yy} = s_y = \frac{M}{EJ} y \tag{60}$$

where M is the bending moment and J is the second moment of inertia of the square plate section. The nonzero components of the deformation depends on coordinate y, thus the deformation field is (vertically) non-homogeneous.

Moreover each family H_x (a particle with all the neighboring ones inside the horizon) is subjected to a deformation field that can be decomposed in a symmetric and antisymmetric part, so that

$$\frac{1}{2}(\mathbf{H} - \mathbf{H}^T) = \frac{1}{2}[(\mathbf{F} - \mathbf{I}) - (\mathbf{F} - \mathbf{I})^T] \neq \mathbf{0} \tag{61}$$

where **H** is the displacement gradient tensor and **F** is the deformation gradient tensor.

When shearing bond stiffness of the lattice is not null, as in the case of $\nu \neq 1/3$, this aspect leads to incorrect results, since the rotational invariance of the lattice unit cell may not be preserved (Pan et al., 2018). The main reason, according to Jagota and Scherer (1993), is that shear springs cannot distinguish the differences in the tangential displacement of two particles owing to a common rotation or shear. Thus, a global rigid body rotation may incorrectly result in an additional strain energy inside the shear springs (Nikolić et al., 2017; Cusatis et al., 2003). As a result, the deformed configurations of the plate predicted by non-micropolar model do not appear accurate, while that obtained with MPPD is in good agreement with FEM solution see also Fig. 21.

These results give a general interpretation of that obtained by Schlangen and Garboczi (1997) and Chang et al. (2002), in which is shown that under mode-I loading conditions, both micropolar and non-micropolar lattice models predict correct crack patterns, while noticeable differences appear in the results under mode-II loading conditions (i.e. shear box test). They state that when normal and shearing bond forces are used the crack starts at the correct angle, but after that the crack stays straight and does not curve, whereas in the simulations with micropolar model, the crack pattern is much closer to the experiments (Schlangen and Garboczi, 1996).

3.1. Natural frequency analysis

A modal analysis is performed in order to evaluate the natural frequencies and the corresponding modal shapes of a square lamina with fixed base, by using both micropolar MPPD and non-micropolar PDS peridynamic models. The lamina is now composed by 3600 particles (square grid of 60 × 60 particles), adopting as usual, a grid spacing $\Delta x = 10$mm and $m = 3$. The density $\rho = 2500 \text{Kg/m}^3$. Young modulus $E = 70000$MPa , whereas five different values of the Poisson's ratio are considered, as in the static analyses.

The generalized dynamic equilibrium of a bond-based PD model[8] can be formulated by expressing the equilibrium of the effective forces associated with each of its degrees of freedom. Then, without considering any damping, a multi degrees of freedom equilibrium equation is obtained collecting bond DOFs in the vector

$$[M]_{bond}\{\ddot{u}\} + [K]_{bond}\{u\} = \{p\} \tag{62}$$

where $[M]_{bond}$ is the bond mass matrix, $[K]_{bond}$ is the bond stiffness matrix and $\{p\}$ is the vector of external loads (Baraldi et al., 2016). The model is meshfree and Lagrangian thus the inertial properties of the lattice are concentrated in the particles centroyds and zero mass is associated to the ligaments. Each particle i is assumed having mass $M_i = \Delta V_i \cdot \rho$ and moment of inertia $J_i = M_i r_i^2$ (in the case of MPPD model), being r_i the radius of gyration associated to the particle, which in general is $r_i = 1/12(\Delta x^2 + \Delta y^2)$ (Bacigalupo and Gambarotta, 2017).

The local mass matrix $[M]_{bond}$ may be highlighted by writing the kinetic energy of each particle in discrete form

$$\Pi(\dot{u}_x, \dot{u}_y) = \frac{1}{2}M\dot{u}_x^{\,2} + \frac{1}{2}M\dot{u}_y^{\,2} \tag{63}$$

$$\Pi(\dot{u}_x, \dot{u}_y, \dot{\theta}) = \frac{1}{2}M\dot{u}_x^{\,2} + \frac{1}{2}M\dot{u}_y^{\,2} + \frac{1}{2}J\dot{\theta}^2 \tag{64}$$

for PDS and MPPD models respectively.

The $[M]_{bond}$ matrix in the case of non-micropolar model is then

$$[M]_{bond} = \begin{bmatrix} \rho\Delta V_i & 0 & 0 & 0 \\ 0 & \rho\Delta V_i & 0 & 0 \\ 0 & 0 & \rho\Delta V_j & 0 \\ 0 & 0 & 0 & \rho\Delta V_j \end{bmatrix} \tag{65}$$

whereas in the case of micropolar model we obtain

$$[M]_{bond} = \begin{bmatrix} \rho\Delta V_i & 0 & 0 & 0 & 0 & 0 \\ 0 & \rho\Delta V_i & 0 & 0 & 0 & 0 \\ 0 & 0 & \rho r_i^2\Delta V_i & 0 & 0 & 0 \\ 0 & 0 & 0 & \rho\Delta V_j & 0 & 0 \\ 0 & 0 & 0 & 0 & \rho\Delta V_j & 0 \\ 0 & 0 & 0 & 0 & 0 & \rho r_j^2\Delta V_j \end{bmatrix} \tag{66}$$

Omitting the applied external load vector $\{p\}$ in Eq. (62), and assuming that the free vibration motion of the bond is simple harmonic, a standard eigenvalue problem is obtained

$$[K]_{bond}\{u\} - \omega^2[M]_{bond}\{u\} = \{0\} \tag{67}$$

where ω are the eigenvalues of the problems, related to the natural frequencies f by $\omega = 2\pi f$. Assembling the global matrices of the square lamina, the first three modal shapes are obtained (see Tables 4–6 and Figs. 22–24). The natural shapes of the plate predicted by non-micropolar model (in the case of Poisson's ratio $\neq 1/3$, i.e. central force model) do not appear accurate, while those obtained with the conceived micropolar peridynamic formulation are in perfect agreement with FEM solutions. Moreover the errors relative to the FEM solutions seems to be not affected by the Poisson's ratio value in the case of micropolar model.

It can be noted that negative values of Poisson's ratio lead the axial natural mode calculated with PDS model to be the principal natural mode, thus characterized by a frequency lower than that corresponding to the first flexural mode. Moreover in the case of $\nu = 0$ those natural modes have almost the same value of frequency. This can be explained considering that for PDS model $g > c$ if $\nu < 0$ and $g = c$ if $\nu = 0$, thus a lower global stiffness is associated to axial deformation fields with respect to those which involves bond slidings.

4. Failure response and effective initial yield domains

The specific spatial discretization adopted for full-discrete models leads the model to be intrinsically anisotropic regarding the failure response (Tancogne-Dejean and Mohr, 2018; Schlangen and van Mier, 1992). In Peridynamics, if we apply for example a uniform PD stretch field s along different directions with respect to the direction of the grid and we evaluate the relative elongation of the bond as a function of this angle of rotation ζ, we obtain that the values at which the springs reach the elastic limit are the exact given limit values s_{t0} only for those directions aligned with the bonds connecting the particles i and j. This grid effect (i.e. the anisotropic behavior at yield of the lattice) leads to simulated crack patterns dependent on the particle packing scheme and, depending on the spatial orientation angle of a regular grid of particles, different peak load values and different crack patterns arise under the same loading conditions. This notwithstanding, the non-local nature of peridynamics leads the above mentioned mesh-depencency of the results, typical of lattice and discrete models, to be weakened or completely eliminated at the cost of a higher computational expense (Pan et al., 2018).

In this section the anisotropy of the failure conditions, or in other words, the direction dependency of the failure response, corresponding to the three yield criteria described in the previous section is investigated. Considering six values of $m = \delta/\Delta x$, a parameter which controls the range of non-local actions (see Fig. 25), a simple extension and a pure shear deformation states are imposed to the family H_x of the particles i (i.e. the fundamental unit cell of a peridynamic model). A deformation state can be described by

$$[\mathbf{F}] = \begin{bmatrix} 1+s_1 & 0 \\ 0 & 1+s_2 \end{bmatrix} \tag{68}$$

where s_1 and s_2 represent the orthogonal peridynamic stretch components considered. In the case of simple extension $s_2 = -\nu s_1$ while in pure shear conditions we have $s_1 = -s_2$. Each deformation state considered is rotated of a series of angles in the interval $-\pi/2 \geq \Theta \geq 0$, thus

$$[F]^* = [Q][F][Q]^T \tag{69}$$

where $[Q]$ operates the rotation of angle Θ

$$[Q] = \begin{bmatrix} \cos\Theta & \sin\Theta \\ -\sin\Theta & \cos\Theta \end{bmatrix} \tag{70}$$

so that one hundred different orientations are obtained (see Fig. 26). The influence of m on this phenomenon, in the case of a uniform grid of discrete peridynamic particles, is calculated analytically dividing for each orientation Θ, the expected maximum value of the deformation parameter related to the failure criterion under consideration (i.e. the analytical values s_{0t} or γ_0) by the maximum measured value of such parameter (s_{0t}^* or γ_0^*). For simplicity we consider first the case of $\nu = 0$ with the maximum stretch and maximum sliding criteria, for which Eqs. (44) and (49) lead to $\gamma_0 = s_{0t}/2$. In the case of simple extension, setting $s_2 = s_{0t}$ in Eq. (68), the failure condition with both yield criteria is reached, whereas in the case of pure shear, adopting $s_2 = s_{0t}/2$, only the failure condition in maximum sliding criterion is obtained, because the maximum stretch in such condition is $s_{0t}/2$. Thus, in order to obtain the yield conditions with the maximum stretch criterion and thus make the presented results comparable, another pure shear state, this time with $s_2 = s_{0t}$ is studied (Fig. 27).

---

[8] As explained in previous sections the model is conceptually comparable to MPPD with rotational degrees of freedom restrained.

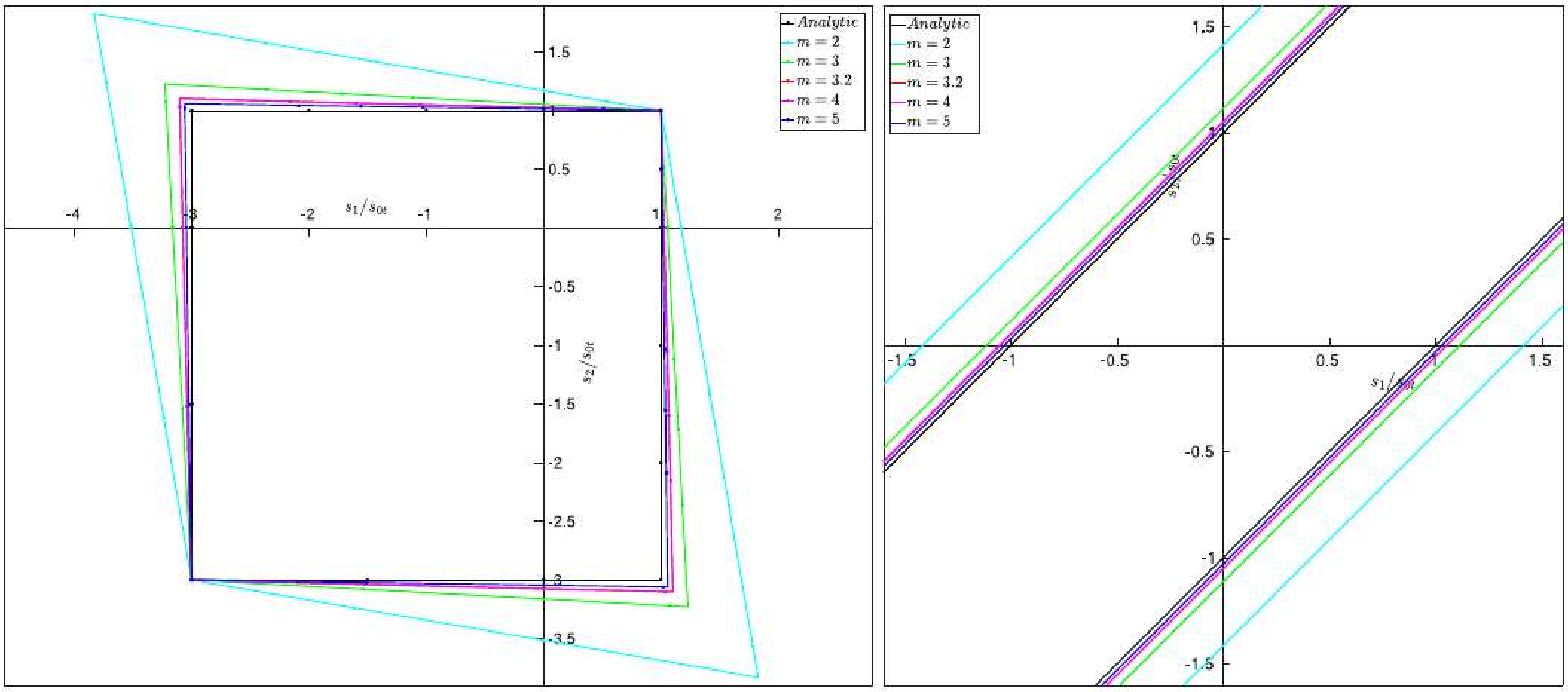

Fig. 36. Maximum stretch yield criterion (sx) and maximum sliding yield criterion (dx, considering $\nu = 0$): Effective yield loci envelopes in two dimensional principal strain (PD stretch) space corresponding to the most unfavorable conditions, being the most favorable condition, instead, represented by the theoretical (Analytic) yield loci.

Increasing the range of non-local actions, i.e. increasing m in a regular fixed grid of particles, the anisotropy effect is reduced since an internal length is introduced in the model. It is the same if in the case of a fixed horizon size δ (related for example to a measured quantity obtained from experiments) we increase the particles density within the horizon, thus reducing the grid spacing Δx of the discretization. A good compromise between the accuracy of the solution and the computational effort is to set $m = 3$ or $m = 3.2$.

This latter represent probably the best choice with both the maximum stretch and maximum shear deformation yield criteria, in fact, although it has only eight particles more than the $m = 3$ unit-cell configuration, it is characterized by a maximum error equal to that corresponding to $m = 4$ (see Figs. 28–35). It can be noted that whatever is the value of the range of non-local actions, the intrinsic anisotropy (both in shape and in values) of the bond shearing yield is independent on the specific load path considered (see Figs. 30, 31, 34 and 35). On the contrary, the direction dependency of the failure response corresponding to the maximum stretch yield criterion is influenced by the specific load path considered (see Figs. 28, 29, 32 and 33). In fact, even if the shape of the failure anisotropy polar diagrams is the same (see Figs. 29 and 33), they are characterized by different maximum values.

The analysis of other thirty different loading conditions (corresponding to homogeneous deformation fields on the PD unit cell) adopting the maximum stretch, maximum shear deformation (sliding) and the frictional sliding criteria leads to a deeper understanding of this phenomenon. For each deformation state of the unit cell, the estimated deformation parameters at failure related to the three failure criteria considered and affected by the maximum errors (i.e. the effective values corresponding to that orientation Θ of the deformation state for which the error is maximum), are reported together with the theoretical expected values of such parameters. The effect of the direction dependency of the failure response on the modification of the theoretical first yield domains is thus quantified, considering different $m = \delta/\Delta x$ ratios. In fact, we identified the effective yield loci envelopes in two dimensional principal strain (PD stretch) space corresponding to the most unfavorable conditions (see Figs. 36 and 38 and Tables 7 and 8), being the most favorable condition, instead, represented by the theoretical (Analytic) yield loci. The increase of the range of non-local actions drastically reduces the anisotropic yield effect, and this is true for all the failure criteria considered herein.[9] In fact Figs. 36 and 37 show that the more m increases, the more the maximum error yield domain results closer to the analytical one.

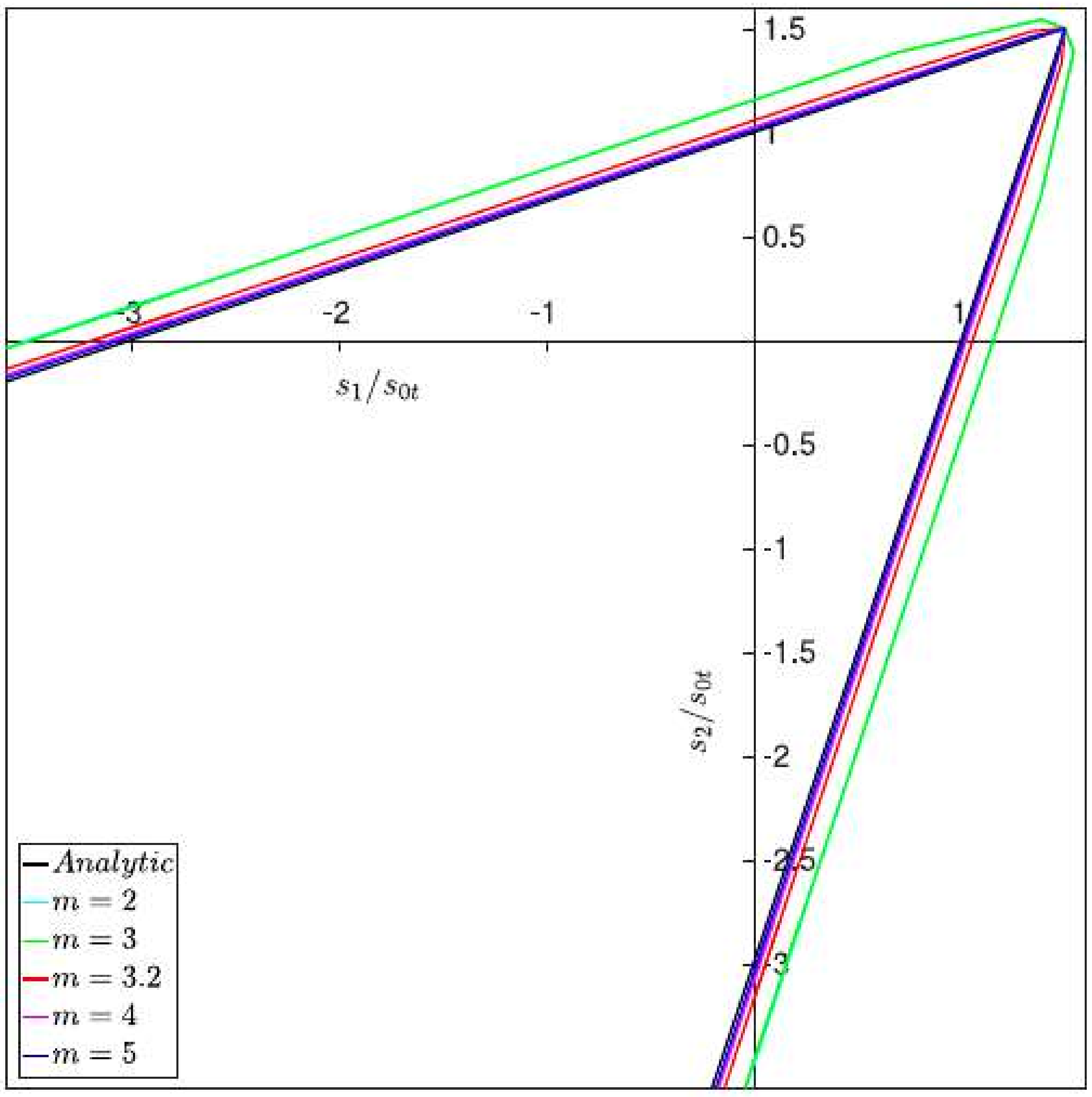

Fig. 37. Frictional sliding yield criterion (considering $\nu = 0$) First Yield domains in 2D principal PD stretch space and relative maximum errors. Effective yield loci envelopes in two dimensional principal strain (PD stretch) space corresponding to the most unfavorable conditions, being the most favorable condition, instead, represented by the theoretical (Analytic) yield loci.

---

[9] Fig. 38 represents the maximum error envelopes corresponding to a sliding criterion combined with a stretch criterion (assuming $s_{0c} = -s_{0t}$) and to a frictional sliding criterion combined with a stretch criterion (assuming $s_{0c} = -3s_{0t}$), respectively. In fact, a yield condition on the stretch measure is required in any case, for the majority of the applications.

Table 7
Maximum stretch yield criterion: maximum errors corresponding to some significant load paths, adopting five different values of m.

s_1/s_{0t}	s_2/s_{0t}	$e_{\max}(\%)$, $m=2$	$e_{\max}(\%)$, $m=3$	$e_{\max}(\%)$, $m=3.2$	$e_{\max}(\%)$, $m=4$	$e_{\max}(\%)$, $m=5$
1	1	0.00	0.00	0.00	0.00	0.00
0.5	1	7.90	2.62	1.24	1.24	0.71
0	1	17.16	5.39	2.51	2.51	1.44
−1	1	41.42	11.38	5.15	5.15	2.92
−2	1	78.36	18.11	7.92	7.92	4.44
−3	1	24.26	7.31	3.37	3.37	1.93
−3	0	17.16	5.39	2.51	2.51	1.44
−3	−1.5	7.90	2.62	1.24	1.24	0.71
−3	−3	0.00	0.00	0.00	0.00	0.00

Table 8
Maximum sliding yield criterion: Maximum errors corresponding to some significant load paths, adopting five different values of m.

s_1/s_{0t}	s_2/s_{0t}	$e_{\max}(\%)$, $m=2$	$e_{\max}(\%)$, $m=3$	$e_{\max}(\%)$, $m=3.2$	$e_{\max}(\%)$, $m=4$	$e_{\max}(\%)$, $m=5$
0.5	1	41.48	11.46	5.23	5.23	3.00
0	1	41.48	11.46	5.23	5.23	3.00
−0.33	0.66	41.48	11.46	5.23	5.23	3.00
−0.5	0.5	41.48	11.46	5.23	5.23	3.00
−0.66	0.33	41.48	11.46	5.23	5.23	3.00
−1	0	41.48	11.46	5.23	5.23	3.00
−1	−0.5	41.48	11.46	5.23	5.23	3.00

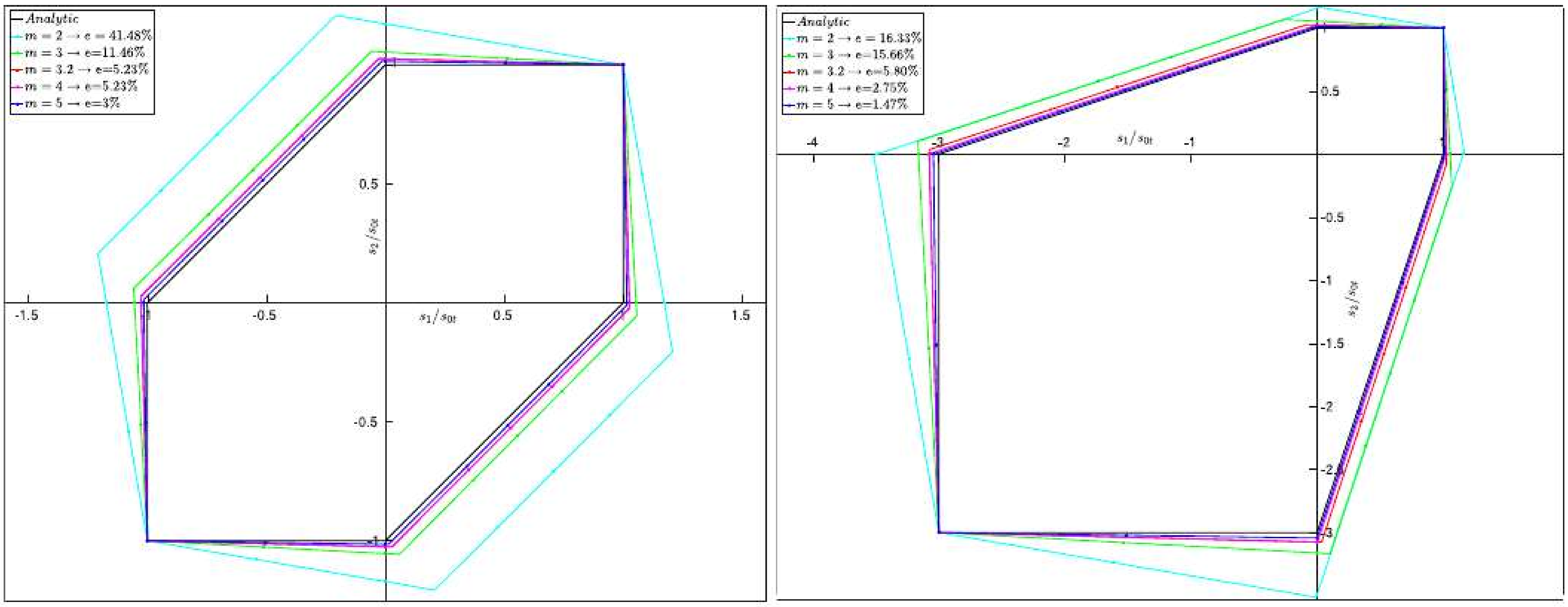

Fig. 38. Maximum sliding (sx) and frictional sliding (dx) yield criteria (considering $\nu = 0$) combined with a maximum stretch criterion: Effective yield loci envelopes in two dimensional principal strain (PD stretch) space corresponding to the most unfavorable conditions, being the most favorable condition, instead, represented by the theoretical (Analytic) yield loci.

We can conclude that in the case of maximum stretch criterion, the theoretical yield loci is independent of the value of Poisson's ratio adopted (see Section 1), however the intrinsic anisotropy of the yield condition is a linear function of the deviatoric part of the deformation tensor (at failure) to which the specific unit cell is subjected to. Thus it depends on the specific load path considered (See Table 7 and Fig. 36). In particular, we observed an increase of such anisotropic effect as the deviatoric part of the deformation tensor increases, even if the shape of the relative polar diagram does not change. In the case of a maximum sliding criterion, instead, the theoretical yield loci depends on the specific value of the Poisson's ratio considered, whereas the direction dependency of the failure response is not influenced by the load path, nor in trends, nor in maximum values (See Table 8 and Figs. 36, 38). For sake of brevity, figures shows only the yield loci envelope in the case of $\nu = 0$, however these considerations are general and thus referable also to the case of other different values of ν.

This because the theoretical yield conditions corresponding to the maximum sliding criterion are represented by parallel lines whose distance from the origin is dependent on the specific value of the Poisson's ratio. A frictional sliding failure criterion exhibits both the aforementioned behaviors. In fact the analytical yield loci depends on the value of Poisson's ratio and the anisotropic effect shows a slight dependence on the load path considered, as Figs. 37 and 38 shows. This is reasonable because the frictional sliding condition is influenced by both the anisotropic effect in bond stretch and sliding measures. In particular there is an increase of the anisotropic effect with the increase of the deviatoric character of the deformation field, however this effect is not significant as in the case of maximum stretch criterion, because of the stabilizing effect induced by the bond sliding measure (see Table 9).

Moreover, the errors drop to zero in proximity of the vertex of the theoretical yield loci because the more the deformation field

Table 9
Frictional sliding yield criterion: maximum errors corresponding to some significant load paths, adopting five different values of m.

s_1/s_{0t}	s_2/s_{0t}	$e_{\max}(\%),\ m=2$	$e_{\max}(\%),\ m=3$	$e_{\max}(\%),\ m=3.2$	$e_{\max}(\%),\ m=4$	$e_{\max}(\%),\ m=5$
1.5	1.5	0.00	0.00	0.00	0.00	0.00
0.6	1.2	15.50	15.48	5.58	2.36	1.10
0	1	15.57	15.50	5.61	2.41	1.15
−1	0.66	15.74	15.57	5.69	2.54	1.28
−1.5	0.5	15.85	15.61	5.74	2.64	1.36
−2	0.33	15.90	15.66	5.80	2.75	1.47
−3	0	16.33	15.78	5.96	3.02	1.72

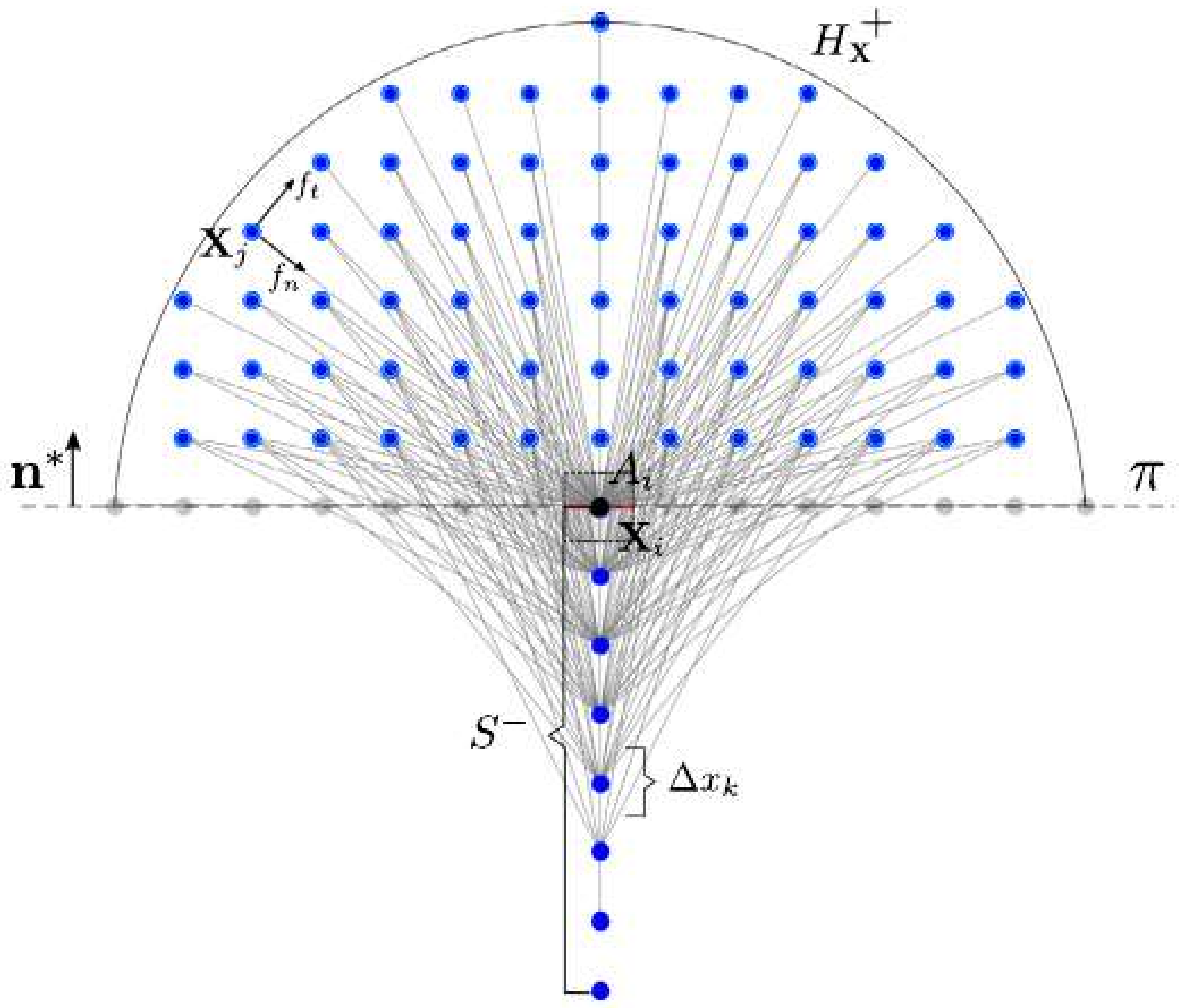

Fig. A.39. Definition of the PD traction vector at point $\mathbf{X_i}$ according to Eq. (A.4) with respect to plane π of outward pointing unit normal $\mathbf{n}^*$.

is spherical, the more the yield is controlled by the bond stretch measure.

5. Conclusions

In this paper a generalized micropolar bond-based Peridynamic is proposed. The conceived model is based on the definition of a microelastic energy function which depends on three deformation parameters: the bond stretch, the bond shear deformation accounting for the rotational degree of freedom, and the particles relative rotation. Hence three different stiffness parameters for each peridynamic bond are defined and calibrated separately, leading to a more general micropolar model applicable to a wide variety of mechanical problems. Results of a natural frequency study and of static analyses considering simple loading cases showed that the definition of a microelastic energy function dependent on a shear deformation measure, leads to a model which results not capable to describe properly the mechanical behavior of Poisson's solids subjected to non-homogeneous deformation fields, if rotational degrees of freedom of the particles are not considered (as in PDS model), because the rotational invariance is not preserved. Moreover two novel deformation-based failure criteria based on the definition of a bond shearing deformation limit are proposed. The theoretical first yield domain corresponding to the classical maximum stretch criterion and to the maximum shear deformation and frictional sliding criteria presented in this work are derived and then a deep investigation on the effective failure response of the PD lattice model is carried out. The effect of the direction dependency of the failure response on the modification of the theoretical first yield domains is shown, considering different range of non-local actions. In the case of maximum stretch criterion, the theoretical yield loci is independent on the value of Poisson's ratio adopted, however the intrinsic anisotropy of the yield condition is a linear function of the deviatoric part of the deformation tensor (at failure) to which the specific unit cell is subjected to. Thus it depends on the specific load path considered. Considering instead a maximum sliding criterion, we noted that the theoretical yield loci depends on the specific value of the Poisson's ratio considered, whereas the anisotropy of the failure condition is not influenced by the load path, nor in trends, nor in maximum values. Finally, being influenced by both the deformation mechanisms, the frictional sliding failure criterion exhibits both the aforementioned behaviors. In fact the analytical yield loci depends on the value of Poisson's ratio and the anisotropic effect shows a slight dependence on the load path considered. Results presented in this work provide new insight into understanding the mechanical behavior of the local and non-local lattices, and even if obtained considering a specific Peridynamic model, they can be considered quite general and referable to other types of lattices structures and discrete models.

Appendix A. Stress computation in bond-based Peridynamic models

According to a physically-based interpretation of stress similar to that given by Cauchy (Capecchi and Ruta, 2015; Cauchy, 1828) in the early discussions on elasticity,[10] and adapting this concept to peridynamics, the PD traction vector with respect to plane π and with outward pointing unit normal $\mathbf{n}^*$ at point $\mathbf{X}$ can be obtained by computing all the interactions between particles arranged on a line normal to the area of interest and particles beneath this surface. This concept can be expressed in integral form as

$$\mathbf{t}(\mathbf{X}, \mathbf{n}^*) = \int_{L_s} \int_{H_{\mathbf{X}}^{+}} \mathbf{f}(\mathbf{u}' - \widehat{\mathbf{u}}, \mathbf{X}' - \widehat{\mathbf{X}}) dV_{\mathbf{X}'} ds \tag{A.1}$$

where $H_{\mathbf{X}}^{+}$ is the positive part of the horizon region $H_{\mathbf{X}}$ (i.e. the family of $\mathbf{X}$) and L_s is the set of collinear points (characterized by a maximum distance δ from $\mathbf{X}$) in the opposite direction of $\mathbf{n}^*$ such that

$$L_s = \{\widehat{\mathbf{X}} \in H_{\mathbf{X}}^{-} : (\widehat{\mathbf{X}} = \mathbf{X} - s\mathbf{n}^*),\ 0 \le s < \delta\} \tag{A.2}$$

being

$$H_{\mathbf{X}}^{-} = \{\mathbf{X}' \in \beta : (\mathbf{X}' - \mathbf{X}) \cdot \mathbf{n}^* < 0\} \tag{A.3}$$

---

[10] Adapted from Capecchi and Ruta (2015): Let us consider a plane π of unit normal $\mathbf{n}^*$ through a point $\mathbf{X}$, dividing the body into two parts, which we will suppose horizontal [...]. Let us denote by β^+ the upper part and β^- the lower part, in which we will include the material points belonging to the plane itself. Consider a cylinder B, having an infinitesimal base dA on the plane π and containing $\mathbf{X}$, located in the half space β^-, the height of which is at least the same as the radius of molecular activity. The force of the molecules of β^+ over those of B, divided by dA, will be the *pressure* exerted by β^+ over β^-, with respect to the unity of surface and relative to the point $\mathbf{X}$.

Eq. (A.1) represents the original definition of the peridynamic traction vector given by Silling (2000) in the context of homogeneous deformations. To this end a specific subroutine which reads the displacement values as input and computes the peridynamic traction at **X** summing up the forces which satisfy the definition previously given, has been implemented Ballarini et al. (2018).

The formal discretized equation of the peridynamic traction vector in the case of regular grid of particles can be written as

$$\begin{aligned}\mathbf{t}(\mathbf{X}_i,\mathbf{n}^*) &= \sum_{k=1}^{S^-}\sum_{j=1}^{H+}\mathbf{f}(\mathbf{u}_j-\mathbf{u}_k,\mathbf{X}_j-\mathbf{X}_k)\Delta V_j\Delta x_k\\ &= \frac{1}{A_i}\sum_{k=1}^{S^-}\sum_{j=1}^{H+}\mathbf{f}(\mathbf{u}_j-\mathbf{u}_k,\mathbf{X}_j-\mathbf{X}_k)\Delta V_j\Delta V_k\\ &= \frac{1}{A_i}\sum_{k=1}^{S^-}\sum_{j=1}^{H+}\Big[f_n(\mathbf{u}_j-\mathbf{u}_k,\mathbf{X}_j-\mathbf{X}_k)\frac{\boldsymbol{\eta_n}}{|\boldsymbol{\eta_n}|}\\ &\quad + f_t(\mathbf{u}_j-\mathbf{u}_k,\mathbf{X}_j-\mathbf{X}_k)\frac{\boldsymbol{\eta_t}}{|\boldsymbol{\eta_t}|}\Big]\Delta V_j\Delta V_k \qquad \text{(A.4)}\end{aligned}$$

where i is the index of the particle for which the traction vector is computed, S^- is the total number of collinear particles $\mathbf{X}_k$ determined by the limit of the influence zone of the i-particle in the negative side, and $H+$ is the number of particles in the positive side of the i-particle's horizon. A_i denotes the area corresponding to the i-particle, as Fig. A.39 shows. In this way the tangential component of the traction vector defined above is the shear stress

$$\tau_{n^*v} = \mathbf{t}(\mathbf{X}_i,\mathbf{n}^*)\cdot\mathbf{v} \qquad \text{(A.5)}$$

where **v** denotes the direction orthogonal to that of the outer normal **n***.

References

Bacigalupo, A., Gambarotta, L., 2017. Wave propagation in non-centrosymmetric beam-lattices with lumped masses: discrete and micropolar modeling. Int. J. Solids Struct. 118–119, 128–145.

Ballarini, R., Diana, V., Biolzi, L., Casolo, S., 2018. Bond-based peridynamic modelling of singular and nonsingular crack-tip fields. Meccanica 53 (14), 3495–3515.

Baraldi, D., Bullo, S., Cecchi, A., 2016. Continuous and discrete strategies for the modal analysis of regular masonry. Int. J. Solids Struct. 84, 82–98.

Bobaru, F., 2011. Peridynamics and multiscale modeling. Int. J. Multiscale Comput. Eng. 9 (6), vii–ix.

Bobaru, F., Foster, J., Geubelle, P., Silling, S., 2015. Handbook of Peridynamic Modeling. Advances in Applied Mathematics. CRC Press.

Bobaru, F., Ha, Y., Hu, W., 2012. Damage progression from impact in layered glass modeled with peridynamics. Central Eur. J. Eng. 2 (4), 551–561.

Bolander, J., Saito, S., 1998. Fracture analyses using spring networks with random geometry. Eng. Fract. Mech. 61 (5), 569–591.

Born, M., Huang, K., 1954. Dynamic Theory of Crystal Lattices. Oxford Press.

Brighenti, R., Carpinteri, A., Spagnoli, A., Scorza, D., 2013. Cracking behaviour of fibre-reinforced cementitious composites: a comparison between a continuous and a discrete computational approach. Eng. Fract. Mech. 103, 103–114. Advances in Failure Assessment Using Fracture and Damage Mechanics.

Capecchi, D., Ruta, G., 2015. The Theory of Elasticity in the 19th Century. Springer Verlag.

Capecchi, D., Ruta, G., Trovalusci, P., 2010. From classical to Voigt's molecular models in elasticity. Arch. Hist. Exact. Sci. 64 (5), 525–559.

Casolo, S., 2009. Macroscale modelling of microstructure damage evolution by a rigid body and spring model. J. Mech. Mater. Struct. 4 (3), 551–570.

Casolo, S., Diana, V., 2018. Modelling laminated glass beam failure via stochastic rigid body-spring model and bond-based peridynamics. Eng. Fract. Mech. 190, 331–346.

Cauchy, A., 1828. De la pression ou tension dans un systéme de points materiels. In: Oeuvres Complétes, 3, pp. 253–277.

Cauchy, A., 1850. Mémoire sur les vibrations d'un double système de molécules et de l'éther continu dans un corps cristallisé. In: Oeuvres Complètes, - Tome II, pp. 338–350.

Chang, C., Wang, T., Sluys, L., van Mier, J., 2002. Fracture modeling using a microstructural mechanics approachii. finite element analysis. Eng. Fract. Mech. 69 (17), 1959–1976.

Chen, H., Lin, E., Liu, Y., 2014. A novel volume-compensated particle method for 2d elasticity and plasticity analysis. Int. J. Solids Struct. 51 (9), 1819–1833.

Chen, H., Liu, Y., 2016. A non-local 3d lattice particle framework for elastic solids. Int. J. Solids Struct. 81, 411–420.

Cheng, Z., Zhang, G., Wang, Y., Bobaru, F., 2015. A peridynamic model for dynamic fracture in functionally graded materials. Compos. Struct. 133, 529–546.

Chowdhury, S.R., Rahaman, M.M., Roy, D., Sundaram, N., 2015. A micropolar peridynamic theory in linear elasticity. Int. J. Solids Struct. 59, 171–182.

Cusatis, G., Bažant, Z.P., Cedolin, L., 2003. Confinement-shear lattice model for concrete damage in tension and compression: II. Computation and validation. J. Eng. Mech. 129 (12), 1449–1458.

Cusatis, G., Pelessone, D., Mencarelli, A., 2011. Lattice discrete particle model (ldpm) for failure behavior of concrete. I: Theory. Cem. Concr. Compos. 33 (9), 881–890.

Cusatis, G., Rezakhani, R., Schauffert, E.A., 2017. Discontinuous cell method (DCM) for the simulation of cohesive fracture and fragmentation of continuous media. Eng. Fract. Mech. 170, 1–22.

Dipasquale, D., Sarego, G., Zaccariotto, M., Galvanetto, U., 2016. Dependence of crack paths on the orientation of regular 2d peridynamic grids. Eng. Fract. Mech. 160, 248–263.

Dipasquale, D., Sarego, G., Zaccariotto, M., Galvanetto, U., 2017. A discussion on failure criteria for ordinary state-based peridynamics. Eng. Fract. Mech. 186, 378–398.

Foster, J., Silling, S., Chen, W., 2011. An energy based failure criterion for use with peridynamic states. Int. J. Multiscale Comput. Eng. 9 (6), 675–687.

Foster, J.T., Xu, X., 2018. A generalized, ordinary, finite deformation constitutive correspondence model for peridynamics. Int. J. Solids Struct.

François, M., Chen, L., Coret, M., 2017. Elasticity and symmetry of triangular lattice materials. Int. J. Solids Struct. 129, 18–27.

Gerstle, W., Sau, N., Sakhavand, N., 2009. On peridynamic computational simulation of concrete structures. Int. Concr. Abstr. Portal 265, 245–264.

Gerstle, W., Sau, N., Silling, S., 2007. Peridynamic modeling of concrete structures. Nucl. Eng. Des. 237 (12), 1250–1258.

Griffiths, D.V., Mustoe, G.G.W., 2001. Modelling of elastic continua using a grillage of structural elements based on discrete element concepts. Int. J. Numer. Methods Eng. 50 (7), 1759–1775.

Hassold, G., Srolovitz, D., 1989. Brittle fracture in materials with random defects. Phys. Rev. B 39 (13), 9273–9281.

Hrennikoff, A., 1941. Solution of problems of elasticity by the framework method. ASME J. Appl. Mech. 12, 169–175.

Jagota, A., Scherer, G.W., 1993. Viscosities and sintering rates of a two-dimensional granular composite. J. Am. Ceram. Soc. 76 (12), 3123–3135.

Jiang, C., Zhao, G.F., Khalili, N., 2017. On crack propagation in brittle material using the distinct lattice spring model. Int. J. Solids Struct. 118–119, 41–57.

Kale, S., Ostoja-Starzewski, M., 2015. Handbook of Damage Mechanics: Nano to Macro Scale for Materials and Structures. Springer New York, New York, NY, pp. 203–238. isbn 978-1-4614-5589-9

Karihaloo, B., Shao, P., Xiao, Q., 2003. Lattice modelling of the failure of particle composites. Eng. Fract. Mech. 70 (17), 2385–2406.

Keating, P., 1966. Effect of the invariance requirements on the elastic moduli of a sheet containing circular holes. J. Mech. Phys. Solids 40, 1031–1051.

Le, Q.V., Bobaru, F., 2017. Surface corrections for peridynamic models in elasticity and fracture. Comput. Mech.

Lee, J., Hong, J.W., 2016. Dynamic crack branching and curving in brittle polymers. Int. J. Solids Struct. 100–101, 332–340.

Lehoucq, R., Silling, S., 2008. Force flux and the peridynamic stress tensor. J. Mech. Phys. Solids 56 (4), 1566–1577.

Lilliu, G., van Mier, J., 2003. 3d lattice type fracture model for concrete. Eng. Fract. Mech. 70 (7), 927–941.

Liu, W., Hong, J.W., 2012. Discretized peridynamics for linear elastic solids. Comput. Mech. 50 (5), 579–590.

Luo, J., Ramazani, A., Sundararaghavan, V., 2018. Simulation of micro-scale shear bands using peridynamics with an adaptive dynamic relaxation method. Int. J. Solids Struct. 130–131, 36–48.

Mitchell, J.A, 2011. Nonlocal, Ordinary, state-Based Plasticity Model for Peridynamics, Albuquerque, NM. Sandia Report SAND2011-3166

Madenci, E., Oterkus, E., 2014. Peridynamic Theory and Its Applications. 9781461484653

Madenci, E., Oterkus, S., 2016. Ordinary state-based peridynamics for plastic deformation according to Von Mises yield criteria with isotropic hardening. J. Mech. Phys. Solids 86, 192–219.

Matlab, 2017. Matlab 2017a (Programmimng Language).

Mohammadipour, A., Willam, K., 2017. On the application of a lattice method to configurational and fracture mechanics. Int. J. Solids Struct. 106–107, 152–163.

Monette, L., Anderson, M., 1994. Elastic and fracture properties of the two-dimensional triangular and square lattices. Modell. Simul. Mater. Sci. Eng. 2 (1), 53–66.

Navier, C., 1827. Mmoire sur les lois de l'equilibre et du mouvement des corps solides elastique. Memoires de l'Institut 6, 375–384.

Nikolić, M., Karavelić, E., Ibrahimbegovic, A., Miščević, P., 2017. Lattice element models and their peculiarities. Arch. Comput. Methods Eng.

Ostoja-Starzewski, M., 2002. Lattice models in micromechanics. Appl. Mech. Rev. 55 (1), 35–59.

Pan, Z., Ma, R., Wang, D., Chen, A., 2018. A review of lattice type model in fracture mechanics: theory, applications, and perspectives. Eng. Fract. Mech. 190, 382–409.

Poisson, S., 1813. Remarques sur une quation qui se prsente dans la thorie des attractions des sphroides. Bulletin de la Soci Philomathique de Paris 3, 388–392.

Prakash, N., Seidel, G.D., 2015. A novel two-parameter linear elastic constitutive model for bond based peridynamics. In: 56th AIAA/ASCE/AHS/ASC Structures, Structural Dynamics, and Materials Conference, AIAA SciTech Forum, (AIAA 2015-0461).

Rabczuk, T., Ren, H., 2017. A peridynamics formulation for quasi-static fracture and contact in rock. Eng. Geol. 225, 42–48.

Ren, H., Zhuang, X., Rabczuk, T., 2016. A new peridynamic formulation with shear deformation for elastic solid. J. Micromech. Mole. Phys. 01 (02), 1650009.

Sarego, G., Le, Q., Bobaru, F., Zaccariotto, M., Galvanetto, U., 2016. Linearized state-based peridynamics for 2-d problems. Int. J. Numer. Methods Eng. 108 101174–1197,

Schlangen, E., Garboczi, E., 1996. New method for simulating fracture using an elastically uniform random geometry lattice. Int. J. Eng. Sci. 34 (10), 1131–1144.

Schlangen, E., Garboczi, E., 1997. Fracture simulations of concrete using lattice models: computational aspects. Eng. Fract. Mech. 57 (2), 319–332.

Schlangen, E., van Mier, J., 1992. Simple lattice model for numerical simulation of fracture of concrete materials and structures. Mater. Struct. 25 (9), 534–542.

Silling, S., 2000. Reformulation of elasticity theory for discontinuities and long-range forces. J. Mech. Phys. Solids 48 (1), 175–209.

Silling, S., 2014. Origin and effect of nonlocality in a composite. J. Mech. Mater. Struct. 9 (2), 245–258.

Silling, S., 2017. Stability of peridynamic correspondence material models and their particle discretizations. Comput. Methods Appl. Mech. Eng. 322, 42–57.

Silling, S., Askari, E., 2005. A meshfree method based on the peridynamic model of solid mechanics. Comput. Struct. 83 (17–18), 1526–1535.

Silling, S., Epton, M., Weckner, O., Xu, J., Askari, E., 2007. Peridynamic states and constitutive modeling. J. Elast. 88 (2), 151–184.

Silling, S., Lehoucq, R., 2010. Peridynamic theory of solid mechanics. Adv. Appl. Mech. 44, 73–168.

Stakgold, I., 1950. The Cauchy relations in a molecular theory of elasticity. Q. Appl. Math. 8 (2), 169–186.

Stillinger, F.H., Weber, T.A., 1985. Computer simulation of local order in condensed phases of silicon. Phys. Rev. B 31, 5262–5271.

Sun, S., Sundararaghavan, V., 2014. A peridynamic implementation of crystal plasticity. Int. J. Solids Struct. 51 (19), 3350–3360.

Tancogne-Dejean, T., Mohr, D., 2018. Elastically-isotropic truss lattice materials of reduced plastic anisotropy. Int. J. Solids Struct. 138, 24–39.

Voigt, W., 1887. Theoretische studien ber die elasticittsverhltnisse der krystalle. Abh Ges Wiss Gottingen 34, 3–51.

Wang, Y., Zhou, X., Wang, Y., Shou, Y., 2018. A 3-d conjugated bond-pair-based peridynamic formulation for initiation and propagation of cracks in brittle solids. Int. J. Solids Struct. 134, 89–115.

Warren, T.L., Silling, S.A., Askari, A., Weckner, O., Epton, M.A., Xu, J., 2009. A non-ordinary state-based peridynamic method to model solid material deformation and fracture. Int. J. Solids Struct. 46 (5), 1186–1195.

Weckner, O., Mohamed, N.A.N., 2013. Viscoelastic material models in peridynamics. Appl. Math. Comput. 219 (11), 6039–6043.

Yaghoobi, A., Chorzepa, M., 2017. Fracture analysis of fiber reinforced concrete structures in the micropolar peridynamic analysis framework. Eng. Fract. Mech. 169, 238–250.

Yao, C., Jiang, Q., Shao, J., Zhou, C., 2016. A discrete approach for modeling damage and failure in anisotropic cohesive brittle materials. Eng. Fract. Mech. 155, 102–118.

Zaccariotto, M., Luongo, F., Sarego, G., Galvanetto, U., 2015. Examples of applications of the peridynamic theory to the solution of static equilibrium problems. Aeronaut. J. 119 (1216), 677–700.

Zhang, Z., Chen, Y., 2014. Modeling nonlinear elastic solid with correlated lattice bond cell for dynamic fracture simulation. Comput. Methods Appl. Mech. Eng. 279, 325–347.

Zhao, G.F., Fang, J., Zhao, J., 2011. A 3d distinct lattice spring model for elasticity and dynamic failure. Int. J. Numer. Anal. Methods Geomech. 35 (8), 859–885.

Zhao, S.F., Zhao, G.F., 2012. Implementation of a high order lattice spring model for elasticity. Int. J. Solids Struct. 49 (18), 2568–2581.

Zhu, Q., Ni, T., 2017. Peridynamic formulations enriched with bond rotation effects. Int. J. Eng. Sci. 121, 118–129.